

# UC Santa Barbara

## UC Santa Barbara Electronic Theses and Dissertations

### Title

Variable-temperature kinetic analysis of reaction profiles for the rapid assessment of heterogeneous catalysts

### Permalink

<https://escholarship.org/uc/item/6kn06088>

### Author

Coller, Daniel Hiroshi

### Publication Date

2016

Peer reviewed|Thesis/dissertation

UNIVERSITY OF CALIFORNIA

Santa Barbara

Variable-Temperature Kinetic Analysis of Reaction Profiles for the Rapid Assessment of  
Heterogeneous Catalysts

A dissertation submitted in partial satisfaction of the  
requirements for the degree Doctor of Philosophy  
in Chemical Engineering

by

Daniel Hiroshi Coller

Committee in charge:

Professor Susannah L. Scott, Chair

Professor Michael Gordon

Professor Baron Peters

Professor Ram Seshadri

June 2016

The dissertation of Daniel Hiroshi Coller is approved.

---

Professor Michael Gordon

---

Professor Baron Peters

---

Professor Ram Seshadri

---

Professor Susannah L. Scott, Committee Chair

June 2016

Variable-Temperature Kinetic Analysis of Reaction Profiles for the Rapid Assessment  
of Heterogeneous Catalysts

Copyright © 2016

by

Daniel Hiroshi Coller

## ACKNOWLEDGEMENTS

I would like to thank my advisor, Professor Susannah Scott, for her guidance, support, and the opportunities provided to our research group. This work and my growth as a scientist would not be possible without my advisor. I am grateful to my dissertation committee, Professors Gordon, Peters and Seshadri, for offering their guidance. I would like to thank the PIRE-ECCI program and Professor Jin-Ping Zhang and his research group at SINANO for their hospitality. Additionally, thank you to Air Products for their support, specifically Dr. Rivillon, Mr. Fowler, and Dr. Li for their mentorship and hospitality. All of these exceptional scientists have inspired me; I am forever grateful.

Of course, none of this would have been possible without the love and support I received from my friends and family. First and foremost, my fiancé Jennifer, this journey would not have been possible without your love and support. You are the love of my life, and I cannot wait to start a life with you. Mom, Dad, Bryan, thank you for always being there. To all my friends old and new, I would not have been able to persevere without you.

Thank you to all the Scott group members, particularly Dr. Gallo, Dr. Crisci, Dr. Davis, Dr. Hwang, and Zachary Jones. The spectroscopy in Chapter 4 is a result of the hard work by Zachary Jones and Dr. Davis. I would also like to acknowledge the scientists at CNSI, MRL and SSRL.

This work was supported financially by the US Department of Energy, Office of Science, Division of Basic Energy Sciences, under the Catalysis Science Initiative (DE-FG-02-03ER15467). D. H. C. thanks the PIRE-ECCI program (NSF OISE-0968399) and Air Products for fellowship support. We are grateful to Dr. Ryan Davis and Dr. Ta Na for the catalyst synthesis and characterization.

## VITA OF DANIEL HIROSHI COLLER

June 2016

### EDUCATION

Doctor of Philosophy in Chemical Engineering, University of California, Santa Barbara, June 2016 (expected)

Bachelor of Science in Chemical Engineering, University of California, Irvine, June 2010 (magna cum laude)

### PROFESSIONAL EMPLOYMENT

PhD Intern, Air Products and Chemicals (2014)

Teaching Assistant (2011 – 2013)

### PUBLICATIONS

Coller, D. H., Vicente, B. C., Scott, S. L. “Rapid Extraction of Quantitative Kinetic Information from Variable-Temperature Reaction Profiles”, *Chem. Eng. J.* Just Accepted (2016) DOI: 10.1016/j.cej.2016.05.136

Rosso, D., Jiang, L., Pitt, P., Hocking, C. S., Stenstrom, M. K., Murthy, S., Hayden, D., Zhong, J., Coller, D. H., Kim, A. Y., Xu, H. “Methodology for In Situ Column Testing to Improve Accuracy during Design and Specification of Aeration Systems”, *J. Environ. Eng.* (2013) 139, 530 – 537

### PRESENTATIONS

D. Coller, S. Scott. Oral delivered at AIChE Annual Meeting, Atlanta, GA, 2014.

D. Coller, S. Scott. Oral delivered at Clorox-Amgen Graduate Student Symposium, Santa Barbara, CA, 2014.

D. Coller, S. Scott. Poster presented at 23<sup>rd</sup> NACS meeting, Louisville, KY, 2013.

D. Coller, S. Scott. Poster presented at Clorox-Amgen Graduate Student Symposium, Santa Barbara, CA, 2013.

D. Coller, S. Scott. Oral delivered at NSF PIRE-ECCI Annual Meeting, Suzhou, China, 2012.

### FIELDS OF STUDY

Professor Scott: heterogeneous catalysis, kinetics, reactor design

### AWARDS

Air Products and Chemicals Fellow (2014)

Kokes Award for the North American Catalysis Society Meeting (2013)

NSF PIRE-ECCI Fellow (2012)

## ABSTRACT

### Variable-Temperature Kinetic Analysis of Reaction Profiles for the Rapid Assessment of Heterogeneous Catalysts

by

Daniel Hiroshi Collier

Variable-temperature reaction profiles, measured in a packed bed reactor (PBR) with a constant temperature heating rate, show the conversion vs. the reactor temperature. Reaction profiles that are kinetically-limited can be simulated using just three equations: a power rate law, Arrhenius equation, and the PBR design equation. Numerical solutions are derived for transport-limited reaction profiles with the inclusion of the internal effectiveness factor and the rate of external mass transport. Simulations demonstrated that the position and shape of a reaction profile is unique for each rate law and set of kinetic parameters.

Analysis of experimental variable-temperature reaction profiles is demonstrated for a typical supported catalyst, 2 wt% Pd/Al<sub>2</sub>O<sub>3</sub>, for the oxidation of H<sub>2</sub>, C<sub>3</sub>H<sub>8</sub>, and CO by oxygen. These reactions were shown to be kinetically-limited and free from gradients in temperature and pressure. Quantitative information about the rate law and reaction constant were reliably extracted by curve-fitting as few as two adjustable parameters to reaction profiles. The reaction orders and observed activation energy were rapidly extracted from a single reaction profile recorded in less than an hour (with

appropriate data truncation, when necessary), and they are at least as accurate as the same parameters obtained from much more time-intensive conventional kinetic analysis. More precise curve-fitting parameters can be obtained by global curve-fitting of a series of reaction profiles recorded with different volumetric flow rates.

*In situ* x-ray absorption spectroscopy (XAS) and *operando* infrared (IR) spectroscopy coupled with variable-temperature kinetic analysis was used to probe the active phase of the catalyst during CO oxidation. Quantitative analysis of reaction profiles predicted that the active phase was Pd(0), which was confirmed by XAS and IR. Sudden deviation from ideal kinetic behavior is observed for CO oxidation catalyzed by either Pd or Pt nanoparticles on alumina. The abrupt increase in activity results from changes in the surface chemistry when CO no longer poisons the surface. IR spectroscopy for the Pd catalyst during CO oxidation captured the transient phase of the catalyst in which metallic interactions are substantially reduced. For CO oxidation catalyzed by Pt, the abrupt increases occur more readily for catalysts that are susceptible to internal and/or external mass transport limitations.



<b>TABLE OF CONTENTS</b>	<b>Page</b>
Chapter 1: Introduction.....	1
1.1. Background.....	1
1.2. Reaction mechanisms and rate laws .....	1
1.3. Conventional linear, differential kinetic analysis .....	3
1.3.1. Arrhenius plots.....	3
1.3.2. Rate law analysis .....	4
1.4. Precedents and challenges in transient temperature kinetic analysis.....	5
1.5. Objectives .....	8
References.....	10
Chapter 2: Derivation of Analytical and Numerical Solutions for Variable-Temperature Reaction Profiles and their Usage for Modeling Reaction Profiles .....	13
2.1. Introduction.....	13
2.2. Derivation of analytical kinetic expressions .....	17
2.2.1. Rate laws with a single concentration dependence.....	19
2.2.2. Rate laws with two concentration dependencies .....	21
2.3. Modeling of reaction profiles .....	23
2.3.1. Analytical approximations compared to numerical solutions .....	23
2.3.2. Effects of inlet concentration on reaction profiles.....	24
2.3.3. Effects of reaction order, residence time, and Arrhenius parameters on reaction profiles .....	28
2.4. Conclusions.....	33
References.....	34
Chapter 3: Rapid Extraction of Information from Kinetically-Limited Experimental Reaction Profiles.....	36
3.1. Experimental Methods.....	36
3.1.1. Materials .....	36
3.1.2. Catalytic reaction conditions .....	36
3.1.3. Recording reaction profiles.....	37
3.1.4. Minimization of non-kinetic effects .....	39
3.1.5. Curve-fitting reaction profiles .....	41
3.1.6. Conventional kinetic analysis .....	43
3.2. Linear analysis of differential kinetic data .....	43
3.3. Extracting kinetic parameters from variable-temperature reaction profiles ...	46
3.3.1. Curve-fitting of individual reaction profiles for H <sub>2</sub> oxidation.....	46
3.3.2. Curve-fitting of individual reaction profiles for propane oxidation .....	48
3.3.3. Curve-fitting of individual reaction profiles for CO oxidation .....	50
3.4. Global curve-fitting of variable-temperature reaction profiles.....	52
3.4.1. Simultaneous analysis of H <sub>2</sub> oxidation profiles.....	52
3.4.2. Simultaneous analysis of propane oxidation profiles .....	54
3.4.3. Simultaneous analysis of CO oxidation profiles .....	56
3.5. Discussion.....	57
3.5.1. Qualitative rate law information encoded in reaction profiles .....	57
3.5.2. Quantitative kinetic parameters from individual reaction profiles .....	58
3.5.3. Conversion-dependent changes in kinetic parameters.....	59

3.5.4. Global analysis of multiple variable-temperature reaction profiles .....	60
3.6. Conclusions.....	61
Appendix 3.....	62
References.....	92
Chapter 4: Coupled Variable-Temperature Kinetic Analysis and <i>Operando</i> Spectroscopy Investigation of CO Oxidation Catalyzed by Pd/Al <sub>2</sub> O <sub>3</sub> .....	94
4.1. Introduction.....	94
4.1.1. Light-off for CO oxidation catalyzed by Pd .....	94
4.1.2. Variable-temperature analysis of reaction profiles .....	95
4.1.3. Objectives .....	96
4.2. Experimental methods .....	96
4.2.1. Materials .....	96
4.2.2. Reactivity studies .....	97
4.2.3. <i>Operando</i> IR spectroscopy .....	98
4.2.4. <i>In situ</i> XAS .....	98
4.3. Results.....	99
4.3.1. Variable-temperature kinetic analysis .....	99
4.3.2. <i>Operando</i> IR .....	103
4.3.3. <i>In situ</i> XAS .....	108
4.4. Conclusions.....	111
Chapter 4 Acknowledgments.....	113
Appendix 4.....	114
References.....	116
Chapter 5: Analysis of Variable-Temperature Reaction Profiles Impacted by Mass Transport Limitations .....	118
5.1. Introduction.....	118
5.1.1. Background.....	118
5.1.2. Kinetically-limited variable-temperature reaction profiles .....	119
5.1.3. Mass Transport Effects on Variable-temperature Reaction Profiles ...	121
5.1.4. CO oxidation light-off catalyzed by Pt.....	122
5.1.5. Objectives .....	123
5.2 Experimental Methods.....	124
5.2.1. Materials .....	124
5.2.2. Experimental Methods.....	124
5.2.3. Simulation of Variable-Temperature Reaction Profiles .....	125
5.3. Results.....	126
5.3.1. Analytical description for the impact of mass transport on variable- temperature reaction profiles .....	126
5.3.2. Numerical analysis.....	127
5.3.3. Effect of external mass transport limitations on a simulated first-order reaction .....	128
5.3.4. Effect of internal mass transport limitations on first-order rate laws ..	131
5.3.5. Simulated reaction profiles for CO oxidation under the influence of mass transport .....	133
5.3.6. Influence of flow rate and inlet concentration on experimental reaction profiles .....	137

5.3.7. Influence of particle size on experimental reaction profiles.....	142
5.3.8. Curve-fitting experimental profiles .....	147
5.4. Conclusion .....	151
Appendix 5.....	152
References.....	161
Chapter 6: Conclusions and Future Direction .....	164
6.1. Conclusions.....	164
6.2. Future directions .....	166

LIST OF FIGURES	Page
Fig. 2.1. Comparison of analytical and numerical solutions. ....	22
Fig. 2.2. Effect of inlet concentration on profile position. ....	25
Fig. 2.3. Effect of excess reactant concentration. ....	27
Fig. 2.4. Comparison of shape and position for unimolecular rate laws. ....	28
Fig. 2.5. Effect of $\tau$ , $A$ , and $E_a$ on reaction profiles. ....	30
Fig. 2.6. Comparison of bimolecular and unimolecular rate laws. ....	32
Fig. 3.1. Reactor schematic. ....	38
Fig. 3.2. Individual curve-fits for $H_2$ oxidation. ....	46
Fig. 3.3. Individual curve-fits for $C_3H_8$ oxidation. ....	49
Fig. 3.4. Individual curve-fits for CO oxidation. ....	51
Fig. 3.5. Global curve-fits for $H_2$ oxidation profiles. ....	53
Fig. 3.6. Global curve-fit for $C_3H_8$ oxidation profiles. ....	55
Fig. 3.7. Global curve-fits for CO-equimolar oxidation profiles. ....	56
Fig. 4.1. Stoichiometric CO oxidation catalyzed by Pd/ $Al_2O_3$ . ....	100
Fig. 4.2. Light-off and extinction observed for CO oxidation catalyzed Pd/ $Al_2O_3$ . ....	102
Fig. 4.3. CO conversion determined from <i>operando</i> IR spectroscopy. ....	104
Fig. 4.4. <i>Operando</i> IR during light-off and extinction for CO oxidation catalyzed by Pd/ $Al_2O_3$ . ....	106
Fig. 4.5. Deconvoluted IR spectra in the region of CO adsorption. ....	107
Fig. 4.6. <i>In situ</i> Pd K-edge XANES for CO oxidation catalyzed by Pd/ $Al_2O_3$ . ....	109
Fig. 4.7. $k^2$ -weighted Fourier-transformed <i>in situ</i> XAS. ....	110
Fig. 5.1. Simulated reaction profiles for a first-order rate law in an isothermal packed-bed reactor, influenced by external mass transport. ....	130
Fig. 5.2. Simulated reaction profiles for first-order rate laws under the influence of internal and/or external mass transport limitations. ....	132
Fig. 5.3. Simulated profiles for CO oxidation catalyzed by Pt/ $Al_2O_3$ , showing the effects of internal and external mass transport limitations. ....	134
Fig. 5.4. Simulated reaction profiles for CO oxidation catalyzed by Pt/ $Al_2O_3$ for 3 volumetric flow rates. ....	136
Fig. 5.5. Effect of inlet $O_2$ concentration and flow rate on light-off profiles for CO oxidation catalyzed by Pt/ $Al_2O_3$ (20-40 mesh particle size). ....	139
Fig. 5.6. Effect of residence time on light-off profiles for CO oxidation. ....	140
Fig. 5.7. Effect of particle size on the light-off profile for CO oxidation ( $\Theta_{O_2} = 100$ , $v_0 = 50 \text{ mL min}^{-1}$ ) catalyzed by Pt/ $Al_2O_3$ . ....	143
Fig. 5.8. Particle size effect on light-off profiles for CO oxidation catalyzed by Pt/ $Al_2O_3$ . ....	144
Fig. 5.9. Individual curve-fit of Eq. 5.5 to a single reaction profile for CO oxidation catalyzed by Pt/ $Al_2O_3$ . ....	148
Fig. 5.10. Representative Arrhenius plots for CO oxidation catalyzed by Pt/ $Al_2O_3$ . ....	150

<b>List of Tables</b>	<b>Page</b>
<b>Table 2.1.</b> Variable-temperature reaction profile equations for kinetically-limited reactions with unimolecular rate laws .....	20
<b>Table 2.2.</b> Variable-temperature reaction profile equations for kinetically-limited reactions with bimolecular rate laws .....	22
<b>Table 3.1.</b> Comparison of apparent Arrhenius parameters extracted by linearization of data from differential, steady-state experiments with those obtained by non-linear curve-fitting of integral, variable-temperature reaction profiles .....	45
<b>Table 3.2.</b> Apparent Arrhenius parameters and reaction orders extracted from global curve-fits <sup>a</sup> of Eq. 7 to reaction profiles.....	53
<b>Table 5.1.</b> Relationship between light-off temperature and conversion for CO oxidation catalyzed by Pt/Al <sub>2</sub> O <sub>3</sub> <sup>a</sup> .....	138
<b>Table 5.2.</b> Maximum observed conversion in CO oxidation catalyzed by Pt/Al <sub>2</sub> O <sub>3</sub> <sup>a</sup> .....	141
<b>Table 5.3.</b> Activation parameters for CO oxidation <sup>1</sup> over Pt/Al <sub>2</sub> O <sub>3</sub> .....	148

# **Chapter 1: Introduction**

## **1.1. Background**

Reaction kinetics and mechanisms are essential for the prediction of catalytic behavior and the design of new catalytic materials and reactor configurations. Analytical kinetic expressions can be used to extract kinetic information from experimental data and to predict activity through simulations [1, 2]. Kinetic expressions reduce the need for expensive and time-intensive experiments at the lab and pilot scale. It is advantageous to work with expressions that capture the critical parameters of the reaction and require the fewest number of kinetic parameters, thus reducing the mathematical complexity and number of experiments required for parameter estimation. For example, the relatively simple empirical expressions developed by Voltz et. al [3] in 1973 are still used in the automobile exhaust industry to predict catalytic activity during three-way catalysis. Conventional experimental techniques for kinetic analysis developed decades ago remain the standard for kinetic analysis today [4, 5], despite advances in analytical, theoretical, and computational methods. Although new techniques (with several advantages and disadvantages relative to conventional analysis) have been continually developed and employed recently (see section 1.4), none have achieved widespread use or acceptance.

## **1.2. Reaction mechanisms and rate laws**

Descriptions of gas and liquid phase reactions require knowledge of all the reactant and product interactions with the catalyst surface and adsorbed species on the solid catalyst

[1]. Reactants diffuse to the external surface of the catalyst, diffuse into pores, adsorb on to active sites and react. Products desorb from active sites, and finally diffuse away from the catalyst. Often the diffusion processes are fast relative to the rates of adsorption/desorption and reaction, therefore the reaction is considered reaction- or kinetically-limited. The reaction mechanism refers to the sequence of chemical steps independent of the diffusion steps. Each step is called an elementary reaction, such as the adsorption of a species on to a surface or the dissociation of a reactant on the surface. The reaction mechanism is simplified using methods such as the pseudo-stead- state approximation, most abundant reaction intermediate, and determination of the rate-limiting step, to write an expression for a rate law that encompasses all important kinetic parameters that are necessary to capture the kinetics of the reaction. The Langmuir-Hinshelwood mechanism is often used to explain the surface reaction between two adsorbed reactants [1, 2, 6]. For a reaction between species **a** and **b** in which the rate-limiting step is the surface reaction, and both reactants adsorb molecularly, the rate law for species **a** can be written in terms of the rate of reaction ( $-r_a$ ), the reaction rate constant ( $k$ ), equilibrium adsorption coefficient for each reactant ( $K_i$ ), and the gas phase concentrations for each reactant ( $C_i$ ), Eq. 1.1.

$$-r_a = k \frac{K_a K_b C_a C_b}{(1 + K_a C_a + K_b C_b)^2} \quad (1.1)$$

The full Langmuir-Hinshelwood mechanism (and others) can be simplified to a power rate law under most reaction conditions because certain kinetic parameters may be much larger than others which simplifies the expression. For example, if **a** adsorbs irreversibly and **b** adsorbs weakly, under high concentrations the denominator of Eq. 1.1

simplifies to  $(K_a C_a)^2$ , resulting in a power rate law of  $-r_a = k K_b C_b / (K_a C_a)$ . The power rate law has the advantage of simplifying the mathematics and reducing the number of physical parameters that must be estimated. An arbitrary rate law is expressed in Eq. 1.2, where the concentration of two species **a** and **b** are raised to the powers  $n$  and  $m$ , which are called reaction orders.

$$-r_a = k [C_a]^n [C_b]^m \quad (1.2)$$

There also exist cases in which empirical power rate laws adequately account for the reaction kinetics. Therefore the power rate law is often curve-fitted to experimental kinetic data and used to simulate theoretical data [6].

### 1.3. Conventional linear, differential kinetic analysis

#### 1.3.1. Arrhenius plots

Kinetic parameters such as the energy of activation,  $E_a$ , and the pre-exponential factor,  $A$ , are typically obtained from experimental data using the Arrhenius relationship, Eq. 1.3.

$$k = A \exp \left[ -\frac{E_a}{RT} \right] \quad (1.3)$$

Generally, the rate of reaction or rate constant is determined from several different isothermal experiments. The activation energy is extracted from the slope of a plot of  $\ln(k)$



or  $\ln(-r_a)$  vs. inverse-temperature ( $T^{-1}$ ) [7, 8]. The rate may be substituted by either the turnover frequency (TOF) or the conversion ( $X$ ). While this method is known and widely accepted, the accuracy of the extracted activation parameters can be poor (and often unacknowledged to be so); many independent experiments are needed to obtain reliable values. Reported values for  $E_a$  generally have errors of at least 4-8 kJ mol<sup>-1</sup> [8]. The pre-exponential factor may only be retrieved from the y-intercept of a plot of  $\ln(k)$  vs.  $T^{-1}$ . It cannot be extracted from any other conventional analysis because these methods assume there are no gradients in conversion between isothermal experiments. Furthermore, only a small range of temperatures is studied to minimize the change in conversion between experiments, meaning that the majority of the reaction conditions are not considered. While the use of  $k$  is the most precise, it is more common to see Arrhenius plots of  $-r_a$ , TOF, or  $X$ . The linearization of data has persisted despite advances in computers and the myriad of benefits associated with non-linear fitting. When linearization of these parameters is used, it is critical that only differential conditions are explored experimentally [7, 8]. Differential kinetics require that the conversion is minimal such that gradients in temperature and concentration are minimized. Often this translates to a maximum conversion of  $X < 0.1$ , although studies may go as high as  $X < 0.2$ .

### **1.3.2. Rate law analysis**

Conventional determination of reaction orders, assuming a reaction mechanism can be simplified into a power rate law, follows a similar procedure to analysis of the activation energy. Each reaction order requires an independent set of experiments in addition to the set of experiments required to determine the Arrhenius parameters. One reactant is held in excess such that its concentration can be considered constant for all measurements. The rate

of reaction is measured for a series of isothermal measurements (such that the conversion is always differential) where each data point corresponds to a different concentration of the limiting reactant ( $C_a$ ). Linear regression of a plot of  $\ln(-r_a)$  vs.  $\ln(C_a)$  yields the reaction order with respect to the limiting reactant [4, 5]. In order to extract the next reaction order, the concentrations must be reversed such that what was the limiting reactant is now the excess reactant and vice versa.

#### **1.4. Precedents and challenges in transient temperature kinetic analysis**

Rate data collected under transient temperature conditions has long been used to extract quantitative kinetic information in materials science and engineering other than heterogeneous catalysis. In thermal analysis, it is used to determine activation parameters for solid-state phase transitions and decomposition reactions [9, 10]. For example, thermogravimetric analysis (TGA) records decreases in mass that reflect the progress of solid-state reactions [11, 12]. Temperature-programmed desorption (TPD) reveals information about adsorbates [13] (although kinetic parameters can be complicated by readsorption, especially in the case of porous materials [14]). Transient temperature kinetics has been used to accelerate pharmacological screening of drug candidates for their thermal, hydrolytic and oxidative stability [15].

Variable temperature kinetics (VTK) have been used to obtain kinetic information about liquid-phase organic reactions, including base-catalyzed hydrolyses [16-18] and esterifications [19]. Inorganic reactions studied using VTK methods include isomerizations [20, 21] and oxidative additions [22], as well as ligand substitution reactions of metal complexes [23]. In some of these liquid phase batch studies, similar accuracy for kinetic

parameters and model discrimination was reported for both traditional differential and transient temperature methods, although the latter gave results several orders of magnitude faster (since far fewer experiments were required). In other studies, analysis of transient temperature experiments was found to be both faster *and* more accurate, principally because statistical errors decrease when vastly more kinetic data is collected.

Interpreting VTK for gas phase reactions in a non-stirred flow reactor is more challenging, because the kinetics are often more strongly convoluted with non-kinetic effects. Gradients in temperature, pressure and concentration may exist inside the reactor, and inside individual catalyst particles. Feed gases may bypass solid catalyst particles in a packed bed. Nevertheless, there have been attempts to extract kinetic information from data recorded in flow reactors where the temperature is ramped, particularly in catalytic converter studies, where accurate and predictive models are required for vehicle-specific decisions about catalyst configurations. For this application, the low temperature (cold-start) performance is important, and quantitative predictions of engine emissions at conversions that are much higher than differential are required. Large transients in temperature, gas composition, and flow rate are typical of real operating conditions.

One approach is to simulate the behavior in a near-adiabatic catalyst monolith or packed-bed reactor involves using the mass and energy balances for the gas and solid phases simultaneously in a 1D plug-flow model. The equations are solved sequentially until convergence using manually adjusted parameters, or residual minimization methods. Another approach is to simulate reaction profiles using kinetic parameters measured for individual reaction steps by conventional methods. Reactions studied using both methods vary from simple CO oxidation [24-28] to CO oxidation in the presence of H<sub>2</sub> [29, 30], the

CO-NO reaction [24, 26], hydrocarbon combustion [24, 26, 31], and methanol steam reforming [31, 32]. In general, only approximate agreement is observed between the experimental and simulated profiles, both for global models (based on power rate laws), and for microkinetic models. The latter generally have large numbers of adjustable parameters, and even fixing some of them based on prior knowledge yields optimized parameter sets that are not unique.

When the temperature ramp rate is slow relative to the reactor residence time, and the heat of reaction is removed efficiently by dilution of the feed gas with an inert, the catalyst bed can be close to isothermal during the measurement time. The better heat and mass transfer characteristics of the PBR relative to monoliths result in activity profiles that are more representative of intrinsic kinetics. In one such study, the shape of the reaction profile was used to discriminate between positive and negative reaction orders with respect to the limiting reagent, and to identify the transition from kinetically-limited to mass transfer-limited conditions, using the relation between conversion and reactor temperature [33]. However, while agreement between the curve-fits and experimental data for CO oxidation and methane combustion is quite good [33, 34], the resulting kinetic parameters were not deemed unreliable.

A method of temperature scanning in a plug-flow reactor (TS-PFR) was developed to increase the rate of data acquisition by making simultaneous measurements of space-time, reactor exit temperature, and outlet concentrations [35]. Numerical differentiation of the smoothed conversion data with respect to the space-time gives the reaction rate as a function of temperature. However, the fits are difficult to assess visually; instead, models are compared via the magnitudes of the sums of squared errors. For example, CO oxidation over

Pt/ $\gamma$ -Al<sub>2</sub>O<sub>3</sub> was examined with a view to determine the reaction order with respect to O<sub>2</sub> using Langmuir-Hinshelwood models with eight adjustable parameters. Global analysis for several feed rates was conducted using more than 10 000 data points. Results analyzed over the full range of conversion gave a smaller uncertainty for a dissociative adsorption model (i.e., half-order in O<sub>2</sub>), compared to a molecular adsorption model (i.e., first-order in O<sub>2</sub>), although some parameters were highly correlated and not unique [36]. Similarly, temperature scanning steam reforming of methanol over a Cu/ZnO/Al<sub>2</sub>O<sub>3</sub> catalyst was analyzed with a 20-parameter Langmuir-Hinshelwood model, for which 7 parameters were fixed at known values [37]. Modest agreement with the literature for the remaining adsorption and activation enthalpies and entropies suggests that this method, too, is not highly quantitative.

## 1.5. Objectives

We aim to develop a method that allows for the rapid extraction of kinetic parameters from variable-temperature reaction profiles ( $T,X$ ) data. The method is intended to be general and easily accessible with the added value of decreasing uncertainty in parameter estimation, acquisition time, and data analysis time. Furthermore, the method will provide important qualitative information not attainable from conventional techniques, and it will not rely on extensive prior kinetic studies. Variable-temperature kinetic analysis of reaction profiles is meant to aid researchers in studying and predicting catalytic activity. The rapid nature of the method is amenable to current high-throughput techniques in catalyst design, and addresses the need for rapid catalyst assessment.

Chapter 2 will develop the analytical expressions necessary for simulating kinetically-limited reaction profiles and curve-fitting experimental data. The expressions will be used to demonstrate how the features of reaction profiles are affected by kinetic and reactor parameters for kinetically-limited reactions, and what this means for researchers.

In Chapter 3, the expressions will be used to rapidly extract kinetic information from three general reactions with importance to automobile exhaust catalysis. Two different methods of curve-fitting are explored; curve-fitting individual profiles, and simultaneous fitting of a series of profiles recorded under different conditions.

In Chapter 4, the kinetics and light-off for CO oxidation catalyzed by PdO/Al<sub>2</sub>O<sub>3</sub> will be investigated. *Operando* and *in situ* infrared spectroscopy and X-ray absorption spectroscopy of PdO/Al<sub>2</sub>O<sub>3</sub> will be combined with variable-temperature reaction profile analysis to understand the chemical state of the catalyst during light-off.

The influence of mass transport during catalysis will be explored in Chapter 5. Expressions for mass transport-limited reaction profiles will be developed and simulated. Experimental profiles for CO oxidation catalyzed by Pt/Al<sub>2</sub>O<sub>3</sub> are investigated for the effects of diffusion on light-off.

Final conclusions and future outlook for variable-temperature reaction profile analysis is discussed in Chapter 6.

## References

- [1] O.A. Hougen, K.M. Watson, Solid catalysts and reaction rates, *Ind. Eng. Chem.* 35 (1943) 529-541.
- [2] K.H. Yang, O.A. Hougen, Determination of mechanism of catalyzed gaseous reactions, *Chem. Eng. Prog.* 46 (1950) 146-157.
- [3] S.E. Voltz, C.R. Morgan, Liederma.D, S.M. Jacob, Kinetic study of carbon-monoxide and propylene oxidation on platinum catalysts, *Ind. Eng. Chem. Prod. Res. Dev.* 12 (1973) 294-301.
- [4] H.S. Fogler, *Elements of chemical reaction engineering*, 4th ed., Prentice Hall PTR, Upper Saddle River, NJ, 2006.
- [5] G.B. Marin, G.S. Yablonsky, *Kinetics of chemical reactions : decoding complexity*, Wiley-VCH Verlag, Weinheim, Germany, 2011.
- [6] S. Weller, Analysis of kinetic data for heterogeneous reactions, *AIChE J.* 2 (1956) 59-62.
- [7] J. Bagg, Apparent activation energies on catalysts with heterogeneous surfaces. 1. General derivation, *J. Catal.* 16 (1970) 370-&.
- [8] V.P. Zhdanov, Arrhenius parameters for rate processes on solid surfaces, *Surface Science Reports* 12 (1991) 185-242.
- [9] A.K. Galway, Kinetic background to thermal analysis and calorimetry, in: M.E. Brown (Ed.) *Handbook of Thermal Analysis and Calorimetry*, Elsevier, Amsterdam, 1998, pp. 147-224.
- [10] A. Tiwari, B. Raj, *Reactions and Mechanisms in Thermal Analysis of Advanced Materials*, Wiley, Hoboken, New Jersey, 2015.
- [11] E.S. Freeman, B. Carroll, The application of thermoanalytical techniques to reaction kinetics - the thermogravimetric evaluation of the kinetics of the decomposition of calcium oxalate monohydrate, *J. Phys. Chem.* 62 (1958) 394-397.
- [12] A.W. Coats, J.P. Redfern, Kinetic parameters from thermogravimetric data, *Nature* 201 (1964) 68-69.
- [13] J.B. Miller, H.R. Siddiqui, S.M. Gates, J.N. Russell, J.T. Yates, J.C. Tully, M.J. Cardillo, Extraction of kinetic-parameters in temperature programmed desorption - a comparison of methods, *J. Chem. Phys.* 87 (1987) 6725-6732.
- [14] R.A. Demmin, R.J. Gorte, Design parameters for temperature-programmed desorption from a packed-bed, *J. Catal.* 90 (1984) 32-39.
- [15] G. Alibrandi, Alternative accelerated methods for studying drug stability: variable-parameter kinetics, in: S.C. Gad (Ed.) *Pharmaceutical Manufacturing Handbook: Regulations and Quality*, Wiley, Hoboken, New Jersey, 2008, pp. 701-724.
- [16] S.P. Asprey, B.W. Wojciechowski, N.M. Rice, A. Dorcas, Applications of temperature scanning in kinetic investigations: The hydrolysis of acetic anhydride, *Chem. Eng. Sci.* 51 (1996) 4681-4692.
- [17] L.F. Brown, B.A. Robinson, Using temperature-programmed reaction for kinetics analysis of liquid-phase reactions, *Chem. Eng. Sci.* 41 (1986) 963-970.
- [18] S.A. Birdsell, B.A. Robinson, Kinetics of aryl halide hydrolysis using isothermal and temperature-programmed reaction analyses, *Ind. Eng. Chem. Res.* 28 (1989) 511-518.
- [19] M. Maeder, K.J. Molloy, M.M. Schumacher, Analysis of non-isothermal kinetic measurements, *Anal. Chim. Acta* 337 (1997) 73-81.

- [20] G. Alibrandi, Nonisothermal spectrophotometric kinetics applied to inorganic reactions, *Inorg. Chim. Acta* 221 (1994) 31-34.
- [21] R. Romeo, G. Alibrandi, Structure-reactivity correlations for the dissociative uncatalyzed isomerization of monoalkylbis(phosphine)platinum(II) solvento complexes, *Inorg. Chem.* 36 (1997) 4822-4830.
- [22] F.N. Hosseini, S.M. Nabavizadeh, Application of variable-temperature kinetic experiments to oxidative addition reactions of dimethylplatinum(II) complexes with alkyl halides, *Transit. Met. Chem.* 38 (2013) 699-703.
- [23] S.L. Zhang, T.L. Brown, Application of the non-isothermal approach to the kinetics of organometallic reactions: The substitution of ( $\eta^5$ -pentamethylcyclopentadienyl)dicarbonylrhodium(I), *Inorg. Chim. Acta* 240 (1995) 427-433.
- [24] N. Matthess, D. Schweich, B. Martin, F. Castagna, From light-off curves to kinetic rate expressions for three-way catalysts, *Top. Catal.* 16 (2001) 119-124.
- [25] R.E. Hayes, F.H. Bertrand, C. Audet, S.T. Kolaczowski, Catalytic combustion kinetics: Using a direct search algorithm to evaluate kinetic parameters from light-off curves, *Can. J. Chem. Eng.* 81 (2003) 1192-1199.
- [26] A. Pandya, J. Mmbaga, R.E. Hayes, W. Hauptmann, M. Votsmeier, Global kinetic model and parameter optimization for a diesel oxidation catalyst, *Top. Catal.* 52 (2009) 1929-1933.
- [27] C. Depcik, S. Loya, A. Srinivasan, T. Wentworth, S. Stagg-Williams, Adaptive global carbon monoxide kinetic mechanism over platinum/alumina catalysts, *Catalysts* 3 (2013) 517-542.
- [28] J.E. Etheridge, T.C. Watling, Is reactor light-off data sufficiently discriminating between kinetic parameters to be used for developing kinetic models of automotive exhaust aftertreatment catalysts? The effect of hysteresis induced by strong self inhibition, *Chem. Eng. J.* 264 (2015) 376-388.
- [29] D. Bhatia, M.P. Harold, V. Balakotaiah, Kinetic and bifurcation analysis of the cooxidation of CO and H<sub>2</sub> in catalytic monolith reactors, *Chem. Eng. Sci.* 64 (2009) 1544-1558.
- [30] N. Rankovic, A. Nicolle, D. Berthout, P. Da Costa, Kinetic modeling study of the oxidation of carbon monoxide-hydrogen mixtures over Pt/Al<sub>2</sub>O<sub>3</sub> and Rh/Al<sub>2</sub>O<sub>3</sub> catalysts, *J. Phys. Chem. C* 115 (2011) 20225-20236.
- [31] C. Dubien, D. Schweich, G. Mabilon, B. Martin, M. Prigent, Three-way catalytic converter modelling: fast- and slow-oxidizing hydrocarbons, inhibiting species, and steam-reforming reaction, *Chem. Eng. Sci.* 53 (1998) 471-481.
- [32] S. Sa, J.M. Sousa, A. Mendes, Steam reforming of methanol over a CuO/ZnO/Al<sub>2</sub>O<sub>3</sub> catalyst, part I: Kinetic modelling, *Chem. Eng. Sci.* 66 (2011) 4913-4921.
- [33] F. Duprat, Light-off curve of catalytic reaction and kinetics, *Chem. Eng. Sci.* 57 (2002) 901-911.
- [34] P. Stefanov, S. Todorova, A. Naydenov, B. Tzaneva, H. Kolev, G. Atanasova, D. Stoyanova, Y. Karakirova, K. Aleksieva, On the development of active and stable Pd-Co/gamma-Al<sub>2</sub>O<sub>3</sub> catalyst for complete oxidation of methane, *Chem. Eng. J.* 266 (2015) 329-338.
- [35] B.W. Wojciechowski, N.M. Rice, *Experimental methods in kinetic studies*, Elsevier, Boston, 2003.



- [36] B.W. Wojciechowski, S.P. Asprey, Kinetic studies using temperature-scanning: the oxidation of carbon monoxide, *Appl. Catal. A: Gen.* 190 (2000) 1-24.
- [37] S.P. Asprey, B. W. Wojciechowski, B.A. Peppley, Kinetic studies using temperature-scanning: the steam-reforming of methanol, *Appl. Catal. A: Gen.* 179 (1999) 51-70.

## **Chapter 2: Derivation of Analytical and Numerical Solutions for Variable-Temperature Reaction Profiles and their Usage for Modeling Reaction Profiles**

### **2.1. Introduction**

As high-throughput methods for materials synthesis become more versatile and accessible [1], large numbers of heterogeneous catalysts covering a wide range of composition space can be generated quickly [2-4], creating a need for similarly fast and flexible methods to screen for catalytic activity. Comparing performance in a catalyst array at a common temperature has limited usefulness, because the onset of activity can be very abrupt for surface-mediated reactions. Using the temperature required to achieve 50 % conversion of a limiting reagent,  $T_{50}$ , can also be problematic, because the single-point measurement may be strongly influenced by non-kinetic effects. Even when this is not the case, comparisons are valid only for measurements made under the same conditions (residence time, feed composition, dispersion of the active phase, etc.), and for catalysts that follow the same rate law. A more robust kinetic assessment requires measurement of reaction orders and activation parameters over a range of operating conditions, which is typically slow and labor-intensive even for a single catalyst. Even more time-consuming is the assembly of a microkinetic model, requiring extensive measurements across a wide range of experimental conditions to identify and quantify the rates of all elementary steps. Nevertheless, acquiring as much of this information as possible for a series of heterogeneous catalysts in a variety of reaction atmospheres is ultimately necessary for properly

interpreting reactivity differences, rationalizing the search for and design of new catalysts, benchmarking and optimizing their performance.

Some kinetic descriptors, such as the turnover frequency (TOF), can be obtained relatively quickly [5], although direct comparisons are still difficult, especially when a series of catalysts exhibits widely varying activities. A recent proposal [6] to create a “standard” TOF suffers from the need to make long extrapolations, and TOFs can be mis-used in such comparisons [7]. The empirical Arrhenius parameters  $A$  (or  $k_0$ ) and  $E_a$  are more generally useful. Ideally, they should be obtained from the temperature dependence of a rate constant, which in turn implies knowledge of the rate law.<sup>1</sup> However, even when the form of the rate law is not known,  $E_a$  can be extracted from the temperature dependence of the conversion ( $X$ ) at the outlet of a packed bed reactor (PBR) operated under differential conditions. Obviously, the same information is available from the temperature dependence of the reaction rate ( $-r_a$ ), computed from the product of  $X$  and  $F_{a,0}$  (the molar flow rate of the limiting reactant **a**).

In a conventional kinetic analysis conducted in a packed-bed reactor, the reaction orders assessed in a series of isothermal experiments for which each inlet concentration is varied independently while keeping the conversion very low. The activation parameters are extracted from the response of the outlet conversion to changes in temperature. The need for isothermal and differential conditions to ensure kinetic control of the rate imposes important constraints on kinetic experiments. The measurements themselves at very low conversions are often inherently imprecise. Keeping the temperature range small to maintain such

---

<sup>a</sup> If  $k$  is a rate constant for an elementary step, an Eyring plot ( $[\ln(k/T)]$  vs.  $T^{-1}$ ), is preferred because it gives the physically meaningful activation parameters  $\Delta H^\ddagger$  and  $\Delta S^\ddagger$ . However, most measurements in heterogeneous catalysis generate apparent rate constants that contain multiple unresolved contributions from adsorption/desorption and reaction steps. In such cases, the empirical Arrhenius treatment is usually considered satisfactory.

conversions contributes to a large (and often unacknowledged) uncertainty in the Eyring and/or Arrhenius parameters. Perhaps most significantly, experiments performed at low conversion over a limited temperature range inevitably exclude the majority of reaction conditions, including those which are likely to be most relevant to practical reactor operation.

Even for a single catalyst, a complete kinetic study requires many experiments over an extended period of time, such that maintaining reactor and catalyst stability can be challenging. For catalysts that deactivate rapidly, the need to conduct lengthy isothermal kinetics experiments is particularly problematic. For example, kinetic analysis of a single-site Pd catalyst for CO oxidation was limited to a single data point at each reactor condition, and steady-state operation was never achieved due to rapid catalyst deactivation [8]. Finally, conventional methods of analysis for isothermal kinetic data involve linearization, which alters the weighting of experimental data, and yields parameters susceptible to correlations [9-11]. Consequently, distinguishing between kinetic models can be prone to error, and complex behavior can be masked. While more accurate and discriminating methods using non-linear analysis of variable temperature kinetic data have long been available [12, 13], they have not been widely adopted.

Much of the kinetic information we seek (rate law, activation parameters) is contained in the light-off profile. According to one definition, catalyst “light-off” occurs at the transition between the kinetically-controlled low temperature performance and the diffusion-controlled high temperature performance. However, with appropriate choice of reactor conditions, the entire  $X$ - $T$  plot can be recorded under predominantly kinetically-controlled conditions, and is still commonly called a light-off profile. Here, we will describe

such data that is free of transport influences as a variable temperature reaction profile. These data are rarely exploited for kinetic parameters (other than the activation energy, from the leading edge of the curve) although their analysis could alleviate several of the drawbacks of isothermal kinetic work. These include differences in sample (e.g., catalyst bed) and reactor characteristics across a series of isothermal runs, and variable temperature reactions that take place while the reactor is being heated to each desired temperature, giving the catalyst a complex thermal history. A method for the quantitative analysis of variable temperature reaction profiles could dramatically reduce the amount of time necessary to assess kinetic parameters for large numbers of heterogeneous catalysts, or even for a small number of catalysts under a wide range of reaction conditions. In principle, it would allow several kinetic parameters to be measured in a single experiment, minimizing the use of time and material and providing rapid results based on performance to guide catalyst synthesis. This in turn would allow researchers to allocate more resources to their most promising leads, and to reduce time spent on catalysts with inadequate properties.

Since variable temperature reaction profiles cover a large temperature range, they generate richer kinetic information (thereby increasing the accuracy of derived kinetic parameters), and allow the validity of a proposed rate law to be assessed over a wider range of conversions. This in turn results in a more robust and versatile reaction model which more completely describes the behavior of industrial reactors, which often operate at high conversion and usually possess temperature gradients. As a corollary, abrupt or gradual changes in kinetic behavior (signaled by deviation from the expected shape of the reaction profile, or changes in the curve-fit parameters) can be used to identify precisely the

conditions where the reaction mechanism and/or the nature of the active sites change, or where the onset of mass transfer limitations occurs.

A general method to extract reliable kinetic parameters from integral  $X$ - $T$  data has yet to be reported. In this report, we show that analysis of kinetically-controlled variable temperature reaction profiles can be fast, simple to implement, and easy to assess for agreement between experiment and model. The straightforward analytical method does not depend on the availability of extensive prior kinetic information, and the results are quantitatively comparable to those obtained by conventional kinetic analysis. Since there is no need for long waiting periods associated with conventional data acquisition under isothermal steady-state conditions, experiments can be conducted much faster, and catalyst deactivation is less problematic. The method is applied to the catalytic oxidation of CO, H<sub>2</sub> and propane, all of which are key reactions in vehicle emissions control during catalyst warm-up.

## 2.2. Derivation of analytical kinetic expressions

Reactions that are kinetically-limited, obey Arrhenius behavior, and take place in a reactor that contains minimal temperature gradients and minimal resistance to mass transport can in principle be fully analyzed using only three relations: a rate law, the Arrhenius equation, and a reactor design equation (mass balance). For many reactions a simple power rate law is enough to fully capture the kinetics of the reactions under specific conditions. A power rate law can be written for  $j + 1$  reactants in terms of the conversion  $X$  of the limiting reactant **a** with inlet concentration  $C_{a,0}$  (mol m<sup>-3</sup>), where  $\Theta_i$  is the ratio of inlet concentrations for reactants **i** and **a**, and  $m_i$  and  $n$  are their reaction orders, Eq. 2.1.

$$-r_a = k[C_a]^n \prod_i^j [C_i]^{m_i} = k[C_{a,0}(1 - X)]^n \prod_i^j \left[ C_{a,0} \left( \Theta_i - \frac{b_i}{a} X \right) \right]^{m_i} \quad (2.1)$$

The temperature dependence of the rate constant  $k$  is described by the Arrhenius equation, Eq. 2.2, where  $R$  ( $\text{J mol}^{-1} \text{K}^{-1}$ ) is the ideal gas constant. The apparent activation parameters  $A$  and  $E_a$  contain contributions from adsorption, and are presumed temperature-independent over the range of reaction conditions relevant to the variable temperature experiment ( $0.05 < X < 0.95$ ).

$$k = Ae^{-\frac{E_a}{RT}} \quad (2.2)$$

Finally, the design equation for a packed bed reactor (PBR) expressed in terms of the catalyst mass,  $W_{\text{cat}}$  (g), is shown in Eq. 2.3,  $C_{a,0}$  is the inlet concentration of the limiting reagent;  $v_0$  is the inlet volumetric flow rate of the feed gas;  $\tau$  is analogous to the space-time (residence time) and is equal to  $W_{\text{cat}}/v_0$  ( $\text{g}_{\text{cat}} \text{s m}^{-3}$ );  $a$  and  $b_i$  are the stoichiometric coefficients of the limiting reagent **a** and other species **i**, respectively; and  $\Theta_i$  is the molar ratio of species **i** and **a**. The reaction orders with respect to species **a** and **i** are designated  $n$  and  $m_i$ , respectively.

$$\frac{W_{\text{cat}}}{v_0} = \tau = C_{a,0} \int_0^X \frac{dX}{-r_a} \quad (2.3)$$

Assuming the rate constant depends only on temperature (i.e. not on reactant concentrations), substituting Eqs. 2.1-2.2 into Eq. 2.3 yields a general form of the variable temperature kinetic equation, Eq. 2.4 (written in terms of a bimolecular rate law).

$$\frac{\tau_{\text{ref}}}{c_{a,0,\text{ref}}} A e^{-\frac{E_a}{RT}} = \int_0^X \frac{dX}{\left[ c_{a,0,\text{ref}} \frac{T_{\text{ref}}}{T} (1-X) \right]^n \prod_i \left[ c_{a,0,\text{ref}} \frac{T_{\text{ref}}}{T} \left( \Theta_i - \frac{b_i X}{a} \right) \right]^{m_i}} \quad (2.4)$$

### 2.2.1. Rate laws with a single concentration dependence

In favorable cases, Eq. 2.4 can be integrated and solved directly for the conversion. This is true for cases in which the rate law depends on a single concentration (unimolecular;  $m = 0$ ) with an integer reaction order. Although the reaction itself may require more than one reactant, many reactions such as the oxidation of hydrogen [14, 15] or propane [16, 17] obey a unimolecular rate law. For example inverse-first ( $n = -1$ ), zeroth ( $n = 0$ ), first ( $n = 1$ ), and second-order ( $n = 2$ ) rate laws can be analytically evaluated in Eq. 2.4, resulting in reaction profile equations for  $X$ , Table 2.1. If the reaction order is not known it is possible to leave  $n$  variable, allowing for a solution to a general unimolecular reaction, Eq. 2.12, although  $n \neq 1$  for this expression.



**Table 2.1.** Variable-temperature reaction profile equations for kinetically-limited reactions with unimolecular rate laws

$-r_a =$	$X =$	Eq.
$k C_a^{-1}$	$1 - \sqrt{1 - \frac{2\tau_{\text{ref}}}{C_{a,0,\text{ref}}^2} \frac{T}{T_{\text{ref}}} A e^{-\frac{E_a}{RT}}}$	2.8
$k$	$\frac{\tau_{\text{ref}}}{C_{a,0,\text{ref}}} A e^{-\frac{E_a}{RT}}$	2.9
$k C_a^1$	$1 - \exp\left[-\tau_{\text{ref}} \frac{T_{\text{ref}}}{T} A e^{-\frac{E_a}{RT}}\right]$	2.10
$k C_a^2$	$1 - \frac{1}{1 + C_{a,0,\text{ref}} \tau_{\text{ref}} \left(\frac{T_{\text{ref}}}{T}\right)^2 A e^{-\frac{E_a}{RT}}}$	2.11
$k C_a^{n^*}$	$1 - \left\{1 + (n - 1) \tau_{\text{ref}} C_{a,0,\text{ref}}^{n-1} \left(\frac{T_{\text{ref}}}{T}\right)^n A e^{-\frac{E_a}{RT}}\right\}^{\frac{1}{1-n}}$	2.12

\* general  $n^{\text{th}}$ -order rate law, ( $n \neq 1$ ) for the analytical solution for  $X$

Since the inlet temperature of the PBR changes continuously with time, inlet volumetric flow rate and reactant concentrations are not constant. According to the ideal gas law:  $v_0$  and  $C_{a,0}$  are directly and inversely proportional to  $T$ , respectively, Eq. 2.5 – 2.6. At  $T = T_{\text{ref}}$ ,  $\tau_{\text{ref}} = W_{\text{cat}}/v_{0,\text{ref}}$  ( $\text{g}_{\text{cat}} \text{ s m}^{-3}$ ) and  $C_{a,0,\text{ref}}$  is the reference inlet concentration. Therefore, the residence time varies inversely with the temperature, Eq. 2.7. From Eq. 2.5 – 2.7, the volumetric flow rate, inlet concentration, and residence time is determined at any steady state inlet  $T$  for any reaction profile.

$$v_0 = v_{0,\text{ref}} \frac{T}{T_{\text{ref}}} \quad (2.5)$$

$$C_{\text{CO},0} = C_{\text{CO},0,\text{ref}} \frac{T_{\text{ref}}}{T} = \frac{P_{\text{CO},0}}{RT_{\text{ref}}} \frac{T_{\text{ref}}}{T} \quad (2.6)$$

$$\tau = \frac{W_{\text{cat}}}{v_0} = \frac{W_{\text{cat}}}{v_{0,\text{ref}}} \frac{T_{\text{ref}}}{T} = \tau_{\text{ref}} \frac{T_{\text{ref}}}{T} \quad (2.7)$$

### 2.2.2. Rate laws with two concentration dependencies

Analytical solutions for reaction profile equations can also be derived for power rate laws that make no assumption that  $m = 0$  and have a bimolecular concentration dependence. Eq. 2.4 can be analytically integrated only if the ratio of the inlet concentrations is equal to the ratio of the stoichiometric coefficients for species **b** and **a**, i.e.  $\Theta_{\text{b}} = b/a$ . The result, Eq. 2.13, is listed in Table 2.2, and is only valid for  $(n + m) \neq 1$ . If  $(n + m) = 1$  and  $\Theta_{\text{b}} = b/a$ , then the result is Eq. 2.14, which is identical to the unimolecular case for  $n = 1$ ,  $m = 0$ . Otherwise Eq. 2.14 is similar to Eq. 2.10 except for the introduction of the factor  $\Theta_{\text{b}}^m$  which is present in a product with  $k$ .

For the more general case that  $\Theta_{\text{b}} \neq b/a$ , then Eq. 2.4 cannot be solved using analytical methods. However, approximate analytical solutions (Eq. 2.15-2.16) are obtained when  $(\Theta_{\text{b}} - X b/a) \approx \Theta_{\text{b}}$ . When  $\Theta_{\text{b}} \gg b/a$  (i.e., all other reactants present in large excess over the limiting reactant), the approximation is valid for all values of  $X$ . However, when  $\Theta_{\text{b}} \approx b/a$ , Eq. 2.15 should only be used for low-to-moderate values of  $X$  (see Fig. 2.1). Although  $n$  cannot be exactly 1 in Eq. 2.15, the approximation still works for values close to 1, i.e. 0.99; therefore, the relation can still be used for simulations or curve-fitting experimental reaction profiles. Alternatively, if the reaction order for **a** is known to be precisely 1, then Eq. 2.16 can instead be used. The result is similar to a unimolecular first-order reaction profile equation with contributions from  $m$ .

**Table 2.2.** Variable-temperature reaction profile equations for kinetically-limited reactions with bimolecular rate laws

$-r_a = k C_a^n C_b^m$	$X =$	Eq.
$\Theta_b = b/a$	$1 - \left[ 1 + (n+m-1) \left( \frac{T_{\text{ref}}}{T} \right)^{n+m} \left( \frac{b}{a} \right)^m C_{a,0,\text{ref}}^{n+m-1} \tau_{\text{ref}} A e^{-\frac{E_a}{RT}} \right]^{\frac{1}{1-n-m}}$	2.13
$n+m=1,$ $\Theta_b = b/a$ ; or $n=1, m=0$	$1 - \exp \left[ -\tau_{\text{ref}} \left( \frac{T_{\text{ref}}}{T} \right) \Theta_b^m A e^{-\frac{E_a}{RT}} \right]$	2.14
$\Theta_b \neq b/a$	$1 - \left[ 1 + (n-1) \tau_{\text{ref}} C_{a,0,\text{ref}}^{n+m-1} \left( \frac{T_{\text{ref}}}{T} \right)^{n+m} \Theta_b^m A e^{-\frac{E_a}{RT}} \right]^{\frac{1}{1-n}}$	2.15
$n=1, m \neq 0,$ $\Theta_b \gg b/a$	$1 - \exp \left[ -\tau_{\text{ref}} C_{a,0,\text{ref}}^m \left( \frac{T_{\text{ref}}}{T} \right)^{m+1} \Theta_b^m A e^{-\frac{E_a}{RT}} \right]$	2.16

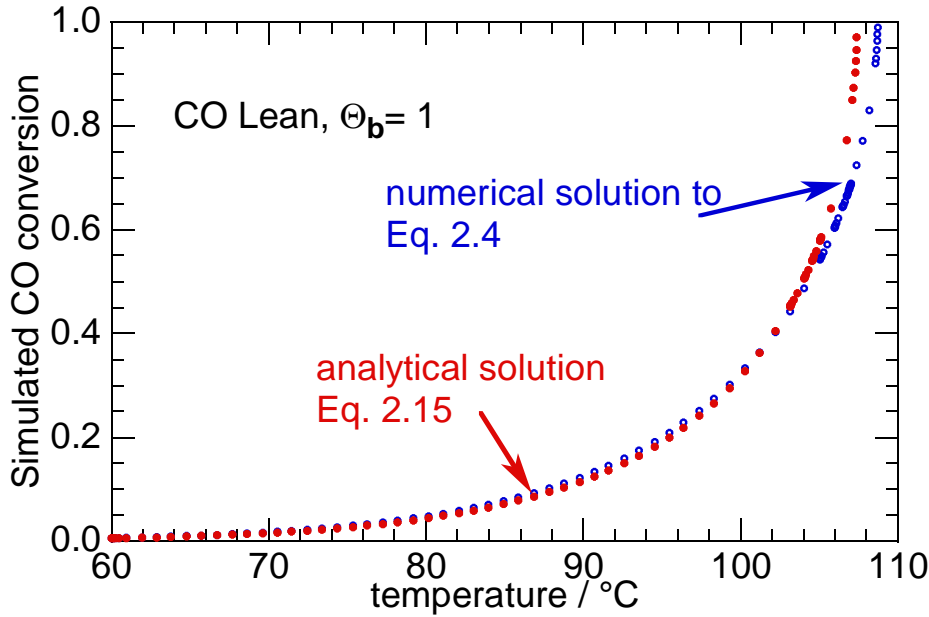


**Fig. 2.1.** Comparison of analytical and numerical solutions.

Comparison of simulated reaction profiles for CO oxidation with equimolar reactants ( $n = 1, m = 1; \Theta_b = 1$ ). The approximate analytical simulation using Eq. 2.15 (filled red circles) uses the approximation  $\Theta_b - X b/a \approx \Theta_b$ . It is nearly superposable on the exact numerical simulation of Eq. 2.4 (open blue circles) up to  $X = 0.6$  (the limit used for curve-fitting). Parameter values:  $C_{0,\text{ref}} = 0.045 \text{ mol m}^{-3}$ ,  $\tau_{\text{ref}} = 1.8 \times 10^4 \text{ g}_{\text{catalyst}} \text{ s m}^{-3}$ ,  $E_a = 100 \text{ kJ mol}^{-1}$ ,  $A = 10^8 \text{ mol g}_{\text{cat}}^{-1} \text{ s}^{-1}$ .

## 2.3. Modeling of reaction profiles

### 2.3.1. Analytical approximations compared to numerical solutions

To validate the assumption that  $(\Theta_b - X b/a) \approx \Theta_b$ , the analytical solution was simulated and compared to the numerical simulation of Eq. 2.4 using the same parameters. Reaction profiles for CO oxidation with a slight excess in O<sub>2</sub> ( $\Theta_b = 1$ ) were simulated using the analytical solution, Eq. 2.15 (for  $\Theta_b \neq b/a = 1/2$ ), and the numerical solution to Eq. 2.4 (Fig. 2.1). The assumption of Eq. 2.15 is most accurate when  $\Theta_b$  is much greater than  $b/a$ , therefore this instance where  $\Theta_b$  is only twice as great as the ratio of the stoichiometric coefficients represents the worst case for the use of Eq. 2.15. The reaction orders were set to  $n = -1$  (CO) and  $m = 1$  (O<sub>2</sub>) [18-20]. The analytical solution deviates from the numerical solution at large conversions ( $X > 0.6$ ) because  $\Theta_b \approx b/a$ . However, the reaction profiles are nearly superposable below this conversion, validating the assumption that  $(\Theta_b - X b/a) \approx \Theta_b$  at low values of  $X$ . Therefore reaction profiles for experiments with a small amount of excess reagents must be truncated in order to use Eq. 2.15-2.16 for curve-fitting. Although cases in which there is an excess greater than a factor of two will require less truncation, and the data sampled will always be much greater than that contained under differential conditions (i.e.  $X < 0.1 - 0.2$ ).

### 2.3.2. Effects of inlet concentration on reaction profiles

Simulations of reaction profiles for a kinetically-controlled reaction with a rate law containing a single concentration term (i.e., variable  $n$ ;  $m = 0$ ) are shown in Fig. 2.2. Four parameters ( $C_{a,0,\text{ref}}$ ,  $\tau_{\text{ref}}$ ,  $A$ , and  $E_a$ ) were varied independently to explore their effects on the shapes and relative positions of the profiles. Information about the rate law is encoded in both the shape of the reaction profile and the concentration dependence of its position along the  $T$ -axis. First-order (and pseudo-first-order) reactions ( $n = 1$ ) give the familiar sigmoidal curve, in which the increase in conversion accelerates with increasing temperature, then decelerates as the concentration of reactant in most of the catalyst bed approaches zero. The position of the reaction profile is independent of inlet concentration (Eq. 2.10). This occurs because the concentration dependence of the rate law is the same as the concentration dependence of the reactor design equation.

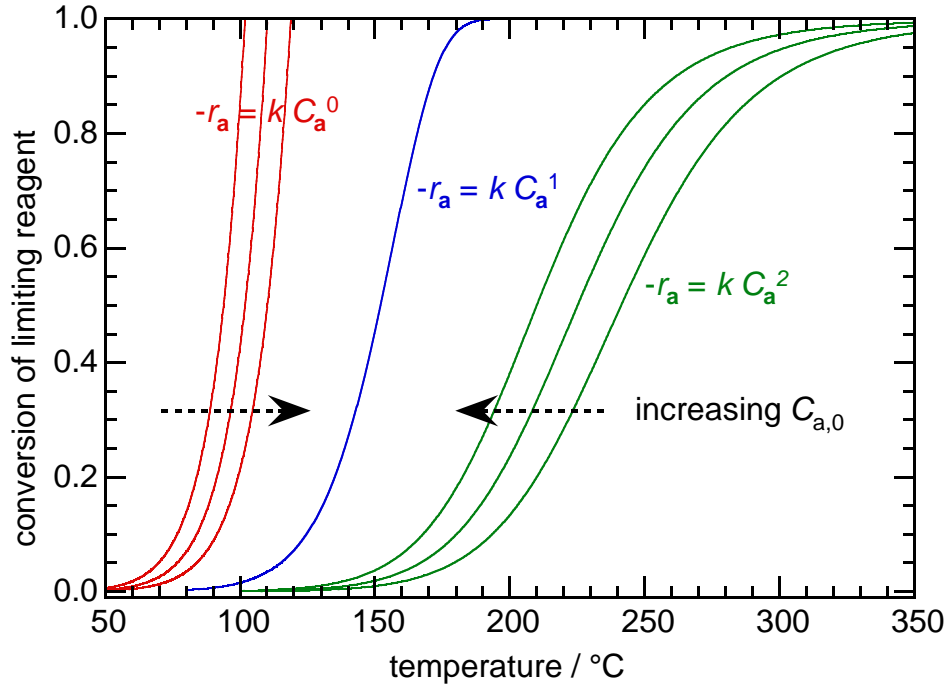


**Fig. 2.2.** Effect of inlet concentration on profile position. Variable temperature reaction profiles simulated with Eq. 2.10 and Eq. 2.12 for a heterogeneously-catalyzed reaction with rate law  $-r_a = k C_a^n$ , conducted in a packed-bed reactor. Parameter values:  $\tau_{\text{ref}} = 1.8 \times 10^4 \text{ g}_{\text{cat}} \text{ s m}^{-3}$ ,  $E_a = 100 \text{ kJ mol}^{-1}$ ,  $A = 1 \times 10^8$  (units depend on reaction order).  $C_{0,\text{ref}}$  was varied from 0.0225 to 0.045 to 0.090  $\text{mol m}^{-3}$ , increasing in the direction of the arrows for  $n = 0$  and 2.

For overall reaction orders less than 1, reaction profiles simulated with the same reactor and activation parameters are shifted to significantly lower temperatures relative to the corresponding first-order reaction profiles. The rate acceleration with temperature is faster because the deceleration caused by decreasing concentration at high conversion is attenuated, (indeed, there is no deceleration for  $n \leq 0$ , and the shape of the profile is non-sigmoidal). Increasing  $C_{a,0}$  displaces the reaction profile to higher temperatures, because of the higher concentration dependence of  $X$  in the reactor design equation relative to the rate law. In contrast, a reaction order higher than 1 causes the sigmoidal reaction profile to shift to significantly higher temperatures, and the entire profile extends over a much wider

temperature range. For this case, increasing  $C_{a,0}$  displaces the profile to lower temperatures, because of the lower concentration dependence of  $X$  in the reactor design equation relative to the rate law. Understanding this qualitative trend in profile positions with inlet concentration, one could quickly generate a series of reaction profiles for different inlet concentrations as a diagnostic tool to quickly assess the reaction rate law. This test could give rapid insight into the order of a reaction and give evidence to suggest or refute a claim as to what the reaction order(s) are.

Reaction profiles were simulated for bimolecular reactions using Eq. 2.15 – 2.16 in order to observe the effect of varying the concentration of the excess reagent,  $\mathbf{b}$ , and thus  $\Theta_{\mathbf{b}}$ . Reaction orders were chosen to simulate CO oxidation under CO-lean conditions ( $n = -1, m = +1$ ) and CO rich conditions ( $n = +1, m = -1$ ). Additionally, a net second-order ( $n = +1, m = +1$ ) rate law was simulated. For each set of reaction orders the excess ratio  $\Theta_{\mathbf{b}}$  was set to 10, 50, and 100, Fig. 2.3. The reaction profiles shift to a lower value of  $T_{50}$  for the CO-lean (green curves) and second-order (blue curves) when the concentration of excess reagent is increased. However the CO-rich (dashed red curves) profiles move to larger values of  $T_{50}$  as  $\Theta_{\mathbf{b}}$  increases.

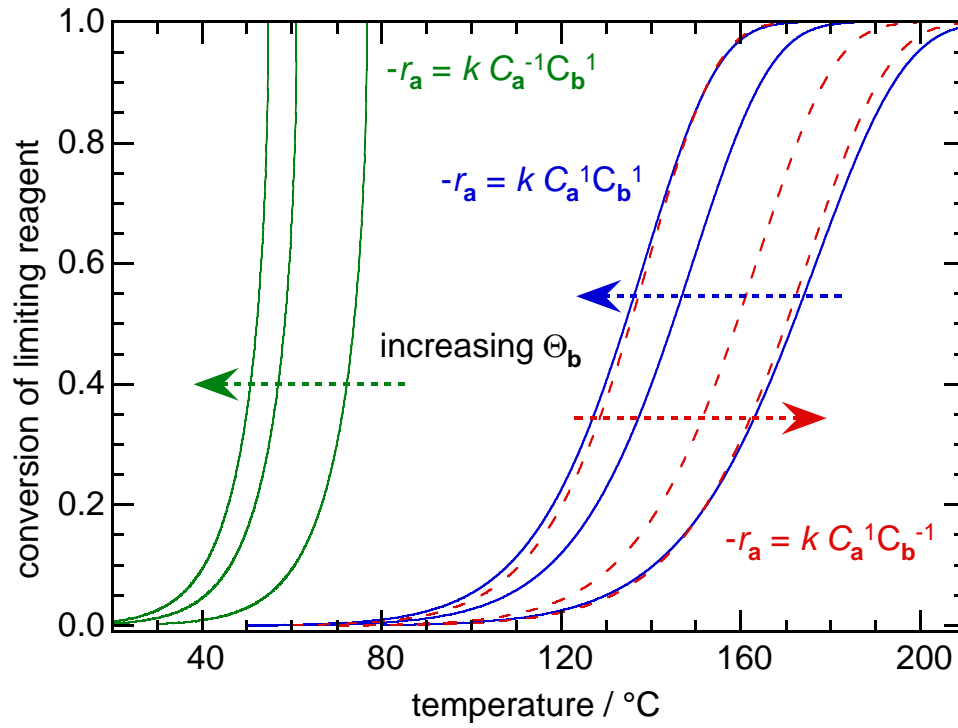


**Fig. 2.3.** Effect of excess reactant concentration.

Variable temperature reaction profiles simulated with Eq. 2.15 – 2.16 for a heterogeneously-catalyzed reaction with rate law  $-r_a = k C_a^n C_b^m$ , conducted in a packed-bed reactor. Parameter values:  $\tau_{\text{ref}} = 1.8 \times 10^4 \text{ g}_{\text{cat}} \text{ s m}^{-3}$ ,  $C_{a,0,\text{ref}} = 0.045 \text{ mol m}^{-3}$ ,  $E_a = 100 \text{ kJ mol}^{-1}$ , and  $A = 1 \times 10^8$  (units depend on reaction order). The ratio of the inlet concentrations,  $\Theta_b$ , was modeled equal to 10, 50, and 100. The arrows correspond to increasing the excess reactant concentration.



### 2.3.3. Effects of reaction order, residence time, and Arrhenius parameters on reaction profiles

To aid in visually comparing their shapes, simulated reaction profiles with various reaction orders are aligned at the same  $T_{50}$  value in Fig. 2.4. The inset to Fig. 2.4 shows that  $T_{50}$  also changes dramatically as the overall reaction order changes, even when all other kinetic parameters have the same numerical values. In this example,  $T_{50}$  increases from 64 to 101, 152 and 225 °C as the order in the limiting reagent changes from -1 to 0, 1 and 2, respectively.

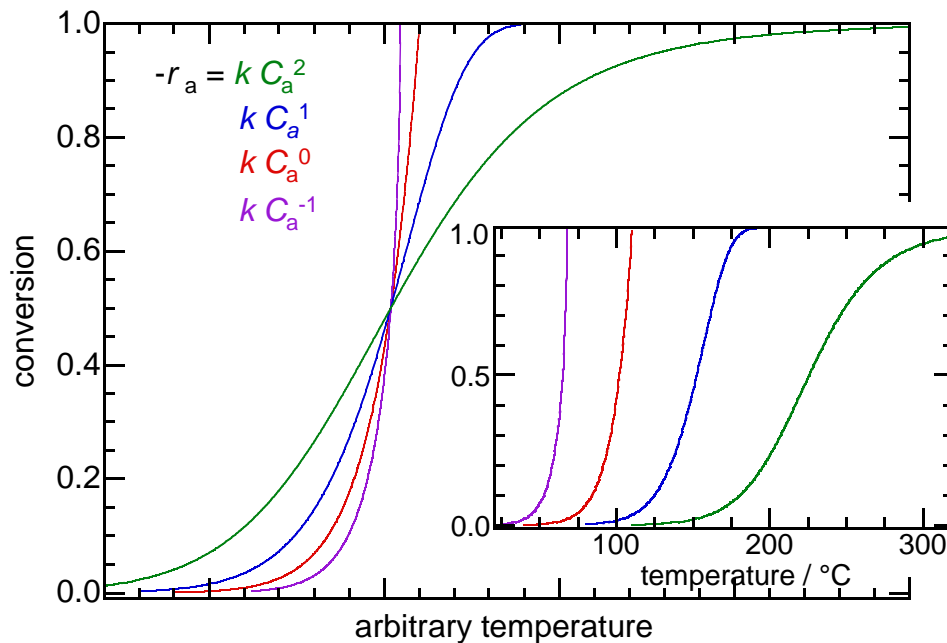


**Fig. 2.4.** Comparison of shape and position for unimolecular rate laws.

Variable temperature reaction profiles simulated with Eq. 2.10 and Eq. 2.12 for four rate laws with a single concentration term. Reaction profiles are aligned to a single  $T_{50}$  to emphasize differences in shape. The inset shows the unaligned reaction profiles. Simulation parameters:  $C_{0,\text{ref}} = 0.045 \text{ mol m}^{-3}$ ,  $\tau_{\text{ref}} = 1.8 \times 10^4 \text{ g}_{\text{cat}} \text{ s m}^{-3}$ ,  $A = 1 \times 10^8$  (units depend on the reaction order),  $E_a = 100 \text{ kJ mol}^{-1}$ .

Increasing the catalyst loading and/or decreasing the volumetric flow rate causes  $\tau$  to increase, which in turn causes  $T_{50}$  to decrease, as shown in Fig. 2.5A for a reaction with a first-order rate law (simulated using Eq. 2.10). Increasing the Arrhenius pre-exponential factor also shifts the reaction profile to lower temperatures, Fig. 2.5B. Since Eq. 2.10 contains the product of  $A$  and  $\tau$ , a change in one parameter is indistinguishable from an equivalent change in the other. As expected, changes in  $E_a$  have the largest effect on the position of the reaction profile: a 5 % change in the value shifts the reaction profile by 22 °C, Fig. 2.5C. In contrast, either  $A$  or  $\tau$  must change by a factor of 5 to cause a similar change in  $T_{50}$  (26 °C).

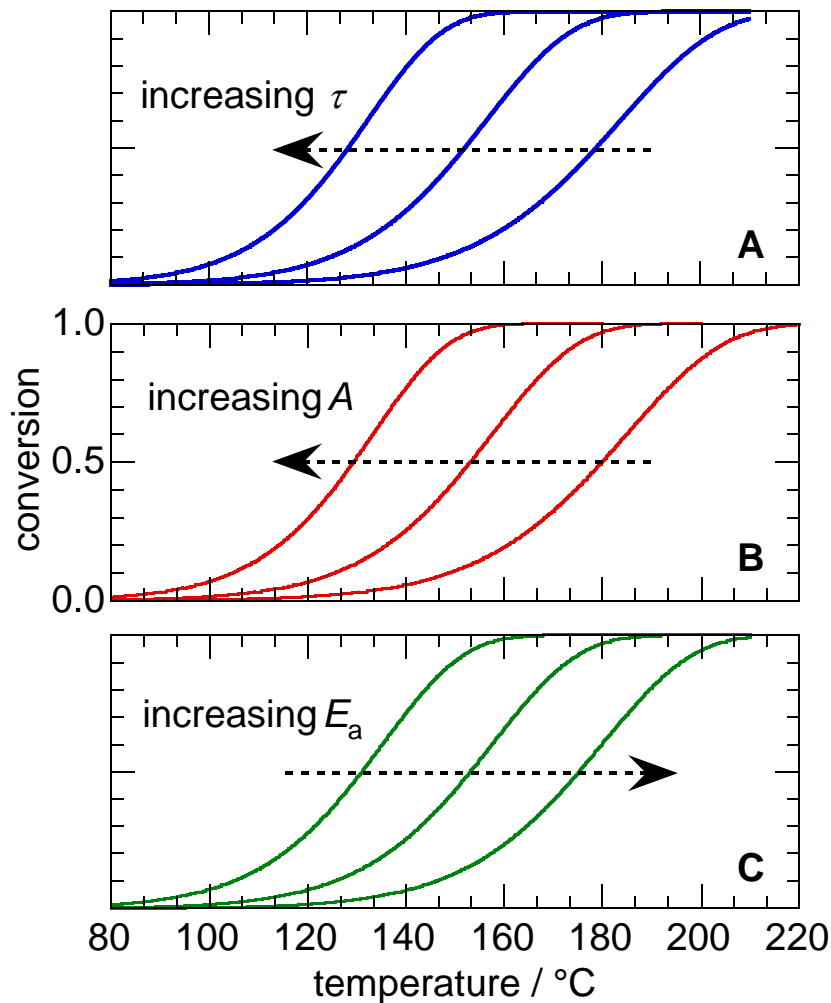


**Fig. 2.5.** Effect of  $\tau$ ,  $A$ , and  $E_a$  on reaction profiles.

Simulated variable temperature reaction profiles with Eq. 2.10 for a first-order rate law with a single concentration term. The simulation parameters for the middle profile in each set are:  $C_{0,\text{ref}} = 0.045 \text{ mol m}^{-3}$ ,  $\tau_{\text{ref}} = 1.8 \times 10^4 \text{ g}_{\text{cat}} \text{ s m}^{-3}$ ,  $A = 1 \times 10^8 \text{ m}^3 \text{ g}_{\text{cat}}^{-1} \text{ s}^{-1}$ ,  $E_a = 100 \text{ kJ mol}^{-1}$ .

(A) Effect of a five-fold increase or decrease in  $\tau$  (i.e., by changing either  $v_0$  or  $W$ ); (B) effect of a five-fold increase or decrease in  $A$ ; and (C) effect of a 5 % increase or decrease in  $E_a$ .

As the inset to Fig. 2.4 demonstrates, an integer increase in the reaction order  $n$  causes a dramatic increase in  $T_{50}$ , even when the activation energy remains the same. Furthermore, the magnitude of  $\Delta T_{50}$  increases with the reaction order (e.g., from 37 °C when  $n$  changes from -1 to 0, up to 73 °C when  $n$  changes from 1 to 2). To cause a similar shift in  $T_{50}$ , the rate constant must change by a factor of ten. For example, a ten-fold decrease in  $A$  causes  $T_{50}$  for a first-order reaction to increase by 39 °C, whereas a change in the reaction order to  $n = 0$  causes  $T_{50}$  to decrease by 51 °C.

Simulated profiles for bimolecular reactions with various reaction orders show that each rate law gives a profile with a distinctive shape and position, Fig. 2.6. Rate laws that depend on two species (**a** and **b**) were modeled with a large excess ( $\Theta_b = 50$ ), as well as for a limiting L-H rate law at stoichiometric conditions ( $\Theta_b = b/a$ ). Rate laws that depend on two species in which the limiting reactant has a reaction order of one have a similar shape when  $\Theta_b \gg b/a$ . When the second reactant is inhibiting ( $m = -1$ ), the activity increases slower under, and faster above  $X = 0.5$ , compared to the case in which the rate depends on only one concentration. The opposite is true when the excess reactant has a positive reaction order. Inverse-first order behavior is observed for a limiting L-H rate law ( $n = -1$ ,  $m = 1$ ) with large excess. The shape of a simulated profile for a bimolecular rate law is similar to the shape of a profile for a unimolecular rate law provided the reaction order of the limiting reactant is the same. The limiting L-H rate law modeled for a stoichiometric reaction is nearly identical in shape to the pseudo-zeroth-order rate law. Simulated profiles where the reaction order with respect to the limiting reactant is inverse-first order or zeroth order contains a discontinuity at maximum conversion that is absent when the limiting reactant has a positive reaction order.

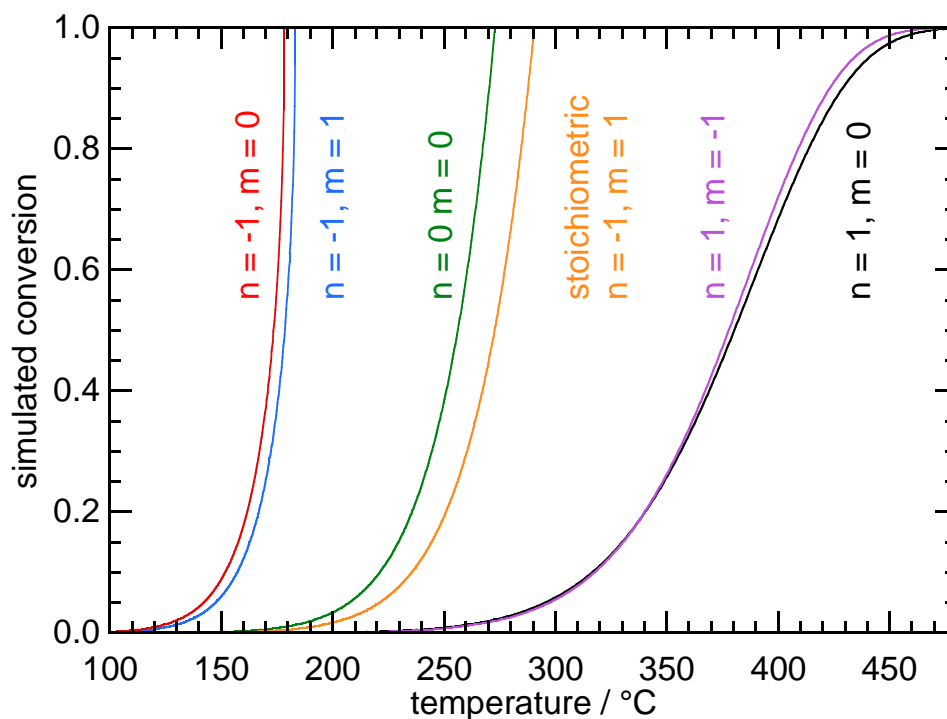


**Fig. 2.6.** Comparison of bimolecular and unimolecular rate laws.

Simulated variable temperature reaction profiles with Eqs. 2.12, 2.15 – 2.16.  $C_{0,\text{ref}} = 0.045 \text{ mol m}^{-3}$ ,  $\tau_{\text{ref}} = 1.8 \times 10^4 \text{ g}_{\text{cat}} \text{ s m}^{-3}$ ,  $A = 1 \times 10^8 \text{ m}^3 \text{ g}_{\text{cat}}^{-1} \text{ s}^{-1}$ ,  $E_a = 100 \text{ kJ mol}^{-1}$ . **(A)** Effect of a five-fold increase or decrease in  $\tau$  (i.e., by changing either  $v_0$  or  $W$ ); **(B)** effect of a five-fold increase or decrease in  $A$ ; and **(C)** effect of a 5 % increase or decrease in  $E_a$ .

## 2.4. Conclusions

Bimolecular surface reactions generally follow Langmuir-Hinshelwood-type mechanisms, which give rise to rate laws with large numbers of adjustable parameters. Their precise formulation remains an open topic for discussion even in nominally simple systems, such as CO oxidation over noble metal catalysts [21, 22]. Fortunately, adsorption/desorption phenomena are often rapid relative to surface reactions over the range of conditions sampled in a single reaction profile, making it possible to describe the rate using a simple power law, as shown in Eq. 2.4.

Both the shape and the position of the reaction profile are influenced by the reaction order with respect to the limiting reactant. At high excess, simulated reaction profiles are dominated by the order of reaction with respect to the limiting reactant, while at small to no excess an intermediate case exists. The position of reaction profiles changes with kinetic and reactor parameters such as  $E_a$ ,  $C_{i,0}$ , and  $\tau$ , and the nature of the change is dependent on the rate law. Therefore simple diagnostic tests where one or more parameters are varied can give experimentalists a general understanding of the rate law based solely on the shape and position of the reaction profile.

The analytical variable-temperature reaction profile equations developed here are applicable to kinetically-limited reactions occurring in a packed bed reactor. These equations can be simulated, assuming the kinetics are understood, to predict how the reaction will respond to a change allowing researchers to forego experiments. In principle these equations allow for the rapid quantitative analysis of experimental reaction profiles through curve-fitting variable-temperature reaction profiles.

## References

- [1] X.D. Xiang, X.D. Sun, G. Briceno, Y.L. Lou, K.A. Wang, H.Y. Chang, W.G. Wallace-Freedman, S.W. Chen, P.G. Schultz, A combinatorial approach to materials discovery, *Science* 268 (1995) 1738-1740.
- [2] A. Hagemeyer, B. Jandeleit, Y.M. Liu, D.M. Poojary, H.W. Turner, A.F. Volpe, W.H. Weinberg, Applications of combinatorial methods in catalysis, *Appl. Catal. A: Gen.* 221 (2001) 23-43.
- [3] B. Jandeleit, D.J. Schaefer, T.S. Powers, H.W. Turner, W.H. Weinberg, Combinatorial materials science and catalysis, *Angew. Chem. Int. Ed.* 38 (1999) 2495-2532.
- [4] S.M. Senkan, S. Ozturk, Discovery and optimization of heterogeneous catalysts by using combinatorial chemistry, *Angew. Chem. Int. Ed.* 38 (1999) 791-795.
- [5] M. Boudart, Turnover rates in heterogeneous catalysis, *Chem. Rev.* 95 (1995) 661-666.
- [6] S. Kozuch, J.M.L. Martin, "Turning Over" Definitions in Catalytic Cycles, *ACS Catal.* 2 (2012) 2787-2794.
- [7] G. Lente, Comment on "'Turning over' definitions in catalytic cycles", *ACS Catal.* 3 (2013) 381-382.
- [8] E.J. Peterson, A.T. Delariva, S. Lin, R.S. Johnson, H. Guo, J.T. Miller, J.H. Kwak, C.H.F. Peden, B. Kiefer, L.F. Allard, F.H. Ribeiro, A.K. Datye, Low-temperature carbon monoxide oxidation catalysed by regenerable atomically dispersed palladium on alumina, *Nat. Commun.* 5 (2014).
- [9] J.R. Kittrell, W.G. Hunter, C.C. Watson, Nonlinear least squares analysis of catalytic rate models, *AIChE J.* 11 (1965) 1051-1057.
- [10] D.J. Pritchard, D.W. Bacon, Statistical assessment of chemical kinetic models, *Chem. Eng. Sci.* 30 (1975) 567-574.
- [11] M. Schwaab, J.C. Pinto, Optimum reference temperature for reparameterization of the Arrhenius equation. Part 1: Problems involving one kinetic constant, *Chem. Eng. Sci.* 62 (2007) 2750-2764.
- [12] E. Koch, *Non-isothermal reaction analysis*, Academic Press, New York, 1977.
- [13] B.W. Wojciechowski, N.M. Rice, *Experimental methods in kinetic studies*, Elsevier, Boston, 2003.
- [14] F.V. Hanson, M. Boudart, Reaction between  $H_2$  and  $O_2$  over supported platinum catalysts, *J. Catal.* 53 (1978) 56-67.
- [15] F. Mahoney, R. Rudham, J.V. Summers, Hydrogen oxidation catalyzed by X zeolite containing transition-metal ions, *J. Chem. Soc. Faraday Trans. 1* 75 (1979) 314-322.
- [16] C.F. Cullis, T.G. Nevell, Kinetics of catalytic-oxidation over palladium of some alkanes and cycloalkanes, *Proc. Roy. Soc. Lond. A* 349 (1976) 523-534.
- [17] Y.F.Y. Yao, Oxidation of alkanes over noble metal catalysts, *Ind. Eng. Chem. Prod. Res. Dev.* 19 (1980) 293-298.
- [18] P.J. Berlowitz, C.H.F. Peden, D.W. Goodman, Kinetics of CO oxidation on single-crystal Pd, Pt, and Ir, *J. Phys. Chem.* 92 (1988) 5213-5221.
- [19] T. Engel, G. Ertl, Molecular beam investigation of catalytic oxidation of CO on Pd (111), *J. Chem. Phys.* 69 (1978) 1267-1281.
- [20] Y.F.Y. Yao, The oxidation of CO and hydrocarbons over noble-metal catalysts, *J. Catal.* 87 (1984) 152-162.

- [21] A.D. Allian, K. Takanabe, K.L. Fajdala, X. Hao, T.J. Truex, J. Cai, C. Buda, M. Neurock, E. Iglesia, Chemisorption of CO and mechanism of CO oxidation on supported platinum nanoclusters, *J. Am. Chem. Soc.* 133 (2011) 4498-4517.
- [22] J. Saavedra, H.A. Doan, C.J. Pursell, L.C. Grabow, B.D. Chandler, The critical role of water at the gold-titania interface in catalytic CO oxidation, *Science* 345 (2014) 1599-1602.



## Chapter 3: Rapid Extraction of Information from Kinetically-Limited Experimental Reaction Profiles

### 3.1. Experimental Methods

#### 3.1.1. Materials

The catalyst selected to explore reaction profile analysis is 2.0 wt% PdO supported on  $\gamma$ -Al<sub>2</sub>O<sub>3</sub> (Sasol HTA-102, surface area 76 m<sup>2</sup> g<sup>-1</sup>, pore volume 0.60 cm<sup>3</sup> g<sup>-1</sup>, median pore radius 15 nm), hereafter called Pd/Al<sub>2</sub>O<sub>3</sub>. It was prepared by incipient wetness impregnation of the  $\gamma$ -Al<sub>2</sub>O<sub>3</sub> with aqueous Pd(NO<sub>3</sub>)<sub>2</sub> (Heraeus, 99.99 %). The resulting solid has an average Pd particle size of (2.8 ± 0.6) Å (assessed by transmission electron microscopy). The as-prepared catalyst was dried in air at 100 °C, followed by calcination at 150 °C for 2 h, 450 °C for 2 h, and 600 °C for 4 h. To minimize the formation of hot spots in the catalyst bed, the resulting powder (40 mg) was sieved to a mesh size of 80/100 (150-180 μm) and diluted with SiC (Sigma Aldrich, >97.5 %, 200 mesh size) in a 1:3 ratio (w/w), unless specified otherwise.

All high purity gasses were supplied by Praxair: Ar (99.999 %), O<sub>2</sub> (99.99 %, and 5000 ppm in Ar, 99.99 %), CO<sub>2</sub> (5000 ppm in Ar, 99.99 %), CO (5005 ppm in Ar, 99.99 %), C<sub>3</sub>H<sub>8</sub> (5138 ppm in Ar, 99.99 %) and H<sub>2</sub> (4913 ppm in Ar, 99.99 %).

#### 3.1.2. Catalytic reaction conditions

Complete oxidation of H<sub>2</sub>, C<sub>3</sub>H<sub>8</sub>, and CO, each catalyzed by Pd/Al<sub>2</sub>O<sub>3</sub> in the presence of O<sub>2</sub>, were chosen as test reactions, in part because their limiting rate laws are

simple and there no side-reactions are expected. In addition, their activation parameters vary little with conversion over the range of reaction conditions studied (see below). For  $\text{H}_2$  oxidation, reaction profiles were recorded under  $\text{O}_2$ -rich conditions relevant to diesel oxidation catalysts (1000 ppm  $\text{H}_2$ , 100 000 ppm  $\text{O}_2$ , balanced by Ar). In this concentration regime, the reaction orders are 0 and 1 with respect to  $\text{O}_2$  and  $\text{H}_2$ , for  $\text{H}_2$  oxidation over transition metals [1]. Reaction profiles for  $\text{C}_3\text{H}_8$  oxidation were also recorded in an  $\text{O}_2$ -rich atmosphere (1000 ppm  $\text{C}_3\text{H}_8$ , 100 000 ppm  $\text{O}_2$ , balanced by Ar). Under these conditions, the reaction orders with respect to  $\text{O}_2$  and  $\text{C}_3\text{H}_8$  are 0 and 1, respectively, over Pd-based catalysts [2].

CO oxidation was conducted with *equimolar* reactant concentrations ( $C_{\text{CO},0} = C_{\text{O}_2,0} = 1000$  ppm, balanced by Ar), relevant to three-way catalysis. Over Pd-based catalysts, CO generally inhibits the reaction rate because its low-temperature adsorption on the metal is more favorable than that of  $\text{O}_2$  [3]. The experimentally-determined reaction orders are +1 and -1 with respect to  $\text{O}_2$  and CO [3], resulting in an overall reaction order of zero when the inlet concentrations are similar.

### 3.1.3. Recording reaction profiles

Variable-temperature kinetic experiments were carried out in a CATLAB micro-reactor (Hiden Analytical). The tubular quartz reactor has an inner diameter of 3.88 mm. The short catalyst bed (< 4 mm) was held in place between two plugs of quartz wool, giving a typical catalyst bed volume of  $5 \times 10^{-8} \text{ m}^3$  (0.05 mL). The pressure drop across the bed was measured to be less than 70 mbar. Since the catalyst bed is essentially isothermal during each measurement, the temperature of the entire reactor is described by a single value, measured by a K-type thermocouple (Omega KQXL, 0.05 s response time) in contact with

the front end of the catalyst bed. During variable temperature experiments, the reactor was heated in a tube furnace at a constant rate of  $5 \text{ K min}^{-1}$ . The composition of the effluent gas stream was monitored using a close-coupled online quadrupole mass spectrometer (HR-20, Hiden Analytical). A secondary electron multiplier (SEM) detector was used to monitor signals for  $\text{CO}_2$  ( $m/z = 44$ ),  $\text{H}_2$  ( $m/z = 2$ ), or  $\text{C}_3\text{H}_8$  (via its ethyl fragment, at  $m/z = 29$ ), whose intensities were recorded every 0.6 s. The reactor setup and experimental design are shown schematically in Fig. 3.1.

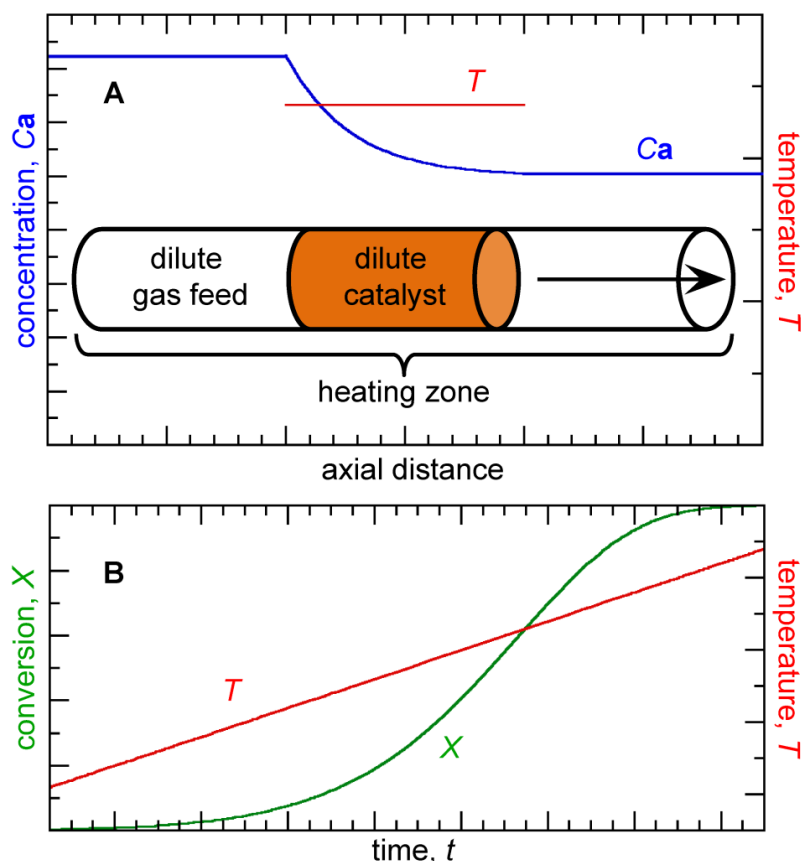


**Fig. 3.1.** Reactor schematic.

(A) Reactor scheme for variable-temperature kinetics experiment in a tubular packed-bed reactor. The reactor inlet and outlet as well as the catalyst bed (orange) are heated in a tube furnace. At any given time, the entire reactor temperature is essentially constant, while the concentration of the limiting reactant **a** decreases as a function of axial distance. (B) The variable-temperature reaction profile is constructed from analysis of the effluent gas while the reactor temperature of the reactor is ramped at constant  $dT/dt$ .

For reproducibility, each catalyst sample was pre-treated in a flow of the appropriate feed gas for 3 h at a temperature for which the conversion of the limiting reactant was slightly greater than 0.95. Reactant gas flow rates were varied using mass flow controllers (3 – 100 mL min<sup>-1</sup>). A series of reaction profiles was recorded for volumetric flow rates between 25 and 70 mL min<sup>-1</sup> (corresponding to gas-hourly space velocities, GHSV, of 3 – 9 x 10<sup>4</sup> h<sup>-1</sup>), varying in random order. At each flow rate, three reaction profiles were recorded sequentially. For H<sub>2</sub> and C<sub>3</sub>H<sub>8</sub> oxidation, conversion was calculated from the loss of signal intensity for the limiting reactant,  $I_a$ , Eq. 3.1, while for CO oxidation, the yield of the product CO<sub>2</sub>,  $I_{CO_2}$ , was monitored, Eq. 3.2.

$$X = \frac{(I_{in} - I_{zero}) - (I_a - I_{zero})}{I_{in} - I_{zero}} = \frac{I_{in} - I_a}{I_{in} - I_{zero}} \quad (3.1)$$

$$X = \frac{I_{CO_2} - I_{zero}}{I_{calibration} - I_{zero}} \quad (3.2)$$

$I_{zero}$  corresponds to the signal intensity recorded at full conversion (for 0 ppm),  $I_{in}$  corresponds to the maximum inlet signal intensity (below the onset of activity), and  $I_{calibration}$  is the signal for the calibration gas (CO<sub>2</sub>) measured at the same flow rate.

### 3.1.4. Minimization of non-kinetic effects

Heat and mass transfer effects must be negligible to allow for curve-fitting of the analytical VTK equations described below to the reaction profiles, and to ensure that parameters extracted from these profiles are purely kinetic. In order to minimize non-kinetic effects, experiments were conducted with large amounts of inert diluents (Ar, SiC) in both the feed gas and in the catalyst bed. The possible contributions of external and internal mass

transfer as well as heat transfer to the observed reaction rates are negligible according to Mears' criterion [4], the Weisz-Prater criterion [5], and Mears' heat criterion [6] (see Appendix 3 for sample calculations).

Possible contributions from non-kinetic effects were also assessed experimentally. Reaction profiles were typically recorded with ca. 11 mg catalyst sieved to 150 – 180  $\mu\text{m}$  and diluted 1:3 with SiC, at a temperature ramp rate of 5 K  $\text{min}^{-1}$ . Reaction profiles for propane oxidation recorded for different reactor loadings of catalyst, while keeping constant the ratio of catalyst mass to volumetric flow rate [4], are nearly superposable (Fig. A3.1). Rates for propane oxidation did not change with catalyst particle diameter (Fig. A3.1). Thus external and internal mass transfer rates do not affect the observed reaction rates significantly. The absence of thermal lag due to the heat of reaction was verified experimentally. Reaction profiles for  $\text{H}_2$  oxidation recorded at temperature ramp rates from 2 – 7 K  $\text{min}^{-1}$  resulted in identical  $T_{50}$  values and near-superposable curves (Fig. A3.3), attesting to the absence of thermal lag for this reactor configuration. Finally, reaction profiles for propane oxidation were unaffected by the catalyst dilution ratio (Fig. A3.2).

The use of a temperature ramp rate that is slow relative to the reactor residence time (ca. 0.001 min) ensures negligible accumulation of heat due to reaction, so that the catalyst bed remains near-isothermal during each measurement of conversion at a particular reactor temperature. In CO oxidation at an overall conversion of 0.2, the measured bed entrance and exit temperatures were the same, 120  $^{\circ}\text{C}$ , within the measurement uncertainty. At full conversion, the bed exit temperature (150  $^{\circ}\text{C}$ ) was slightly higher than the entrance temperature (149  $^{\circ}\text{C}$ ). Consequently, we assumed that axial temperature gradients were negligible, and that the temperature of the entire bed can be described by a single value

measured at the entrance. In a recent series of CO oxidation experiments conducted using similar conditions (1000 ppm CO, 10% O<sub>2</sub> flowing at 50 mL min<sup>-1</sup> over undiluted 4 wt% Pt/Al<sub>2</sub>O<sub>3</sub> in a reactor with an inner diameter of 1.7 mm), temperatures across the entire catalyst bed were measured directly using IR thermography [7]. The maximum difference in local temperatures was only 2 °C. In our experiments, the use of inert diluents for both the feed gas and the catalyst bed are expected to result in even smaller temperature variations [6].

### 3.1.5. Curve-fitting reaction profiles

Reaction profiles were analyzed individually, as well as simultaneously (i.e., globally), for a series of profiles recorded with different volumetric flow rates, via non-linear least-squares refinement to the kinetic equations. The Arrhenius relationship for the rate constant, design equation for a packed bed reactor, and a power rate law were integrated and solved analytically for conversion. The solution for a bimolecular power rate law in which the reaction order with respect to the limiting reactant is first-order was fitted to experimental reaction profiles, Eq. 3.3. A bimolecular rate law in which the reaction orders with respect to the limiting and excess reactants are unknown and left as variables  $n$  and  $m$ , respectively, was also used, Eq. 3.4.

$$X = 1 - \exp \left[ -\tau_{\text{ref}} \left( \frac{T_{\text{ref}}}{T} \right) \Theta_{\text{b}}^m A e^{-\frac{E_a}{RT}} \right] \quad (3.3)$$

$$X = 1 - \left[ 1 + (n - 1) \tau_{\text{ref}} C_{\text{a},0,\text{ref}}^{n+m-1} \left( \frac{T_{\text{ref}}}{T} \right)^{n+m} \Theta_{\text{b}}^m A e^{-\frac{E_a}{RT}} \right]^{\frac{1}{1-n}} \quad (3.4)$$

Analyses were performed using either Origin (OriginLab) or Kaleidagraph (Synergy Software). Initial parameter guesses for the activation parameters  $A$  and  $E_a$  were chosen based on previously reported values, and/or values estimated using  $(X,T)$  data from the differential region of the reaction profile. The results are not sensitive to changes in these initial values. In individual curve-fits,  $A$  and  $E_a$  were refined, as well as one or two reaction orders (as specified below). In simultaneous curve-fits to multiple reaction profiles,  $E_a$  and the reaction order for each reactant were refined as global fit parameters. Initial values for the reaction orders were chosen based on literature values as well as visual inspection of the shapes of the profiles. Since the pre-exponential term  $A$  appears in the curve-fitting equations as the product  $A\tau$ , where  $\tau$  is the varying space-time ( $\tau$ ),  $A\tau$  was refined as a separate parameter for each reaction profile to reduce the impact of experimental error in  $\tau$  on refinement of  $A$ . The reported value of  $A$  is the average for all reaction profiles. A curve-fit was judged acceptable if the residuals were random and the refined parameters were physically reasonable. Furthermore, it was possible to truncate experimental reaction profiles to variable extents without significantly changing the values of refined parameters.

The uncertainty  $\sigma_{E_a}$  was estimated using full error propagation according to Eq. 3.5, where  $\sigma_T$  and  $\sigma_{r_a}$  are the estimated uncertainties in the temperature and rate, respectively, and  $\Delta T$  and  $\Delta(\ln[-r_a])$  are the ranges of  $T$  and  $-r_a$ , respectively, used in the analysis [8].

$$(\sigma_{E_a}/E_a)^2 = 2(T\sigma_T/(T\Delta T))^2 + 2(\Delta(\ln[-r_a])^{-2}(\sigma_{r_a}/-r_a)^2 \quad (3.5)$$

The uncertainty in  $A$  was estimated as the standard deviation of the average for all pre-exponential values. To estimate the uncertainty in the rate laws with two variable reaction

orders, one reaction order was fixed to its refined value while the other was fixed manually above and below its original curve-fitted value until either  $E_a$  or  $A$  exceeded its predetermined uncertainty.

### 3.1.6. Conventional kinetic analysis

After all reaction profiles had been recorded under a given set of reaction conditions, the reactor was operated at steady-state for several temperatures corresponding to  $0.01 < X < 0.10$ . The reaction rate was calculated, then  $E_a$  was obtained from the slope of an Arrhenius plot constructed using  $\ln(-r_a)$  vs.  $T^{-1}$ . The uncertainty  $\sigma_A$  was calculated using error propagation analogous to Eq. 3.5 (replacing  $\sigma_{E_a}$  and  $E_a$  by  $\sigma_A$  and  $A$ , respectively). Arrhenius plots were also constructed by plotting  $\ln(k)$  vs.  $T^{-1}$ , where  $k$  values were calculated according to a power rate law, using appropriate integer reaction orders obtained from the literature. Sample calculations can be found in Appendix 3.

## 3.2. Linear analysis of differential kinetic data

Three different catalytic reactions were studied in the presence of a Pd/Al<sub>2</sub>O<sub>3</sub> catalyst. In order to validate kinetic parameters for the reactions of H<sub>2</sub>, C<sub>3</sub>H<sub>8</sub>, and CO with O<sub>2</sub> obtained by analysis of their variable-temperature reaction profiles (see below) using non-linear curve-fitting, we also measured steady-state conversions under differential conditions. Under the conditions of interest here, the rate laws for all three reactions can be represented by a simple power law. Arrhenius plots were constructed using reaction rates (which yield accurate values for  $E_a$  only when measured under differential conditions,  $X < 0.1$ , see Appendix 3). The formulation of the rate law in the packed bed reactor design equation reveals a key unstated assumption in the direct use of  $X$ ,  $-r_a$  or TOF to create



Arrhenius plots, namely, that all variables other than  $k$  (i.e.,  $F_{a,0}$  and  $C_i$ ) are temperature-independent. This assumption is indeed reasonable when the conversion is low, since all such terms are approximately constant. In addition, while  $E_a$  can always be extracted from the differential Arrhenius slope, the  $y$ -intercept yields an accurate value for  $A$  only with the much stricter condition that  $X \approx 0$ . Arrhenius plots were also constructed using apparent rate constants (by fixing reaction orders to values obtained in previous studies), in order to obtain physically meaningful values for  $A$ . The results are shown in Figs. A3.5-3.7 and Table 3.1.

**Table 3.1.** Comparison of apparent Arrhenius parameters extracted by linearization of data from differential, steady-state experiments with those obtained by non-linear curve-fitting of integral, variable-temperature reaction profiles

Reaction	$\Theta_b$	Steady-state analysis <sup>a</sup>			VTK analysis <sup>b</sup>	
		Dependent variable	$A$	$E_a$ kJ mol <sup>-1</sup>	$A$	$E_a$ kJ mol <sup>-1</sup>
$H_2 + \frac{1}{2} O_2 \rightarrow H_2O^c$	200	$-r_a$		58 ± 6		
		$k$	$(1.4 \pm 0.1) \times 10^4$	61 ± 6	$(5 \pm 1) \times 10^4$	66 ± 2
$C_3H_8 + 5 O_2 \rightarrow 3 CO_2 + 4 H_2O^d$	100	$-r_a$		118 ± 10		
		$k$	$(4.5 \pm 0.4) \times 10^7$	124 ± 10	$(1.0 \pm 0.3) \times 10^7$	114 ± 3
$CO + \frac{1}{2} O_2 \rightarrow CO_2^e$	1	$-r_a$		91 ± 6		
		$k$	$(1.5 \pm 0.1) \times 10^5$	89 ± 6	$(3 \pm 2) \times 10^6$	98 ± 3

<sup>a</sup> Ca. 10 mg Pd/Al<sub>2</sub>O<sub>3</sub> diluted 1:3 with SiC,  $v_0 = 50$  mL min<sup>-1</sup>,  $0.01 < X < 0.10$ . Six to nine isothermal measurements were made, covering a temperature range of 25 °C. Uncertainties were obtained by full error propagation similar to Eq. 3.5.

<sup>b</sup> Ca. 11 mg Pd/Al<sub>2</sub>O<sub>3</sub> diluted 1:3 with SiC. Uncertainties from the standard deviation of the average value for duplicate runs at five different volumetric flow rates (typically,  $v_0 = 25 - 70$  mL min<sup>-1</sup>, GHSV = 3.2 – 8.9 x 10<sup>4</sup> h<sup>-1</sup>).

<sup>c</sup>  $C_{H_2,0} = 500$  ppm,  $C_{O_2,0} = 100\ 000$  ppm. Reaction orders fixed at +1 and 0 for H<sub>2</sub> and O<sub>2</sub>, respectively [1]. Dimensions of  $A$  are m<sup>3</sup> g<sub>cat</sub><sup>-1</sup> s<sup>-1</sup>.

<sup>d</sup>  $C_{C_3H_8,0} = 1000$  ppm,  $C_{O_2,0} = 100\ 000$  ppm. Reaction orders fixed at +1 and 0 for C<sub>3</sub>H<sub>8</sub> and O<sub>2</sub>, respectively [2]. Dimensions of  $A$  are m<sup>3</sup> g<sub>cat</sub><sup>-1</sup> s<sup>-1</sup>.

<sup>e</sup>  $C_{CO,0} = 1000$  ppm,  $C_{O_2,0} = 1000$  ppm. Reaction orders fixed at -1 and +1 for CO and O<sub>2</sub>, respectively [3]. Dimensions of  $A$  are mol<sub>CO</sub> g<sub>cat</sub><sup>-1</sup> s<sup>-1</sup>.

### 3.3. Extracting kinetic parameters from variable-temperature reaction profiles

#### 3.3.1. Curve-fitting of individual reaction profiles for H<sub>2</sub> oxidation

Reaction profiles for H<sub>2</sub> oxidation catalyzed by Pd/Al<sub>2</sub>O<sub>3</sub> were recorded with a large excess of O<sub>2</sub> ( $C_{\text{H}_2,0} = 1000$  ppm;  $C_{\text{O}_2,0} = 100\,000$  ppm). At each volumetric flow rate, three sigmoidal reaction profiles were recorded, and are superposable (Fig. A3.8). This finding demonstrates that catalyst deactivation is negligible. For two of the flow rates, the third reaction profile of each series is shown in Fig 3.2. Increasing  $v_0$  from 30 to 70 mL min<sup>-1</sup> causes  $T_{50}$  to increase (Fig. 3.5), as predicted by simulations.

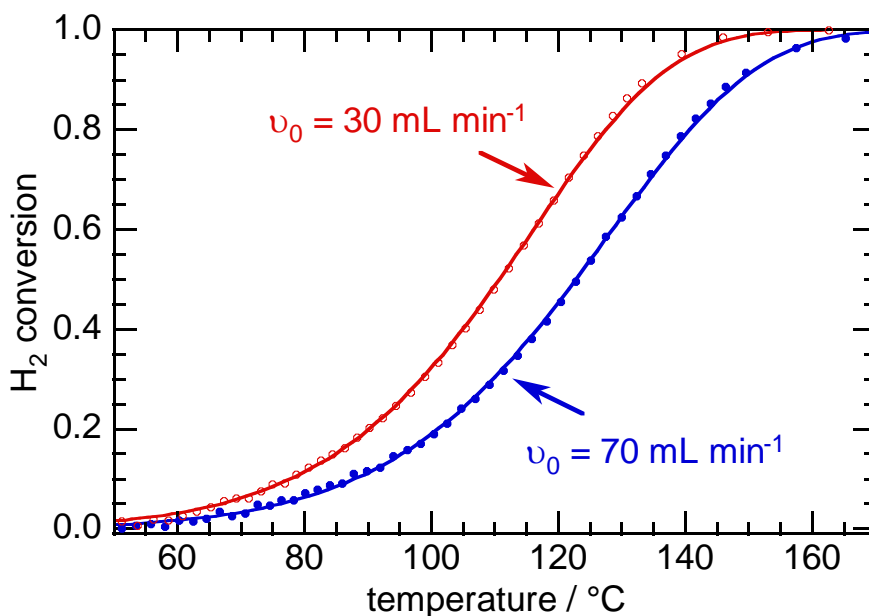


**Fig. 3.2.** Individual curve-fits for H<sub>2</sub> oxidation.

Representative reaction profiles for H<sub>2</sub> oxidation (1000 ppm H<sub>2</sub>, 100 000 ppm O<sub>2</sub>, balance Ar) over Pd/Al<sub>2</sub>O<sub>3</sub> (11.4 mg) diluted in SiC (34.5 mg), recorded at flow rates of 30 (open red circles, GHSV =  $3.8 \times 10^4$  h<sup>-1</sup>) and 70 mL min<sup>-1</sup> (solid blue circles, GHSV =  $8.9 \times 10^4$  h<sup>-1</sup>). Only one reaction profile (of three recorded) is shown for each flow rate, and every 20<sup>th</sup> datapoint is displayed (the full set of profiles is shown in Fig 3.5). Lines are individual curve-fits of Eq. 3.3 to the full data range ( $46 \leq T \leq 195$  °C) for a single reaction profile.

The orders of reaction with respect to  $\text{H}_2$  and  $\text{O}_2$  are known to be 1 and 0, respectively [1]. Since  $\Theta_{\text{O}_2} = 100$ , the sigmoidal shape of the reaction profile is determined principally by the positive reaction order with respect to the limiting reactant,  $\text{H}_2$ . As shown above (Fig. 3.2), the inlet concentration should not affect the position of the reaction profile for a first-order reaction. Indeed, profiles recorded at different inlet  $\text{H}_2$  concentrations ( $C_{\text{H}_2,0} = 500$  or  $1000$  ppm) have an identical  $T_{50}$  values and are virtually superposable (Fig. A3.9).

For each value of  $v_0$ , Eq. 3.3 was first curve-fit to a single reaction profile over the entire  $X$ - $T$  range. Two of the curve-fits are shown superposed on the experimental data in Fig. 3.2. The excellent agreement between the model and the data is readily assessed visually. It confirms that heat and mass transfer effects do not influence the rate over the entire range of conversion. The average values of  $E_a$  and  $A$  from the individual curve-fits are  $(66 \pm 2) \text{ kJ mol}^{-1}$  and  $(5 \pm 1) \times 10^4 \text{ m}^3 \text{ g}_{\text{cat}}^{-1} \text{ s}^{-1}$ , respectively. This  $E_a$  is similar to a value reported for the oxidation of  $1000 \text{ ppm H}_2$  in air, catalyzed by oxide-supported Pd nanoparticles,  $53 \text{ kJ mol}^{-1}$  [9]. It also agrees with values determined here in a differential reactor (Table 3.1), while the value for  $A$  differs by a factor of 3.

The amount of data collected in a single, variable-temperature reaction profile is clearly more than sufficient to obtain reliable kinetic parameters. Averaging curve-fit parameters from multiple individual fits did not alter the values significantly. Indeed, essentially the same values were obtained when just 1% of the data from a single reaction profile (for a total of ten data points, evenly spaced in  $X$ ) was used in the curve-fit. The effect of truncating the reaction profile was also explored. For the profile recorded at  $v_0 = 40 \text{ mL min}^{-1}$ , a curve-fit of Eq. 3.3 using data limited to  $X \leq 0.2$  yielded the same  $E_a$  value,  $(66 \pm 3) \text{ kJ mol}^{-1}$ , as did curve-fits to data truncated at other, intermediate conversions.

It is not uncommon for spurious correlations between  $E_a$  and  $A$  to appear in kinetic analyses, because of their very different magnitudes and non-linear relationship [10]. The correlation can be minimized by temperature-centering, in which a reference rate constant,  $k_0$ , is defined at a temperature  $T_0$  relevant to the reaction conditions, Eq. 3.6 [11, 12]. While Eq. 3.6 is mathematically equivalent to the usual Arrhenius relationship for  $k$ , it has the potential benefits of reducing the search space for the pre-exponential factor, as well as minimizing correlations between  $A$  and  $E_a$ .

$$k = k_0 \exp \left[ -\frac{E_a}{R} \left( \frac{1}{T} - \frac{1}{T_0} \right) \right] = A \exp \left( -\frac{E_a}{RT_0} \right) \exp \left[ -\frac{E_a}{R} \left( \frac{1}{T} - \frac{1}{T_0} \right) \right] \quad (3.6)$$

When this formulation for the rate constant was used to modify Eq. 3.3, and  $k_0$  and  $E_a$  were refined in a curve-fit to the data in Fig. 3.2, the resulting kinetic parameters were indistinguishable from those obtained using Eq. 3.3 directly, suggesting that the non-linear analysis method does not generate inherently correlated activation parameters.

The reaction orders were also studied as variable curve-fit parameters using Eq. 3.4. The results are shown in Fig. A3.10. The corresponding average values of  $E_a$  and  $A$  are essentially unchanged, at  $(61 \pm 2)$  kJ mol<sup>-1</sup> and  $(9.1 \pm 0.3) \times 10^3$  m<sup>3</sup> g<sub>cat</sub><sup>-1</sup> s<sup>-1</sup>, respectively. The average fitted reaction orders with respect to H<sub>2</sub> and O<sub>2</sub> are  $(0.9 \pm 0.1)$  and  $(-0.2 \pm 0.5)$ , respectively. Similar fit parameters were obtained at each flow rate.

### 3.3.2. Curve-fitting of individual reaction profiles for propane oxidation

Reaction profiles for propane oxidation catalyzed by Pd/Al<sub>2</sub>O<sub>3</sub> were recorded in a similar fashion, with a large excess of O<sub>2</sub> ( $C_{C_3H_8,0} = 1000$  ppm;  $C_{O_2,0} = 100\,000$  ppm). According to Fig. 3.3, their sigmoidal shape signals that the rate law has a positive reaction

order for the limiting reactant, propane. As expected, the reaction profile shifts to higher temperatures with increasing volumetric flow rate. Compared to profiles for  $\text{H}_2$  oxidation, the  $T_{50}$  values for propane oxidation are far higher (at the same concentrations and flow rate), consistent with an activation energy for propane oxidation that is approximately twice as large.

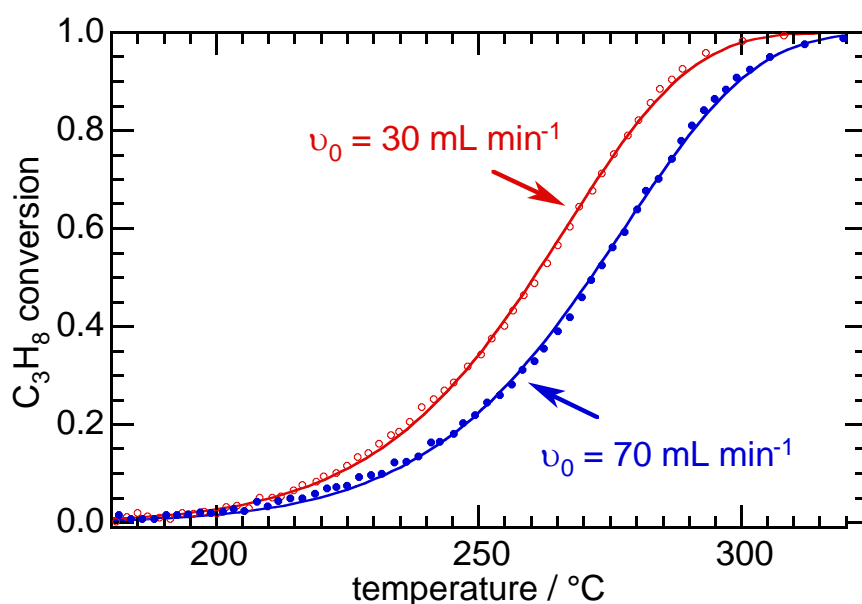


**Fig. 3.3.** Individual curve-fits for  $\text{C}_3\text{H}_8$  oxidation.

Representative reaction profiles for propane oxidation (1000 ppm  $\text{C}_3\text{H}_8$ , 100 000 ppm  $\text{O}_2$ , balance Ar) over  $\text{Pd}/\text{Al}_2\text{O}_3$  (11.8 mg) diluted in SiC (30.9 mg), recorded at flow rates of 40 (hollow red circles,  $\text{GHSV} = 5.1 \times 10^4 \text{ h}^{-1}$ ) and 60  $\text{mL min}^{-1}$  (solid blue circles,  $\text{GHSV} = 7.6 \times 10^4 \text{ h}^{-1}$ ). Only one reaction profile is shown for each flow rate (of two recorded), and every 100<sup>th</sup> datapoint is shown (the full set of profiles is shown in Fig. 3.6). Lines are individual curve-fits of Eq. 3.3 to the full data range,  $180 \leq T \leq 350 \text{ }^\circ\text{C}$ .

Curve-fits of individual reaction profiles using the entire temperature/conversion range were obtained using Eq. 3.3. The resulting average values of  $E_a$  and  $A$ ,  $(114 \pm 3) \text{ kJ mol}^{-1}$  and  $(1.0 \pm 0.3) \times 10^7 \text{ m}^3 \text{ g}_{\text{cat}}^{-1} \text{ s}^{-1}$ , respectively, agree well with the values from differential steady-state measurements in Table 3.1. The activation energy is close to the high end of the range of values reported for propane oxidation in  $\text{O}_2$ -rich conditions catalyzed by Pd foil, wire and nanoparticles supported on  $\gamma\text{-Al}_2\text{O}_3$ , typically 60-100  $\text{kJ mol}^{-1}$  [2, 13, 14]. Curve-fits obtained using Eq. 3.4 instead yielded average values for  $E_a$  and  $A$  of  $(107 \pm 4) \text{ kJ mol}^{-1}$  and  $(1.4 \pm 0.3) \times 10^6 \text{ m}^3 \text{ g}_{\text{cat}}^{-1} \text{ s}^{-1}$ , respectively, as well as reaction orders of  $(0.9 \pm 0.1)$  and  $(-0.5 \pm 0.8)$  with respect to propane and  $\text{O}_2$ , respectively.

### 3.3.3. Curve-fitting of individual reaction profiles for CO oxidation

Reaction profiles for CO oxidation with equimolar reactant concentrations ( $C_{\text{CO},0} = C_{\text{O}_2,0} = 1000 \text{ ppm}$ ) catalyzed by Pd/ $\text{Al}_2\text{O}_3$  were recorded at volumetric flow rates from 25 to 50  $\text{mL min}^{-1}$ . Under these conditions, the rate law is expected to be close to zeroth-order overall (since the orders of reaction are +1 and -1 with respect to  $\text{O}_2$  and CO, respectively). Two representative profiles are shown in Fig. 3.4. The profiles shift to higher temperatures as the volumetric flow rate increases. The rate of increase in activity accelerates with increasing temperature over nearly the entire temperature range. Such behavior is predicted qualitatively by a simulated zeroth-order reaction profile. At the lowest volumetric flow rate (25  $\text{mL min}^{-1}$ ), the rate continues to accelerate nearly to  $X = 1$ . At higher flow rates, deceleration at  $X > 0.85$  results in a sigmoidal appearance.

Prior to curve-fitting with Eq. 3.4, each reaction profile was truncated at  $X = 0.6$  to avoid possible complications from mass and/or heat transfer limitations, as well as changes in the surface chemistry, which can alter the observed rate law. In addition, the use of Eq. 3.4 is

not justified for  $X > 0.6$ , where the analytical and numerical solutions differ for  $\Theta_{\text{O}_2} \approx b/a$ . Further truncation (i.e., below  $X = 0.6$ ) did not affect the fit parameters. Representative curve-fits, with fixed reaction orders of -1 and +1 with respect to CO and O<sub>2</sub>, to the individual truncated reaction profiles are shown in Fig. 3.4. The average values for  $E_a$  and  $A$  obtained from fits at all flow rates are  $(98 \pm 3) \text{ kJ mol}^{-1}$  and  $(3 \pm 2) \times 10^6 \text{ mol g}_{\text{cat}}^{-1} \text{ s}^{-1}$ , respectively. (Fixing the reaction order with respect to O<sub>2</sub> instead at +0.5, implying dissociative chemisorption of O<sub>2</sub>, barely changes these results.) The value of  $E_a$ ,  $(96 \pm 4) \text{ kJ mol}^{-1}$ , and the refined value of  $A$ ,  $(3 \pm 2) \times 10^5 \text{ mol}^{3/2} \text{ g}_{\text{cat}}^{-1} \text{ s}^{-1} \text{ m}^{-3/2}$ , agree with those obtained by differential analysis (Table 3.1).

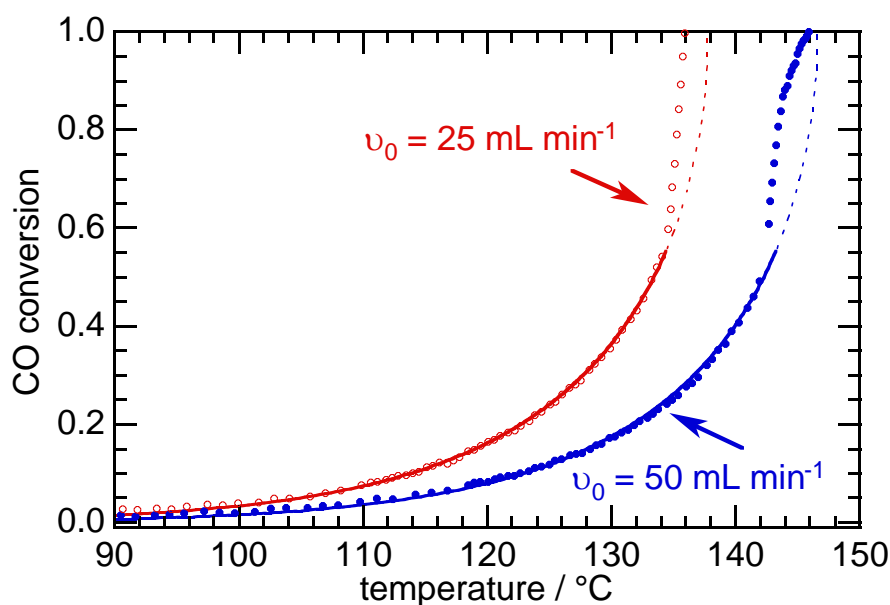


**Fig. 3.4.** Individual curve-fits for CO oxidation.

Representative reaction profiles for CO oxidation (1000 ppm CO<sub>2</sub>, 1000 ppm O<sub>2</sub>, balance Ar) over Pd/Al<sub>2</sub>O<sub>3</sub> (11.3 mg) diluted in SiC (35.4 mg), recorded at flow rates of 25 (open red circles, GHSV =  $3.2 \times 10^4 \text{ h}^{-1}$ ) and 50 mL min<sup>-1</sup> (solid blue circles, GHSV =  $6.3 \times 10^4 \text{ h}^{-1}$ ). Only one reaction profile (of three recorded) is shown for each flow rate, and approx. one-third of the data recorded is displayed (the full set of profiles is shown in Fig. 3.7). Individual curve-fits of Eq. 3.4 are shown for fixed values of  $n = -1$  and  $m = 1$ , and  $0 \leq X \leq 0.6$  (solid lines). Dashed lines show curve-fits extrapolated for  $0.6 < X \leq 1$ .



When the individual curve-fits were repeated using Eq. 3.4 and variable reaction orders  $n$  and  $m$ , the average values obtained were  $(-1.7 \pm 0.5)$  and  $(2.2 \pm 1.7)$ , respectively. While the average sum  $(n + m)$  is  $(0.5 \pm 2.2)$ , which is indistinguishable from the expected value (0), the uncertainty is very large. The opposing reaction orders in the rate law, in combination with the choice of equimolar inlet concentrations, together make it particularly difficult to distinguish  $n$  and  $m$  in the curve-fit of a single reaction profile. Therefore, global curve-fitting was explored to determine whether more reliable rate law information for complex rate laws can be obtained in this way.

### **3.4. Global curve-fitting of variable-temperature reaction profiles**

#### **3.4.1. Simultaneous analysis of H<sub>2</sub> oxidation profiles**

The global fit of Eq. 3.4 to the set of ten H<sub>2</sub> oxidation profiles (two profiles recorded consecutively at each of five different values of  $v_0$ ) is shown in Fig. 3.5. The activation energy and reaction orders were refined as global variables. The global fit reproduces the shape and position of each reaction profile. The resulting activation energy is  $(61 \pm 2)$  kJ mol<sup>-1</sup>, while the average value of  $A$  is  $(8.4 \pm 0.9) \times 10^3$  m<sup>3</sup> g<sub>cat</sub><sup>-1</sup> s<sup>-1</sup>, Table 2. The agreement with  $E_a$  values from differential, steady-state analysis, as well as with values obtained by curve-fitting individual reaction profiles (Table 3.1), is excellent.

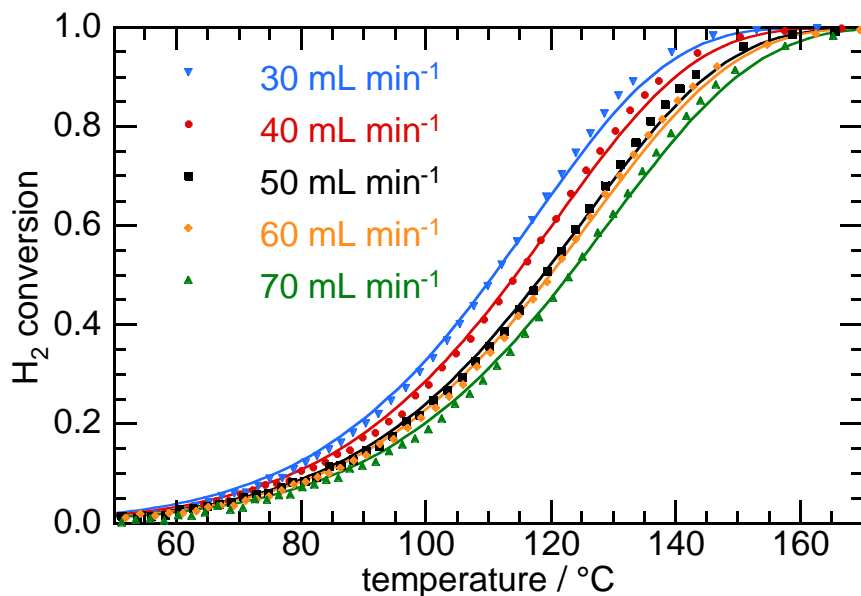


**Fig. 3.5.** Global curve-fits for H<sub>2</sub> oxidation profiles.

Reaction profiles (symbols) for H<sub>2</sub> oxidation (1000 ppm H<sub>2</sub>, 100 000 ppm O<sub>2</sub>, balance Ar) over Pd/Al<sub>2</sub>O<sub>3</sub> (11.4 mg) diluted in SiC (34.5 mg). Only one reaction profile (of three recorded) is shown for each flow rate (GHSV = 3.8 – 8.9 x 10<sup>4</sup> h<sup>-1</sup>), and every 20<sup>th</sup> datapoint is displayed. Lines are global curve-fits of Eq. 3.4 to the full data range (46 °C ≤ *T* ≤ 195 °C) for every reaction profile. *E<sub>a</sub>*, *n*, and *m* were refined as global parameters. The pre-exponential factor *A* was refined separately for each profile.

**Table 3.2.** Apparent Arrhenius parameters and reaction orders extracted from global curve-fits<sup>a</sup> of Eq. 7 to reaction profiles

Reaction	Θ <sub>b</sub>	<i>A</i>	<i>E<sub>a</sub></i> / kJ mol <sup>-1</sup>	<i>n</i>	<i>m</i>
H <sub>2</sub> + ½ O <sub>2</sub> → H <sub>2</sub> O <sup>b</sup>	100	(8.4 ± 0.9) x 10 <sup>3</sup>	61 ± 2	0.9 ± 0.1	-0.3 ± 0.4
C <sub>3</sub> H <sub>8</sub> + 5 O <sub>2</sub> → 3 CO <sub>2</sub> + 4					
H <sub>2</sub> O <sup>c</sup>	100	(2.7 ± 0.4) x 10 <sup>6</sup>	110 ± 3	0.9 ± 0.1	0.2 ± 0.3
CO + ½ O <sub>2</sub> → CO <sub>2</sub> <sup>d</sup>	1	(1.5 ± 0.4) x 10 <sup>5</sup>	91 ± 6	-1.1 ± 0.1	0.8 ± 0.2

<sup>a</sup> Ca. 11 mg Pd/Al<sub>2</sub>O<sub>3</sub> diluted 1:3 with SiC. Uncertainties in *A* are the standard deviation of the average value for duplicate runs at five different volumetric flow rates (typically, *v*<sub>0</sub> = 25 - 70 mL min<sup>-1</sup>, GHSV = 3.2 – 8.9 x 10<sup>4</sup> h<sup>-1</sup>). Uncertainties in *E<sub>a</sub>* were obtained by full error propagation using Eq. 3.5.

<sup>b</sup> C<sub>H<sub>2</sub>,0</sub> = 1000 ppm, C<sub>O<sub>2</sub>,0</sub> = 100 000 ppm. Dimensions of *A* are m<sup>3</sup> g<sub>cat</sub><sup>-1</sup> s<sup>-1</sup>.

<sup>c</sup> C<sub>C<sub>3</sub>H<sub>8</sub>,0</sub> = 1000 ppm, C<sub>O<sub>2</sub>,0</sub> = 100 000 ppm. Dimensions of *A* are m<sup>3</sup> g<sub>cat</sub><sup>-1</sup> s<sup>-1</sup>.

<sup>d</sup> C<sub>CO,0</sub> = 1000 ppm, C<sub>O<sub>2</sub>,0</sub> = 1000 ppm. Dimensions of *A* are mol<sub>CO</sub> g<sub>cat</sub><sup>-1</sup> s<sup>-1</sup>.

The globally-refined values for the reaction orders with respect to H<sub>2</sub> and O<sub>2</sub>, ( $0.9 \pm 0.1$ ) and ( $-0.3 \pm 0.4$ ), respectively, are unchanged from the values obtained in the individual curve-fits. The corresponding activation parameters are shown in Table 3.2. Fixing the reaction order with respect to O<sub>2</sub> to an integer value (i.e.,  $m = -1, 0$  or  $1$ ) did not cause the refined value of  $E_a$  to change significantly. When fixed at the reported value ( $m = 0$ ), the global fit of Eq. 3.4 gave a refined  $E_a$  value of ( $61.2 \pm 1.8$ ) kJ mol<sup>-1</sup>, an average pre-exponential factor of ( $7.0 \pm 0.8$ ) x 10<sup>3</sup> m<sup>3</sup> g<sub>cat</sub><sup>-1</sup> s<sup>-1</sup>, and a reaction order with respect to H<sub>2</sub> of ( $0.9 \pm 0.1$ ).

### 3.4.2. Simultaneous analysis of propane oxidation profiles

A similar approach was used for propane oxidation, by simultaneous curve-fitting of Eq. 3.4 to ten reaction profiles (two superposable profiles recorded at each flow rate over the entire data range, 180 – 320 °C), with  $E_a$ ,  $n$  and  $m$  as global variables (Fig. 3.6). The resulting activation energy is ( $110 \pm 3$ ) kJ mol<sup>-1</sup>, while the average value of  $A$  is ( $2.7 \pm 0.4$ ) x 10<sup>6</sup> m<sup>3</sup> g<sub>cat</sub><sup>-1</sup> s<sup>-1</sup>. The reaction order for propane refines to  $n = (0.9 \pm 0.1)$ , while the reaction order in O<sub>2</sub> refines to  $m = (0.2 \pm 0.3)$ , in agreement with the literature value (0) [2]. The values of  $E_a$  and  $n$  agree with values obtained from differential steady-state analysis and variable-temperature analysis of individual reaction profiles, while the value of  $A$  is an order of magnitude smaller. Repeating the global fit while fixing the reaction order with respect to O<sub>2</sub> at zero did not affect the values of  $E_a$ ,  $A$ , or  $n$ .

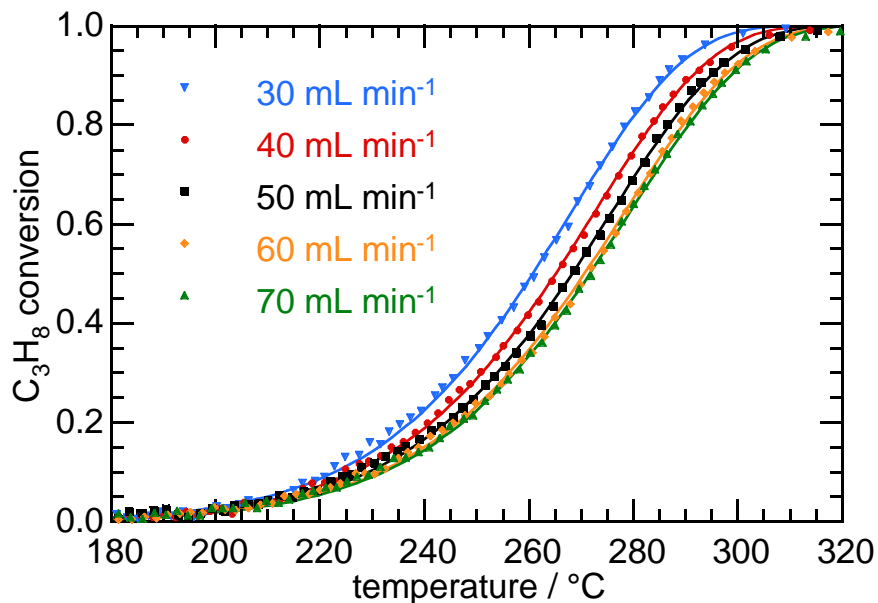


**Fig. 3.6.** Global curve-fit for  $\text{C}_3\text{H}_8$  oxidation profiles

Reaction profiles (symbols) for  $\text{C}_3\text{H}_8$  oxidation (1000 ppm  $\text{C}_3\text{H}_8$ , 100 000 ppm  $\text{O}_2$ , balance Ar) over  $\text{Pd}/\text{Al}_2\text{O}_3$  (11.8 mg) diluted in SiC (30.9 mg). Only one reaction profile (of three recorded) is shown for each flow rate ( $\text{GHSV} = 3.8 - 8.9 \times 10^4 \text{ h}^{-1}$ ), and every 100<sup>th</sup> datapoint is displayed. Lines are global curve-fits of Eq. 3.4 to the full data range ( $180 \text{ }^\circ\text{C} \leq T \leq 350 \text{ }^\circ\text{C}$ ) for every reaction profile.  $E_a$ ,  $n$ , and  $m$  were refined as global parameters. The pre-exponential factor  $A$  was refined separately for each profile.

### 3.4.3. Simultaneous analysis of CO oxidation profiles

The simultaneous fit of Eq. 3.4 to ten reaction profiles, each truncated at  $X = 0.6$ , was conducted as described above, with refinement of both reaction orders  $n$  and  $m$ . The results are shown in Fig. 3.7. The activation energy  $E_a$ ,  $(93 \pm 3) \text{ kJ mol}^{-1}$ , and the average value for the pre-exponential factor,  $(1.5 \pm 0.4) \times 10^5 \text{ mol}_{\text{CO}} \text{ g}_{\text{cat}}^{-1} \text{ s}^{-1}$ , are the same as the values in Table 1. In addition, both refined reaction orders,  $(-1.1 \pm 0.1)$  and  $(0.8 \pm 0.2)$  with respect to CO and O<sub>2</sub>, respectively, are consistent with literature values [3].

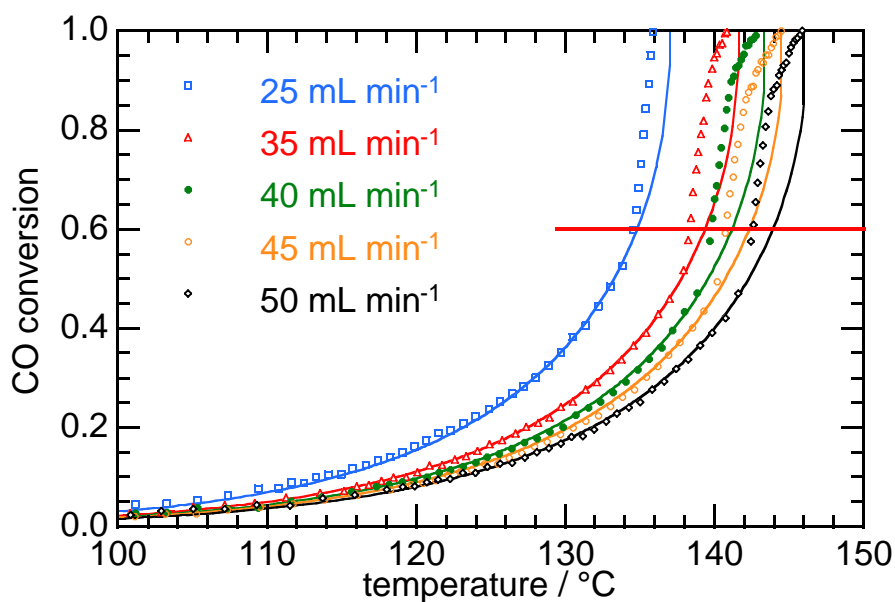


**Fig. 3.7.** Global curve-fits for CO-equimolar oxidation profiles.

Reaction profiles (symbols) for CO oxidation (1000 ppm CO, 1000 ppm O<sub>2</sub>, balance Ar) over Pd/Al<sub>2</sub>O<sub>3</sub> (11.3 mg) diluted in SiC (35.4 mg). Only one reaction profile (of three recorded) is shown for each flow rate ( $\text{GHSV} = 3.2 - 6.3 \times 10^4 \text{ h}^{-1}$ ), and approx. one-third of the data recorded is displayed. Lines are global curve-fits of Eq. 3.4 (solid lines) to data up to  $X = 0.6$  (horizontal red line).  $E_a$ ,  $n$ , and  $m$  were refined as global parameters. The pre-exponential factor  $A$  was refined separately for each profile.

### 3.5. Discussion

#### 3.5.1. Qualitative rate law information encoded in reaction profiles

The shape of the reaction profile conveys qualitative information about the reaction order with respect to the limiting reactant. Reaction orders  $n \geq 1$  give rise to sigmoidal profiles (as in the oxidations of  $\text{H}_2$  and  $\text{C}_3\text{H}_8$ ), while reaction orders  $n < 1$  give rise to profiles in which the conversion increases rapidly with temperature in a non-sigmoidal fashion (as seen for the oxidation of CO [3]). The precise reaction order can be determined either by refining the value of  $n$  in a curve-fit for which  $n$  is an adjustable parameter (Eq. 3.4), or by the agreement between the model and the data in a curve-fit using a particular integer value for  $n$  (Eq. 3.3). Where mass transfer limitations, changes in the rate law, or changes in the surface chemistry are suspected, or the choice of reactant concentrations (e.g., resulting in a significant axial gradient in  $\Theta_b$ ) requires it, the dataset can be truncated to remove affected regions (typically, at high conversion). Reactions with  $n < 1$  appear to be more susceptible to these phenomena due to the rapid rate acceleration as  $X$  approaches unity. Conversely, when the kinetic model describes the entire dataset up to  $X \approx 1$ , this is strong evidence that the rate is not influenced by mass or heat transport.

When a reactant is present in large excess over the limiting reactant (as is the case here for  $\text{O}_2$  in the oxidation of  $\text{H}_2$  and propane), its order in the rate law cannot be determined accurately from a single reaction profile. This is expected, due to the relative insensitivity of the profile to the order with respect to a concentration that is essentially constant throughout the catalyst bed under all reaction conditions used. A less common situation arises when reactants are present in similar concentrations and have opposing reaction orders (e.g., -1 and +1 for CO and  $\text{O}_2$ , respectively). Since their concentrations in

the experiment vary in parallel, and their kinetic contributions largely cancel each other, determining the reaction orders requires more than a single reaction profile.

### **3.5.2. Quantitative kinetic parameters from individual reaction profiles**

Arrhenius plots based on kinetic data collected isothermally at steady-state are routinely used to determine activation parameters for heterogeneous catalysts, but the uncertainty in the activation energy is relatively high due to the small number of data points (typically, less than 10) as well as the limited temperature range (typically,  $\leq 40$  K, as in this study). In addition, the rate law is not assessed and thus the pre-exponential factor cannot be determined without a considerable number of additional isothermal experiments. In contrast, high quality variable-temperature kinetic data can be collected quickly over a wide temperature range in less than an hour (e.g., 400 data points over 110 K for CO oxidation, and 6 000 data points over 170 K for C<sub>3</sub>H<sub>8</sub> oxidation) and its analysis provides all of the desired information, provided care is taken to ensure that mass and energy transport effects are minimized. Consecutive profiles can be used to probe catalyst stability. No special equipment or sophisticated data analysis is required, beyond a thermally-controlled packed bed reactor and a non-linear least squares fitting routine. Remarkably, identical fit results were obtained even when only 10 data points ranging from low to high conversion were analyzed.

In all three cases examined here, the activation energies obtained from a single reaction profile are indistinguishable from those measured in a series of differential steady-state experiments. Furthermore, the larger range of temperatures sampled in the variable-temperature experiment yields the activation energy with somewhat higher precision compared to the conventional Arrhenius analysis. Values for the pre-exponential factors are

close, although not identical. Since propane oxidation is much more exothermic than  $\text{H}_2$  oxidation, and has a much larger activation energy, it represents a more challenging test for reaction profile analysis. Nevertheless, the strong agreement between the differential and variable-temperature results, and between the reaction profile data and the model, confirm that the heat of reaction does not influence the measurement of the kinetic parameters.

CO oxidation is another challenging test of the general utility of variable-temperature reaction profiles. Since the rate law is inverse-first-order with respect to CO [3], the rate increases rapidly with conversion, causing non-kinetic effects to become severe. The reaction profiles in Fig. 3.4 appear to become mass transfer-limited at moderate-to-high conversions, although deviations from the extrapolated kinetic profiles could also be caused by changes in the rate law and/or the catalyst. Discontinuities may also arise from multiple steady states, which have been observed for CO oxidation over  $\text{Pt}/\text{Al}_2\text{O}_3$  [15]. When such effects distort the data, truncation may be necessary to obtain accurate kinetic parameters. For both  $\text{H}_2$  and propane oxidation, truncating the datasets did not affect the activation parameters. For CO oxidation, the extent of truncation below  $X = 0.6$  did not affect the activation parameters.

### **3.5.3. Conversion-dependent changes in kinetic parameters**

Even without a change in the rate law or the intrusion of non-kinetic effects, the ability to analyze variable-temperature reaction profiles may be impacted by large changes in activation parameters as a function of the reaction conditions. For example, the range of activation energies reported for CO oxidation catalyzed by supported Pd nanoparticles is very large (54-133  $\text{kJ mol}^{-1}$ ) [16-19]; a similarly large range has been reported for Pd single crystals (60-138  $\text{kJ mol}^{-1}$ ) [3, 16, 20]. Much of the variation is due to the dominant



contribution to the activation energy made by the CO desorption energy [16], which is strongly coverage-dependent due to lateral interactions between adsorbed CO molecules [21, 22]. For Pd(111) terraces, the initial heat of adsorption is  $149 \text{ kJ mol}^{-1}$ , while for Pd nanoparticles less than 10 nm in size, reported initial values vary from 106-126  $\text{kJ mol}^{-1}$  [23]. For Pd surfaces saturated with CO, the adsorption energy is much smaller, 60–90  $\text{kJ mol}^{-1}$  [23-25]. The heat of adsorption on Pd nanoparticles is a strong function of coverage well below 0.6 monolayers, and levels off at high coverage [23]. It also appears to be fairly independent of particle size, for particles larger than 1.5 nm [26].

Such coverage dependence could make the refinement of an “average” activation energy problematic. Fortunately, variable activation energies do not seem to be a problem here. In our experiments, the CO coverage is expected to remain high over virtually the entire  $P_{\text{CO}}$  (1000 – 400 ppm) and  $T$  (90–142 °C) ranges used in curve-fitting (corresponding to  $0.05 \leq X \leq 0.60$ ) [27]. Consequently, we do not expect the kinetic parameters to vary significantly with conversion in the analysis of individual reaction profiles. This expectation is borne out by the ability of a model containing a single activation energy to describe the profiles very well.

#### **3.5.4. Global analysis of multiple variable-temperature reaction profiles**

Uncertainties and correlations in curve-fit parameters can be minimized by performing a global (simultaneous) fit of multiple reaction profiles, recorded with varying  $\tau$  values. A similar approach has been used in kinetic analysis of TGA data (using multiple profiles recorded at different heating rates) [28]. In the cases examined here, global curve-fits gave the same activation parameters as individual curve-fits, and uncertainties in the pre-exponential factors decreased significantly. When reactant concentrations are similar, as for

CO oxidation by equimolar O<sub>2</sub>, a global fit of reaction profiles provides more reliable information about the reaction orders, in contrast to the individual fit of a single reaction profile (described above).

### **3.6. Conclusions**

Accurate information about the activation parameters and the reaction order with respect to the limiting reactant can be obtained from a single curve-fit of a variable-temperature reaction profile recorded in the absence of transport limitations. The small number of adjustable parameters (as few as two) in the fit make it likely that a unique solution will be found. The reaction order with respect to an excess reactant may be refined by simultaneous curve-fitting of multiple profiles recorded at different volumetric flow rates. When multiple reactants are present in similar concentrations, global curve-fitting makes it possible to refine their reaction orders. Obviously, additional experiments with different feed gas compositions are desirable to establish the generality of the rate law. In principle, the method could be used for rapid and rigorous assessment of the effects of metal loading, metal particle size, support interactions, promoters and poisons in the gas and solid phases, on catalyst performance. For catalysts that deactivate on a time-scale longer than the recording of a reaction profile, variable-temperature kinetic analysis could allow for fuller kinetic assessment than is currently possible with conventional steady-state methods. The variable-temperature method can detect changes in the limiting rate law as a function of reaction conditions, and in the future could be extended to include diffusion effects, more complex rate laws, reversible reactions, and variable activation energies.

## Appendix 3

### A3.1. Obtaining kinetic parameters in differential and reaction profile experiments

#### A3.1.1. Calculation of conversions

For H<sub>2</sub> oxidation over Pd/Al<sub>2</sub>O<sub>3</sub> in the presence of excess O<sub>2</sub>, the mass spectrometer signal intensity for H<sub>2</sub> at m/z = 2 ( $I_{in}$ ) was recorded at 30 °C (i.e., below the onset of activity) for each reaction profile. The signal intensity corresponding to full conversion ( $I_{zero}$ ) was recorded when no further change was observed with increasing  $T$ , Eq. A3.1:

$$\text{slope} = d/dT (\text{signal intensity at } m/z = 2) = 0 \quad (\text{A3.1})$$

At intermediate temperatures, the dimensionless conversion was calculated using Eq. A3.2, where  $I_{H2}$  represents the signal intensity at m/z = 2 recorded during the experiment.

$$X = \frac{(I_{in} - I_{zero}) - (I_{H2} - I_{zero})}{I_{in} - I_{zero}} = \frac{I_{in} - I_{H2}}{I_{in} - I_{zero}} \quad (\text{A3.2})$$

A similar procedure was followed for propane oxidation (using the ethyl cation signal at m/z = 29), except that  $I_{in}$  was recorded at a temperature below 170 °C (i.e., below the onset of activity), where  $d/dT(\text{signal intensity at } m/z = 29) = 0$ .

For CO oxidation, conversion was calculated from the calibrated intensity of the mass spectrometer signal for CO<sub>2</sub> at m/z = 44, using a standard gas mixture (1000 ppm CO<sub>2</sub> in Ar, 99.99% Praxair). After each set of experiments at a single flow rate, the mass spectrometer signal intensity was measured with the calibration gas at the same flow rate ( $I_{calibration}$ ). After 30 min, the feed was switched back to the reaction mixture and the

temperature was returned to 30 °C. When the background signal for  $m/z = 44$  was stable, its average signal intensity was recorded. This value, or the signal corresponding to 0 ppm CO<sub>2</sub>, is designated  $I_{\text{zero}}$ . Conversion was calculated using Eq. A3.3, where  $I_{\text{CO}_2}$  represents the signal intensity at  $m/z = 44$  recorded during the experiment.

$$X = \frac{I_{\text{CO}_2} - I_{\text{zero}}}{I_{\text{calibration}} - I_{\text{zero}}} \quad (\text{A3.3})$$

### A3.1.2. Calculation of rates

Under differential conditions (conversion  $< 0.1$ ) in a packed-bed reactor, the rate,  $-r_{\text{a}}$ , can be assumed constant throughout the catalyst bed. Expressed in terms of the generation of the limiting reactant **a**, the rate is given by Eq. A3.4:

$$-r_{\text{a}} = \frac{F_{\text{a},0} X}{W_{\text{cat}}} \quad (\text{A3.4})$$

where  $F_{\text{a},0}$  is the molar flow rate of the limiting reagent in mol s<sup>-1</sup>,  $X$  is the conversion, and  $W_{\text{cat}}$  is the total mass of catalyst, in g.

### A3.1.3. Writing power rate laws

The Langmuir-Hinshelwood (LH) rate law for CO oxidation, assuming molecular adsorption of O<sub>2</sub>, is written as in Eq. A3.5 [3]:

$$-r_{\text{CO}} = k_r \frac{K_{\text{CO}} K_{\text{O}_2} C_{\text{CO}} C_{\text{O}_2}}{(1 + K_{\text{CO}} C_{\text{CO}} + K_{\text{O}_2} C_{\text{O}_2})^2} \quad (\text{A3.5})$$

where  $K_{CO}$  and  $K_{O_2}$  are adsorption equilibrium constants for CO and  $O_2$ , respectively, and  $k_r$  is the rate constant for the surface reaction between adsorbed CO and O. Since  $K_{CO}C_{CO} \gg (1 + K_{O_2}C_{O_2})$  under the reaction conditions, the limiting Langmuir-Hinshelwood rate law takes a simple power law form [3]:

$$-r_{CO} = k_r \frac{K_{O_2}C_{O_2}}{K_{CO}C_{CO}} = k_{CO} \frac{C_{O_2}}{C_{CO}} \quad (A3.6)$$

where the apparent rate constant  $k_{CO}$  is defined as  $k_r K_{O_2}/K_{CO}$ . The temperature-dependence of each adsorption constant is described by Eq. A3.7:

$$K_i = \exp\left(\frac{\Delta S_i}{R}\right) \exp\left(-\frac{\Delta H_i}{RT}\right) = A_i \exp\left(-\frac{\Delta H_i}{RT}\right) \quad (A3.7)$$

Thus the Arrhenius behavior of  $k_{CO}$  includes the temperature dependence of the two adsorption constants, Eq. A3.8:

$$k_{CO} = A \exp\left(-\frac{E_a}{RT}\right) = \frac{A_r A_{O_2}}{A_{CO}} \exp\left(-\frac{E_a - \Delta H_{O_2} + \Delta H_{CO}}{RT}\right) \quad (A3.8)$$

In the oxidation of  $H_2$  [1] and propane [2], the reactions are known to obey power rate laws from which  $C_{O_2}$  is absent, when  $O_2$  is present in large excess:

$$-r_{H_2} = k_{H_2} C_{H_2} \quad (A3.9)$$

$$-r_{C_3H_8} = k_{C_3H_8} C_{C_3H_8} \quad (A3.10)$$

#### A3.1.4. Calculation of rate constants

For CO oxidation, the power rate law is first-order in O<sub>2</sub> and inverse-first-order in CO [3]. Thus the apparent rate constant  $k_{CO}$  is obtained from:

$$k_{CO} = \frac{F_{CO,0} X C_{CO,0} (1-X)}{W_{cat} C_{CO,0} (\Theta_{O_2} - X/2)} = \frac{C_{CO,0} v_0 X C_{CO,0} (1-X)}{W_{cat} C_{CO,0} (\Theta_{O_2} - X/2)} \quad (A3.11)$$

where  $C_{CO,0}$  is the inlet concentration of the limiting reagent, and  $\Theta_{O_2}$  is the molar ratio of O<sub>2</sub> and CO. Assuming ideal gas behavior, the temperature dependence of  $C_{CO,0}$  and  $v_0$  can each be written in terms of an arbitrary reference temperature  $T_{ref}$ , Eq. A3.12- A3.13 ( $R$  is the ideal gas constant).

$$C_{CO,0} = C_{CO,0,ref} \frac{T_{ref}}{T} = \frac{P_{CO,0}}{RT_{ref}} \frac{T_{ref}}{T} \quad (A3.12)$$

$$v_0 = v_{0,ref} \frac{T}{T_{ref}} \quad (A3.13)$$

Since the oxidation of H<sub>2</sub> or propane in the presence of a large excess of O<sub>2</sub> can be described by a power rate law that is zeroth-order in O<sub>2</sub> and first-order in either H<sub>2</sub> (Eq. A3.9), or C<sub>3</sub>H<sub>8</sub> (Eq. A3.10), the apparent rate constants are:

$$k_{H_2} = \frac{-r_{H_2}}{C_{H_2}} = \frac{-r_{H_2}}{C_{H_2,0}(1-X)} = \frac{F_{H_2,0} X}{W_{cat} C_{H_2,0}(1-X)} = \frac{C_{H_2,0} v_0 X}{W_{cat} C_{H_2,0}(1-X)} \quad (A3.14)$$

$$k_{C_3H_8} = \frac{-r_{C_3H_8}}{C_{C_3H_8}} = \frac{-r_{C_3H_8}}{C_{C_3H_8,0}(1-X)} = \frac{F_{C_3H_8,0}X}{W_{cat}C_{C_3H_8,0}(1-X)} = \frac{C_{C_3H_8,0}v_0X}{W_{cat}C_{C_3H_8,0}(1-X)} \quad (A3.15)$$

### A3.1.5. Sample rate constant calculation

In a propane oxidation experiment, the following parameters are typical:

Feed: 1000 ppm  $C_3H_8$ , 10%  $O_2$

$W_{catalyst} = 11.8 \text{ mg}$ ,  $v_{0,ref} = 50 \text{ mL min}^{-1}$

$T_{ref} = 298 \text{ K}$ ,  $T = 525 \text{ K}$

$S_{in} = 2.57 \times 10^{-9}$ ,  $S_{zero} = 8.29 \times 10^{-12}$ ,  $S_{C_3H_8} = 2.38 \times 10^{-9}$

Using Eq. A3.12- A3.13 to express the temperature dependence of  $C_{a,0}$  and  $v_0$  in terms of an arbitrary reference temperature  $T_{ref}$ , we obtain:

$$C_{C_3H_8,0} = \frac{P_{C_3H_8}}{RT} = \left[ \frac{(1 \times 10^{-3} \frac{\text{mol } C_3H_8}{\text{mol}}) 1 \text{ atm}}{(0.082 \frac{\text{L} \cdot \text{atm}}{\text{mol} \cdot \text{K}}) \cdot 525 \text{ K}} \right] \left( 10^3 \frac{\text{L}}{\text{m}^3} \right) = 2.3 \times 10^{-2} \frac{\text{mol } C_3H_8}{\text{m}^3} \quad (A3.16)$$

$$F_{C_3H_8,0} = C_{C_3H_8,0}v_0 = \frac{P_{C_3H_8,0}}{RT} v_{0,ref} \frac{T}{T_{ref}} = \frac{P_{C_3H_8,0}v_{0,ref}}{RT_{ref}}$$

$$0.023 \frac{\text{mol } C_3H_8}{\text{m}^3} 50 \frac{\text{mL}}{\text{min}} \left( \frac{525 \text{ K}}{298 \text{ K}} \right) \left( \frac{\text{min}}{60 \text{ s}} \right) \left( \frac{\text{m}^3}{10^6 \text{ mL}} \right) = 3.4 \times 10^{-8} \text{ mol } C_3H_8 \text{ s}^{-1} \quad (A3.17)$$

$$X = \frac{S_{in} - S_{C_3H_8,0}}{S_{in} - S_{zero}} = \frac{2.57 \times 10^{-9} - 2.38 \times 10^{-9}}{2.57 \times 10^{-9} - 8.29 \times 10^{-12}} = 0.074 \quad (A3.18)$$

$$-r_{C_3H_8} = \frac{F_{C_3H_8,0}X}{W_{cat}} = \frac{(3.4 \times 10^{-8} \text{ mol } C_3H_8 \text{ s}^{-1})(0.074)}{0.0118 \text{ g}_{catalyst}} = 2.1 \times 10^{-7} \frac{\text{mol } C_3H_8}{\text{g}_{catalyst} \cdot \text{s}} \quad (A3.19)$$

$$k_{C_3H_8} = \frac{2.1 \times 10^{-7} \frac{\text{mol } C_3H_8}{\text{g}_{\text{catalyst}} \cdot \text{s}}}{\left(0.023 \frac{\text{mol } C_3H_8}{\text{m}^3}\right)(1-0.074)} = 5.7 \times 10^{-6} \frac{\text{m}^3}{\text{g}_{\text{catalyst}} \cdot \text{s}} \quad (\text{A3.20})$$

The unusual units for the pseudo-first-order rate constant  $k_{C_3H_8}$  arise because the reactant and catalyst exist in different phases.

### A3.2. Minimizing non-kinetic effects in reaction profiles

#### A3.2.1. Prediction of external and interparticle diffusion limitations

The potential contribution of external and interparticle diffusion rates to the observed reaction rate was assessed using Mears' Criterion [4]. For spherical catalyst particles of radius  $R_P$  and a reaction that can be described by a power rate law of order  $n$  in the limiting reagent **a**, external diffusion does not contribute significantly to the rate if:

$$\frac{-r_a R_P n}{k_c C_{a,\text{bulk}}} < 0.15 \quad (\text{A3.21})$$

where  $k_c$  is the mass transfer coefficient of **a** and  $C_{a,\text{bulk}}$  is the gas-phase concentration of **a** in the reactor.

##### A3.2.1.1. Sample calculation of Mears' Criterion

Oxidation of  $H_2$  (1000 ppm,  $n = 1$ ) was conducted in the presence of a large excess of  $O_2$  (100,000 ppm,  $m = 0$ ) over a  $Pd/Al_2O_3$  catalyst with average particle diameter  $2R_P = 165 \mu\text{m}$ . The reaction rate is proportional to  $C_{H_2,\text{bulk}}$  and the volumetric flow rate  $v_0$ , for



which  $50 \text{ mL min}^{-1}$  (at 298 K, or  $71 \text{ mL min}^{-1}$  at 423 K assuming ideal gas behavior) is typical. The following calculation was performed at 423 K, for which  $X = 0.95$ . At 125 °C, the bulk concentration of  $\text{H}_2$  (also assuming ideal gas behavior) is taken to be the average  $\text{H}_2$  concentration in the reactor, i.e.,  $C_{\text{H}_2, \text{bulk}} = C_{\text{H}_2} = C_{\text{H}_2, 0}(1-X)$ . The inlet concentration is:

$$C_{\text{H}_2, 0} = \left(1 \times 10^{-3} \frac{\text{mol H}_2}{\text{mol}}\right) \left[ \frac{1 \text{ atm}}{\left(0.082 \frac{\text{L} \cdot \text{atm}}{\text{mol} \cdot \text{K}}\right) \cdot 423 \text{ K}} \right] \left(10^3 \frac{\text{L}}{\text{m}^3}\right) = 2.9 \times 10^{-2} \frac{\text{mol H}_2}{\text{m}^3} \quad (\text{A3.22})$$

At 95 %  $\text{H}_2$  conversion, the average rate normalized by catalyst volume  $V_{\text{cat}}$  (based on a cylindrical bed of diameter  $d = 3.9 \text{ mm}$  and height  $h = 4 \text{ mm}$ ) is:

$$V_{\text{cat}} = \pi(h) \left(\frac{d}{2}\right)^2 = \pi(0.004 \text{ m}) \left(\frac{0.0039 \text{ m}}{2}\right)^2 = 4.7 \times 10^{-8} \text{ m}^3 \quad (\text{A3.23})$$

$$-r_{\text{H}_2} = \frac{C_{\text{H}_2, 0} v_0 X}{V_{\text{cat}}} = \frac{\left(2.9 \times 10^{-2} \frac{\text{mol H}_2}{\text{m}^3}\right) \left(0.071 \frac{\text{L}}{\text{min}}\right) \left(\frac{\text{m}^3}{10^3 \text{ L}}\right) \left(\frac{\text{min}}{60 \text{ s}}\right) (0.95)}{4.7 \times 10^{-8} \text{ m}^3} = 0.68 \frac{\text{mol H}_2}{\text{m}^3 \cdot \text{s}} \quad (\text{A3.24})$$

The mass transfer coefficient  $k_c$  is estimated from the dimensionless Sherwood number  $Sh$ :

$$k_c = \frac{Sh \cdot D_{12}}{2R_p} \quad (\text{A3.25})$$

where the diffusivity,  $D_{12}$ , for equimolar  $H_2$  in Ar at 423 K is  $1.51 \times 10^{-4} \text{ m}^2 \text{ s}^{-1}$  [29].

The value of  $Sh$  [30] is given by:

$$Sh = 2 + 0.6Re^{0.5}Sc^{0.33} \quad (\text{A3.26})$$

where  $Re$  and  $Sc$  are the dimensionless Reynolds and Schmidt numbers, respectively:

$$Sc = \frac{\mu}{\rho D_{12}} \quad (\text{A3.27})$$

$$Re = \frac{u\rho(2R_p)}{\mu} \quad (\text{A3.28})$$

The viscosity  $\mu$  of the diluent Ar at 423 K is  $2.98 \times 10^{-5} \text{ Pa}\cdot\text{s}$  [31], while its fluid density  $\rho$  is:

$$\rho = \frac{m}{V} = \frac{PM_{Ar}}{RT} = \frac{\left(39.9 \frac{\text{g}}{\text{mol}}\right)(1 \text{ atm})}{\left(0.082 \frac{\text{L}\cdot\text{atm}}{\text{mol}\cdot\text{K}}\right)(423\text{K})} \left(10^3 \frac{\text{L}}{\text{m}^3}\right) = 1.15 \times 10^3 \frac{\text{g}}{\text{m}^3} = 1.2 \frac{\text{kg}}{\text{m}^3} \quad (\text{A3.29})$$

where  $m$  is the mass of Ar,  $M_{Ar}$  is the molar mass of Ar, and  $V$  is the gas volume, calculated assuming ideal gas behavior. The linear fluid velocity,  $u$ , depends on the volumetric flow rate  $v_0$  and the reactor cross-sectional area  $A_c$ :

$$A_c = \pi \left(\frac{d}{2}\right)^2 = \pi \left(\frac{0.0039 \text{ m}}{2}\right)^2 = 1.2 \times 10^{-5} \text{ m}^2 \quad (\text{A3.30})$$

$$v_0 = v_{0,\text{ref}} \frac{T}{T_{\text{ref}}} = \left(0.050 \frac{\text{L}}{\text{min}}\right) \left(\frac{423 \text{ K}}{298 \text{ K}}\right) \left(\frac{\text{m}^3}{10^3 \text{ L}}\right) \left(\frac{\text{min}}{60 \text{ s}}\right) = 1.2 \times 10^{-6} \frac{\text{m}}{\text{s}} \quad (\text{A3.31})$$

$$u = \frac{v_0}{A_c} = \frac{1.2 \times 10^{-6} \frac{\text{m}}{\text{s}}}{1.2 \times 10^{-5} \text{ m}^2} = 0.10 \frac{\text{m}}{\text{s}} \quad (\text{A3.32})$$

Thus, the estimated values of the dimensionless numbers are:

$$Sc = \frac{\mu}{\rho D_{12}} = \frac{2.98 \times 10^{-5} \text{ Pa}\cdot\text{s}}{\left(1.2 \frac{\text{kg}}{\text{m}^3}\right) \left(1.51 \times 10^{-4} \frac{\text{m}^2}{\text{s}}\right)} = 0.17 \quad (\text{A3.33})$$

$$Re = \frac{u \rho (2R_p)}{\mu} = \frac{\left(0.10 \frac{\text{m}}{\text{s}}\right) \left(1.2 \frac{\text{kg}}{\text{m}^3}\right) (1.65 \times 10^{-4} \text{ m})}{2.98 \times 10^{-5} \text{ Pa}\cdot\text{s}} = 0.64 \quad (\text{A3.34})$$

$$Sh = 2 + 0.6 Re^{0.5} Sc^{0.33} = 2 + 0.6 (0.64)^{0.5} (0.21)^{0.33} = 2.27 \quad (\text{A3.35})$$

Together, they lead to the following estimate for the mass transfer coefficient for H<sub>2</sub> in Ar, and Mears' Criterion:

$$k_c = \frac{Sh \cdot D_{12}}{2R_p} = \frac{(2.27) \left(1.51 \times 10^{-4} \frac{\text{m}^2}{\text{s}}\right)}{1.65 \times 10^{-4} \text{ m}} = 2.1 \frac{\text{m}}{\text{s}} \quad (\text{A3.36})$$

$$\frac{-r_a R_p n}{k_c C_{a,\text{bulk}}} = \frac{\left(0.68 \frac{\text{mol H}_2}{\text{m}^3 \cdot \text{s}}\right) (8.3 \times 10^{-5} \text{ m})}{\left(2.1 \frac{\text{m}}{\text{s}}\right) \left(2.9 \times 10^{-2} \frac{\text{mol H}_2}{\text{m}^3}\right) (1-0.95)} = 0.019 \quad (\text{A3.37})$$

Since the estimated value of Mears' Criterion for H<sub>2</sub> oxidation, 0.019, is an order of magnitude smaller than the value (0.15) which would signal the onset of external diffusion limitations for a first-order reaction, external mass transport should not be rate-limiting for values of X up to at least 0.95. Since this calculation was performed for a condition near the

highest observed rate in this study, all other reaction conditions are expected to be unaffected by external diffusion as well.

The Mears' Criterion for propane oxidation, also calculated for  $X = 0.95$ , is 0.07, suggesting the absence of external mass transfer limitations for almost all reaction conditions used in this study. Further empirical tests were conducted to confirm that external mass transport is not rate limiting (see section A3.2.4.1). For CO oxidation, under the reaction conditions used in this study, the rate law is net pseudo-zeroth-order. Mears [4] and Eq. A3.21 suggest that zeroth-order reactions cannot be external mass transport-limited. However evidence for external mass transport limitation is evident at high conversion,  $X > 0.85$  (Fig. 3.4), therefore reaction profiles were truncated below  $X = 0.6$  before kinetic analysis was performed.

### A3.2.2. Prediction of intraparticle diffusion limitations

Potential internal mass transfer limitations were assessed via the Weisz-Prater Criterion,  $C_{wp}$  [5]. When  $C_{wp} < 1$ , internal diffusion is not rate-determining. For spherical catalyst particles of radius  $R_p$ ,  $C_{wp}$  is given by:

$$C_{wp} = \frac{-r_a R_p^2}{D_{TA}^e C_{a,s}} \quad (A3.38)$$

where  $D_{TA}^e$  is the effective diffusivity of the gas mixture, defined in terms of the molecular diffusivity  $D_{12}$  and the Knudsen diffusivity  $D_{K1}$  in Eq. A3.39.  $C_{a,s}$  is the concentration of the limiting reagent at the particle surface.

$$(D_{TA}^e)^{-1} = (D_{12})^{-1} + (D_{K1})^{-1} \quad (\text{A3.39})$$

### A3.2.2.1. Sample calculation of Weisz-Prater Criterion

The value of  $D_{K1}$  for  $H_2$  in Sasol HTA-102 non-ordered mesoporous  $\gamma$ -alumina ( $12 < R_{\text{pore}} < 17$  nm, with a midpoint value of  $15 \text{ nm} = 1.5 \times 10^{-8} \text{ m}$ ) at 423 K is:

$$D_{K1} = \frac{2R_{\text{pore,median}}}{3} \sqrt{\frac{8RT}{\pi M_{H_2} (\text{kg}/10^3 \text{g})}} = \frac{2(1.5 \times 10^{-8} \text{m})}{3} \sqrt{\frac{8(8.314 \frac{\text{J}}{\text{mol K}})423 \text{ K}}{\pi (2 \frac{\text{g}}{\text{mol}})(\frac{\text{kg}}{10^3 \text{g}})}} = 2.1 \times 10^{-5} \frac{\text{m}^2}{\text{s}} \quad (\text{A3.40})$$

For equimolar  $H_2$  in Ar at 423 K, the value of  $D_{12}$  is  $1.51 \times 10^{-4} \text{ m}^2 \text{ s}^{-1}$  [29]. The value of  $D_{TA}^e$  is therefore estimated as:

$$D_{TA}^e = \{(D_{12})^{-1} + (D_{K1})^{-1}\}^{-1} = \{(1.5 \times 10^{-4})^{-1} + (2.1 \times 10^{-5})^{-1}\}^{-1} \frac{\text{m}^2}{\text{s}} = 1.9 \times 10^{-5} \frac{\text{m}^2}{\text{s}} \quad (\text{A3.41})$$

Since the reaction rate is not limited by external diffusion (see section A3.2.1 above),  $C_{a,s}$  can be estimated as  $C_{H_2, \text{bulk}} = C_{H_2,0}(1-X)$ . The value of the Weisz-Prater Criterion is therefore:

$$\frac{-r_a(R_P)^2}{D_{TA}^e C_{a,s}} = \frac{(0.68 \frac{\text{mol } H_2}{\text{m}^3 \cdot \text{s}})(8.2 \times 10^{-5} \text{m})^2}{(1.9 \times 10^{-5} \frac{\text{m}^2}{\text{s}})(2.9 \times 10^{-2} \frac{\text{mol } H_2}{\text{m}^3})(1-X)} = 0.17 \quad (\text{A3.42})$$

Since the value of the Weisz-Prater Criterion is less than 1, we infer that the reaction rate is probably not limited by internal diffusion. When the calculation is repeated with a lower pore radius of 12 nm, the resulting  $C_{wp}$  is 0.21, which is still less than 1. Since this calculation was performed for a condition near the highest observed rate in this study, all other reaction conditions are expected to be unaffected by internal diffusion as well.

For propane oxidation, the Weisz-Prater Criterion calculated in the same way, at the concentration  $C_{a,s}$  corresponding to  $X = 0.95$  for the median pore size (15 nm), is 0.9, and when the calculation is repeated for the smallest pore size of 12 nm, the value of  $C_{wp}$  is 1.1. Therefore the reaction rate for propane oxidation is potentially susceptible to internal diffusion limitations, and we performed further tests (see section A3.2.4.2) to confirm that internal diffusion is not rate-limiting in propane oxidation.

For CO oxidation at  $X = 0.6$ , the Weisz-Prater parameter is 0.053, indicating that this reaction is kinetically controlled over the entire range of conditions used for kinetic analysis.

### **A3.2.3. Prediction of heat transfer effects on reaction rates**

The potential contribution of external heat transfer effects to the reaction rates was explored using Mears' heat criterion [6].

$$\frac{\Delta H_{rxn}(-r_a)R_p E_a}{hT^2 R} < 0.15 \quad (A3.43)$$

where  $\Delta H_{rxn}$  is the heat of reaction,  $h$  is the heat transfer coefficient, and  $R$  is the gas constant.

### A3.2.3.1. Sample calculation of Mears' heat Criterion

Propane oxidation is the most exothermic of the three reactions studied here, and therefore the most likely rate to be impacted by heat transfer limitations. This possibility was assessed at 573 K, where  $X = 0.95$ . The heat transfer coefficient,  $h$ , can be estimated from the Nusselt number,  $Nu$  [30]:

$$Nu = \frac{h(2R_p)}{k_T} = 2 + 0.6Re^{0.5}Pr^{1/3} \quad (A3.44)$$

The thermal diffusivity,  $\alpha$ , for Ar is used to calculate the Prandtl number,  $Pr$ . The thermal conductivity for Ar,  $k_T$ , is  $0.027 \text{ W m}^{-1} \text{ K}^{-1}$  at 573 K [32]; its density,  $\rho$ , is  $0.85 \text{ kg/m}^3$  (Eq. A3.29 calculated at 573 K); and its heat capacity,  $C_p$ , is  $570 \text{ J kg}^{-1} \text{ K}^{-1}$  [33].

$$\alpha = \frac{k_T}{\rho C_p} = \frac{0.027 \frac{\text{W}}{\text{m} \cdot \text{K}}}{\left(0.85 \frac{\text{kg}}{\text{m}^3}\right) \left(570 \frac{\text{J}}{\text{kg} \cdot \text{K}}\right)} = 5.5 \times 10^{-5} \frac{\text{m}^2}{\text{s}} \quad (A3.45)$$

$$Pr = \frac{\mu}{\rho \alpha} = \frac{(3.8 \times 10^{-5} \text{ Pa} \cdot \text{s})}{\left(0.85 \frac{\text{kg}}{\text{m}^3}\right) \left(5.5 \times 10^{-5} \frac{\text{m}^2}{\text{s}}\right)} = 0.81 \quad (A3.46)$$

The heat transfer coefficient,  $h$ , is obtained by rearranging Eq. A3.44:

$$h = \left(2 + 0.6Re^{0.5}Pr^{\frac{1}{3}}\right) \frac{k_T}{2R_p} = \left(2 + 0.6(0.5)^{0.5}(0.81)^{\frac{1}{3}}\right) \frac{0.027 \frac{\text{W}}{\text{m} \cdot \text{K}}}{1.65 \times 10^{-4} \text{ m}} = 389 \frac{\text{W}}{\text{m}^2 \cdot \text{K}} \quad (A3.47)$$

The activation energy for propane oxidation is  $E_a = 111 \text{ kJ mol}^{-1}$  (from the main text), and the heat of reaction is  $\Delta H^\circ = -2219 \text{ kJ mol}^{-1}$  [34]. Mears' heat criterion is therefore:

$$\frac{(2,219,000 \frac{\text{J}}{\text{mol}})(0.68 \frac{\text{mol}}{\text{m}^3 \cdot \text{s}})(8.3 \times 10^{-5} \text{ m})(111,000 \frac{\text{J}}{\text{mol}})}{(389 \frac{\text{W}}{\text{m}^2 \cdot \text{K}})(573 \text{ K})^2(8.314 \frac{\text{J}}{\text{mol} \cdot \text{K}})} = 0.013 \quad (\text{A3.48})$$

For propane oxidation at 95% conversion, the Mears' heat criterion is an order of magnitude less than 0.15, thus external heat transfer probably does not affect the rate of reaction under the reaction conditions. To confirm this conclusion, further experimental tests were performed (see section A3.2.4.3).

Both CO oxidation ( $\Delta H^\circ = -283 \text{ kJ mol}^{-1}$ ) [35] and  $\text{H}_2$  oxidation ( $\Delta H^\circ = -284 \text{ kJ mol}^{-1}$ ) [35] are much less exothermic than propane oxidation. The Mears' heat criteria for CO oxidation at 423 K ( $X = 0.6$ ) and  $\text{H}_2$  oxidation at 423 K ( $X = 0.95$ ) are  $1.6 \times 10^{-3}$  and  $1.7 \times 10^{-3}$ , respectively (reaction profiles for CO oxidation were only analyzed up to  $X = 0.6$ , see Fig. 3.4). Therefore external heat transfer does not affect the rates of these reactions under the conditions used in this study.

#### **A3.2.4. Experimental assessment of heat and mass transfer limitations**

Use of a small reactor radius (3.8 mm i.d.), dilution of the catalyst bed with an inert material (1:3 SiC) and dilution of the feed with an inert gas (1000 ppm max, limiting reactant gas concentration in Ar) are all methods to reduce heat transfer effects in packed bed reactors [6]. The absence of significant axial temperature gradients was verified experimentally for CO oxidation ( $C_{\text{CO},0} = C_{\text{O}_2,0} = 1000 \text{ ppm}$ ) by monitoring the temperature



of the catalyst bed with two K-type thermocouples, placed at the entrance and the end of the bed. The axial temperature gradient did not exceed 1 K at any inlet temperature, even for  $X = 1$ .

#### A3.2.4.1. Experimental assessment of external mass transport and heat transfer effects

The absence of external mass transport limitations and external heating effects on the reaction rate in a reactor can be validated experimentally by simultaneously varying the catalyst loading and volumetric flow rate in order to maintain a constant space-time  $\tau$ . If there is no effect on the conversion, then the reaction is kinetically controlled [4].

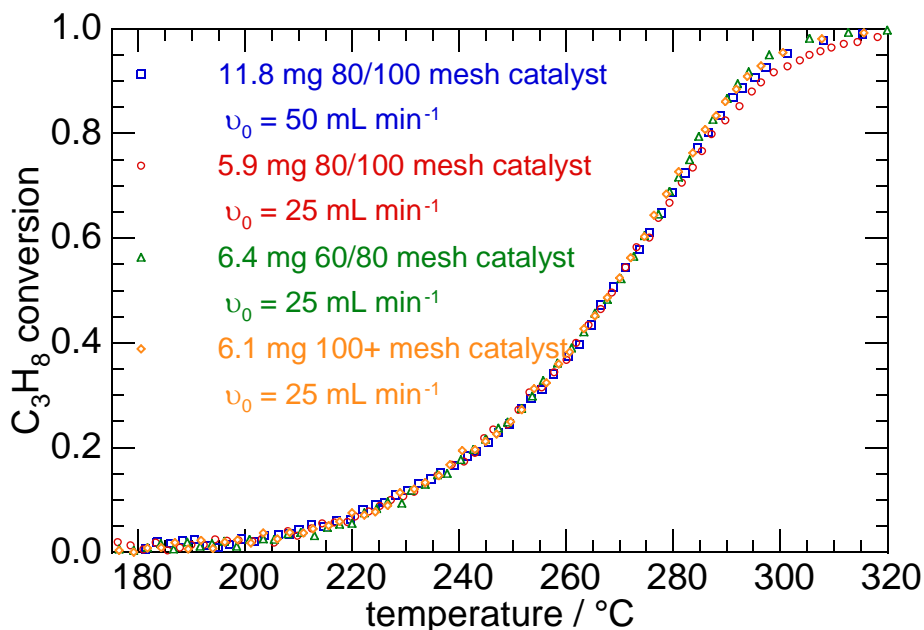


**Fig. A3.1.** Comparison of reaction profiles recorded for  $C_3H_8$  oxidation ( $C_{C_3H_8,0} = 1000$  ppm,  $C_{O_2,0} = 100,000$  ppm, balance Ar) over 2 wt% Pd/Al<sub>2</sub>O<sub>3</sub> sieved to 80/100 mesh (11.8 mg diluted in 30.9 mg SiC, open blue squares; 5.9 mg diluted in 15.5 mg SiC, open red circles), so that the ratio of catalyst weight to volumetric flow rate is constant ( $\tau = 11.8 \text{ mg} / 50 \text{ mL min}^{-1} = 5.9 \text{ mg} / 25 \text{ mL min}^{-1} = 0.24 \text{ mg catalyst} / \text{mL min}^{-1}$ ). Also shown is the effect of particle size: 6.4 mg catalyst sieved to 60/80 mesh and diluted 3:1 w/w in SiC (open green triangles), and 6.1 mg catalyst sieved to 100+ mesh and diluted 3:1 w/w in SiC (open orange diamonds). Prior to recording each reaction profile, the catalyst was pre-conditioned at 500 °C ( $X = 1$ ) for 3 h under reaction conditions. Showing every 100<sup>th</sup> data point.

Since total propane oxidation has the highest heat of reaction for the three reactions tested in this study ( $\Delta H^\circ = -2219 \text{ kJ mol}^{-1}$  [34]), reaction profiles were recorded for propane oxidation ( $C_{\text{C}_3\text{H}_8,0} = 1000 \text{ ppm}$ ,  $C_{\text{O}_2,0} = 100,000 \text{ ppm}$ , balance Ar) over 2 wt% Pd/Al<sub>2</sub>O<sub>3</sub> with different amounts of catalyst. One reaction profile was recorded with 11.8 mg catalyst diluted in 30.9 mg SiC, at a flow rate of 50 mL min<sup>-1</sup>. Another reaction profile was recorded with 5.9 mg catalyst diluted in 15.5 mg SiC, at flow rate of 25 mL min<sup>-1</sup>, in order to maintain the same value of  $\tau$ . The resulting reaction profiles are nearly superposable, Fig. A3.1 (compare red and blue data). Since the values of  $X$  corresponding to each  $T$  are the same, the reaction is kinetically controlled. The much smaller heats of reaction for oxidation of H<sub>2</sub> ( $\Delta H^\circ = -284 \text{ kJ mol}^{-1}$ ) [35] and CO ( $\Delta H^\circ = -283 \text{ kJ mol}^{-1}$ ) [35] will produce smaller temperature gradients, therefore we assume that these reactions are also kinetically controlled.

#### **A3.2.4.2. Experimental assessment of internal mass transport limitations**

Internal diffusion limitations can be assessed experimentally by examining the effect on conversion of the catalyst particle size [4]. Reaction profiles were recorded over 2 wt% Pd/Al<sub>2</sub>O<sub>3</sub> sieved to three different particle sizes: 60/80 mesh ( $0.18 \text{ mm} < 2R_p < 0.25 \text{ mm}$ ), 80/100 mesh ( $0.15 \text{ mm} < 2R_p < 0.18 \text{ mm}$ ), and 100+ mesh ( $2R_p < 0.15 \text{ mm}$ ). In each case, ca. 6 mg catalyst was diluted 3:1 w/w in SiC, and the flow rate was held constant at 25 mL min<sup>-1</sup>. All of the reaction profiles are superposable, Fig. A3.1. Therefore the conversion does not vary with particle size, and we conclude that internal diffusion is not rate-limiting in propane oxidation.

Since the Weisz-Prater criterion for propane oxidation is larger than values calculated for either  $\text{H}_2$  or CO oxidation, we can assume that all of the reactions are kinetically controlled. All subsequent reaction profiles were recorded using catalyst sieved to 80/100 mesh.

#### **A3.2.4.3. Experimental assessment of heat transfer limitations**

The possible formation of hot spots (from the heat of reaction) in the catalyst bed, due to slow heat transfer in exothermic reactions, can be explored experimentally by varying the amount of inert diluent present in the catalyst bed. Reaction profiles for propane oxidation were recorded at catalyst dilution ratios of 2:1, 3:1, and 4:1, Fig. A3.2. The three reaction profiles are almost superposable. We infer that slow heat transfer is not a significant issue in the catalyst bed under our reaction conditions. Since  $\text{H}_2$  and CO oxidation are both considerably less exothermic, it is unlikely that slow heat transfer is a significant issue in those reactions either.

The influence of the temperature ramp rate was studied for  $\text{H}_2$  oxidation. Reaction profiles recorded at ramp rates of 2, 5, 7, and  $10\text{ }^\circ\text{C min}^{-1}$  are shown in Fig. A3.3. The near-superposability of the profiles suggests that heat transfer effects are not important in our reactor configuration for temperature ramp rates between 2 and  $7\text{ }^\circ\text{C min}^{-1}$ . Therefore all reaction profiles were recorded with ramp rates of  $5\text{ }^\circ\text{C min}^{-1}$ .

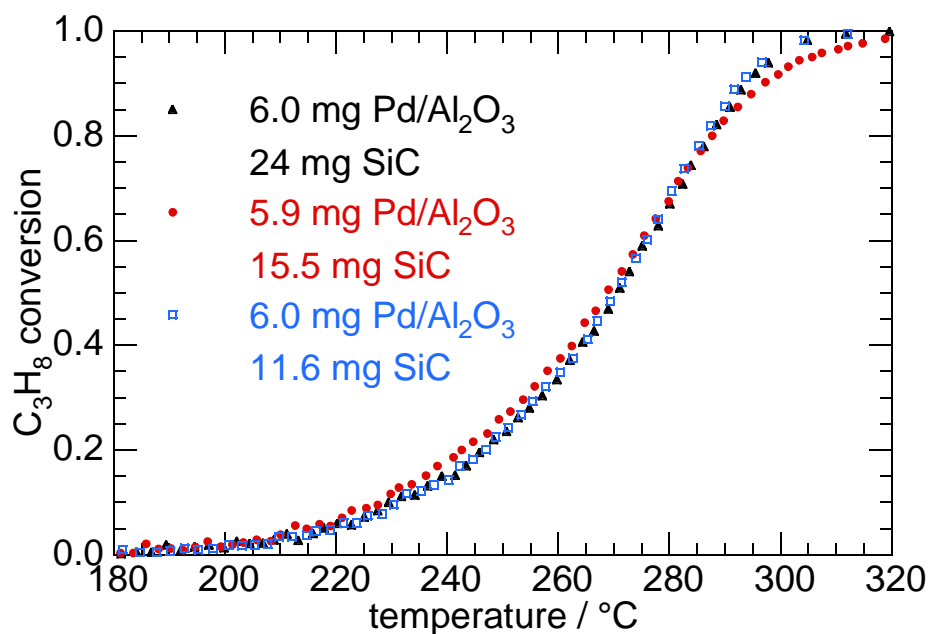


**Fig. A3.2.** Reaction profiles recorded for propane oxidation ( $C_{\text{C}_3\text{H}_{8,0}} = 1000$  ppm,  $C_{\text{O}_{2,0}} = 100,000$  ppm, balance Ar,  $v_0 = 25$  mL min<sup>-1</sup>) over 2 wt% Pd/Al<sub>2</sub>O<sub>3</sub> diluted with various amounts of SiC, at dilution ratios of 1:2 (open blue squares), 1:3 (filled red circles) and 1:4 (filled black triangles). Prior to recording each reaction profile, the catalyst was pre-conditioned at 500 °C ( $X = 1$ ) for 3 h under reaction conditions. Showing every 100<sup>th</sup> data point.

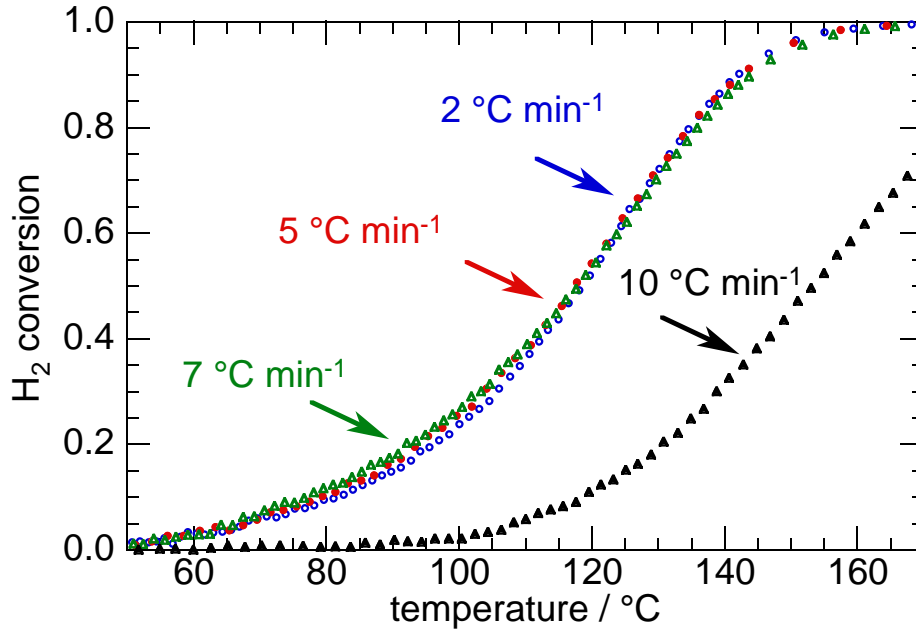


**Fig. A3.3.** Reaction profiles recorded for H<sub>2</sub> oxidation ( $C_{\text{H}_2,0} = 1000$  ppm,  $C_{\text{O}_2,0} = 100,000$  ppm, balance Ar,  $v_0 = 50$  mL min<sup>-1</sup>) over 2 wt% Pd/Al<sub>2</sub>O<sub>3</sub> (11.4 mg) diluted in SiC (33 mg). Recorded with temperature ramp rates of: 2 (open blue circles), 5 (filled red circles), 7 (open green triangles) and 10 °C min<sup>-1</sup> (filled black triangles). Showing every 20<sup>th</sup> data point.

### A3.3. Derivation of kinetic expressions for reaction profiles

A power rate law can be written for  $j + 1$  reactants in terms of the conversion  $X$  of the limiting reactant **a** with inlet concentration  $C_{a,0}$  (mol m<sup>-3</sup>), where  $\Theta_i$  is the ratio of inlet concentrations for reactants **i** and **a**, and  $m_i$  and  $n$  are their reaction orders, Eq. A3.49.

$$-r_a = k[C_a]^n \prod_i^j [C_i]^{m_i} = k[C_{a,0}(1 - X)]^n \prod_i^j \left[ C_{a,0} \left( \Theta_i - \frac{b_i}{a} X \right) \right]^{m_i} \quad (\text{A3.49})$$

The temperature dependence of the rate constant  $k$  is described by the Arrhenius equation, Eq. A3.50, where  $R$  (J mol<sup>-1</sup> K<sup>-1</sup>) is the ideal gas constant. The apparent activation parameters  $A$  and  $E_a$  contain contributions from adsorption (see Eq. A3.7- A3.8), and are

presumed temperature-independent over the range of reaction conditions relevant to the reaction profile ( $0.05 < X < 0.95$ ).

$$k = Ae^{-\frac{E_a}{RT}} \quad (\text{A3.50})$$

The design equation for a packed bed reactor (PBR) expressed in terms of the catalyst mass,  $W_{\text{cat}}$  (g), is shown in Eq. A3.51, where  $v_0$  ( $\text{m}^3 \text{s}^{-1}$ ) is the volumetric flow rate at the reactor inlet, and  $\tau$  is analogous to the space-time.

$$\frac{W_{\text{cat}}}{v_0} = \tau = C_{a,0} \int_0^X \frac{dX}{-r_a} \quad (\text{A3.51})$$

Consequently, a design equation can be written in which  $-r_a$  is the sole temperature-dependent term, Eq. A3.52, and  $\tau_{\text{ref}} = W_{\text{cat}}/v_{0,\text{ref}}$ :

$$\frac{\tau_{\text{ref}}}{C_{a,0,\text{ref}}} = \int_0^X \frac{dX}{-r_a} \quad (\text{A3.52})$$

Assuming the rate constant  $k$  depends only on temperature (i.e., not on reactant concentrations), substitution of Eq. A3.49- A3.50 into Eq. A3.52 yields a general form of the reaction profile kinetic equation, Eq. A3.53.

$$\frac{\tau_{\text{ref}}}{C_{a,0,\text{ref}}} Ae^{-\frac{E_a}{RT}} = \int_0^X \frac{dX}{\left[ C_{a,0,\text{ref}} \frac{T_{\text{ref}}}{T} (1-X) \right]^n \prod_i \left[ C_{a,0,\text{ref}} \frac{T_{\text{ref}}}{T} \left( \Theta_i - \frac{b_i}{a} X \right) \right]^{m_i}} \quad (\text{A3.53})$$

For first-order reactions ( $n = 1$ ,  $m_i = 0$ ), evaluation of the integral gives a simple analytical expression for  $X$ , Eq. A3.54.

$$X = 1 - e^{\left(-\tau_{\text{ref}} \frac{T_{\text{ref}}}{T} A e^{-\frac{E_a}{RT}}\right)} \quad n = 1 \text{ (first-order)} \quad (\text{A3.54})$$

Similarly, for rate laws with other integer order-dependences on a single reactant, we obtain the analytical expressions in Eq. A3.55- A3.57:

$$X = 1 - \sqrt{1 - \frac{2\tau_{\text{ref}}}{C_{a,0,\text{ref}}^2} \frac{T}{T_{\text{ref}}} A e^{-\frac{E_a}{RT}}} \quad n = -1 \text{ (inverse-first-order)} \quad (\text{A3.55})$$

$$X = \frac{\tau_{\text{ref}}}{C_{a,0,\text{ref}}} A e^{-\frac{E_a}{RT}} \quad n = 0 \text{ (zeroth-order)} \quad (\text{A3.56})$$

$$X = 1 - \frac{1}{1 + C_{a,0,\text{ref}} \tau_{\text{ref}} \left(\frac{T_{\text{ref}}}{T}\right)^2 A e^{-\frac{E_a}{RT}}} \quad n = 2 \text{ (second-order)} \quad (\text{A3.57})$$

For a general rate law with a (to-be-determined)  $n^{\text{th}}$ -order-dependence on a single reactant, we obtain the analytical expression in Eq. A3.58 (only valid for  $n \neq 1$ ):

$$X = 1 - \left\{1 + (n - 1) \tau_{\text{ref}} C_{a,0,\text{ref}}^{n-1} \left(\frac{T_{\text{ref}}}{T}\right)^n A e^{-\frac{E_a}{RT}}\right\}^{\frac{1}{1-n}} \quad (n^{\text{th}}\text{-order}) \quad (\text{A3.58})$$

For rate laws that depend on the concentrations of two different species, the integral in Eq. A3.53 can be still evaluated if  $\Theta_b = b/a$ , giving the analytical expression in Eq. A3.59 (only valid only for  $n + m \neq 1$ ):

$$X = 1 - \left( 1 + (n + m - 1) \left( \frac{T_{\text{ref}}}{T} \right)^{n+m} \left( \frac{b}{a} \right)^m C_{a,0,\text{ref}}^{n+m-1} \tau_{\text{ref}} A e^{-\frac{E_a}{RT}} \right)^{\frac{1}{1-n-m}} \quad (\text{A3.59})$$

When  $\Theta_b \neq b/a$ , numerical integration is required. However, approximate analytical solutions (Eq. A3.60- A3.61) are obtained when  $(\Theta_b - X b/a) \approx \Theta_b$ . When  $\Theta_b \gg b/a$  (i.e., all other reactants present in large excess over the limiting reactant), the approximation is valid for all values of  $X$ . However, when  $\Theta_b \approx b/a$ , it should only be used for low-to-moderate values of  $X$  (see Fig. A3.4).

$$X = 1 - e^{\left( -\tau_{\text{ref}} C_{a,0,\text{ref}}^m \left( \frac{T_{\text{ref}}}{T} \right)^{m+1} \Theta_b^m A e^{-\frac{E_a}{RT}} \right)} \quad n = 1 \text{ (first-order in lim. reactant)} \quad (\text{A3.60})$$

$$X = 1 - \left( 1 + (n - 1) \tau_{\text{ref}} C_{a,0,\text{ref}}^{n+m-1} \left( \frac{T_{\text{ref}}}{T} \right)^{n+m} \Theta_b^m A e^{-\frac{E_a}{RT}} \right)^{\frac{1}{1-n}} \quad n \neq 1 \quad (\text{A3.61})$$

Reaction profiles for CO oxidation with a slight excess  $\text{O}_2$  ( $\Theta_b = 1$ ) were simulated using the analytical solution, Eq. A3.61, and the numerical solution to Eq. A3.53. The analytical solution deviates from the numerical solution at large conversions ( $X > 0.6$ ) because  $\Theta_b \approx b/a$ . However, the reaction profiles are nearly superposable below this conversion, validating the assumption that  $(\Theta_b - X b/a) \approx \Theta_b$  at low values of  $X$ .



Therefore reaction profiles for experiments with a small amount of excess reagents must be truncated in order to use Eq. A3.60-61 for curve-fitting.

#### A3.4. Analysis of simulated isothermal kinetic data

Isothermal kinetic data were simulated in order to compare the accuracy of Arrhenius plots made using either  $-r_a$  or  $k$ . Data were simulated for a first-order reaction, using arbitrary kinetic parameters, over the temperature range 187-327 °C. Arrhenius plots were constructed in both differential ( $X < 0.10$ ) and non-differential regimes ( $0 < X < 0.66$ ), Fig. A3.4. The linear fit obtained using rate constants simulated over the full temperature range (blue) returns the chosen values for  $E_a$  and  $A$  precisely. However, the linear fit obtained using rates over the same temperature range (black) yields a much lower value for  $E_a$ , 84 kJ mol<sup>-1</sup>. This is a consequence of the non-negligible concentration gradient in the reactor, and the first-order dependence of the rate on concentration. Similar results were obtained by plotting  $\ln(X)$  or  $\ln(\text{TOF})$ : use of non-differential conditions leads to curvature in the Arrhenius plot and inaccurate activation parameters. (However, if the reaction is overall pseudo-zeroth-order,  $-r_a = k$ . Consequently, the use of  $-r_a$ ,  $X$  or TOF instead  $k$  in the Arrhenius plot has no effect on the result).

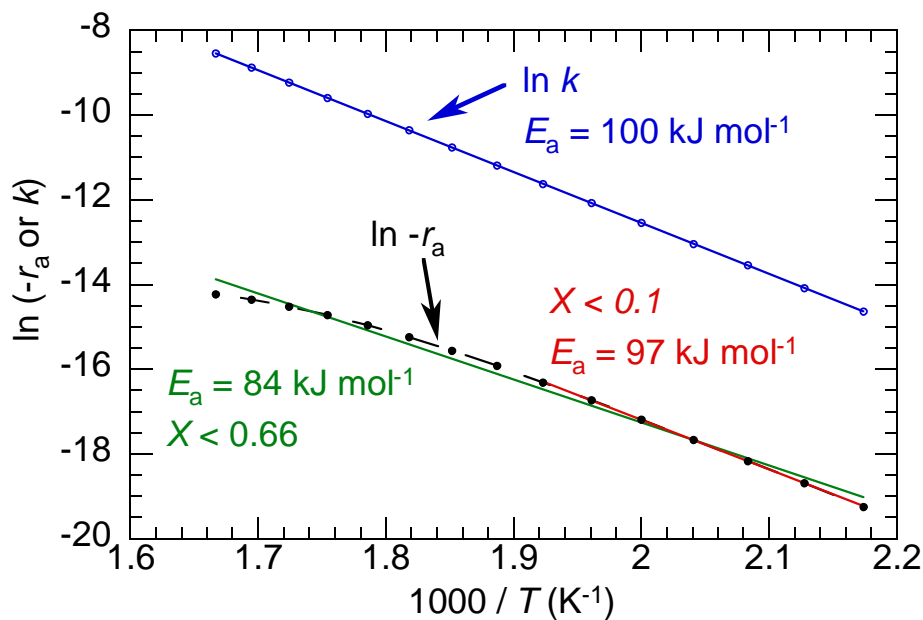


**Fig. A3.4.** Arrhenius plots constructed using simulated rates (black circles) and rate constants (open blue circles), for a first-order reaction with  $E_a = 100 \text{ kJ mol}^{-1}$ ,  $A = 10^5 \text{ s}^{-1}$ ,  $C_{a,0} = 0.01 \text{ mol m}^{-3}$ ,  $W_{\text{cat}} = 0.01 \text{ g}$  and  $F_{a,0} = 10^{-8} \text{ mol s}^{-1}$ . Linear fits are shown for  $X < 0.66$  ( $k$ : blue;  $-r_a$ : green) and for  $X < 0.1$  ( $-r_a$ : red).

Consequently, for reactions with an overall non-zeroth-order concentration dependence, the temperature range must be restricted to values that give low conversions (e.g., less than 0.10, corresponding to near-gradientless or differential conditions) in order to obtain accurate activation energies. With this constraint, the simulated Arrhenius plot with  $-r_a$  (red) returns a value for  $E_a$ ,  $97 \text{ kJ mol}^{-1}$ , just 3 % lower than the true value. This would likely be within the measurement error of the actual value in a real experiment. However, the value of  $A$  calculated from the intercept of the Arrhenius plot,  $\ln(AC_{a,0})$ , is  $5 \times 10^4 \text{ s}^{-1}$ . The error is 100 % even in “data” with no experimental uncertainty, and is caused by the invalid assumption that  $X = 0$  even when the conditions are differential.

### A3.5. Arrhenius plots based on isothermal kinetic experiments

To obtain activation parameters by the conventional method (for comparison to values extracted from reaction profiles), the reactor temperature was set to a value corresponding to conversion less than  $X = 0.1$  and held at this value for approx. 1 h while the mass spectrometer signal intensity for  $H_2$  ( $m/z = 2$ ),  $C_3H_8$  ( $m/z = 29$ ) or  $CO_2$  ( $m/z = 44$ ) was recorded. For  $H_2$  and  $C_3H_8$ ,  $I_{in}$  was also recorded before each isothermal experiment (described above). After all isothermal experiments were performed, the temperature was set to a value corresponding to complete conversion, to obtain  $I_{zero}$ . Kinetic parameters were calculated as described above (section 1.1 for  $X$ , section 1.2 for  $-r_a$ , and section 1.3 for  $k$ ). For CO oxidation,  $I_{zero}$  was recorded after each isothermal experiment, by reducing the temperature to 30 °C.  $I_{calibration}$  was recorded after all isothermal experiments were completed in the same way as described above (section A3.1.1).

Arrhenius plots constructed for the oxidation of  $H_2$ , CO and  $C_3H_8$  over  $Pd/Al_2O_3$  are shown in Figs. A3.5-7. For each reaction, the same values for  $E_a$  were obtained from Arrhenius plots made using either  $-r_a$  or  $k$ . In order to extract values for  $A$ , Arrhenius plots must be constructed using apparent rate constants (see section A3.4). All kinetic parameters are summarized in Table 3.1.

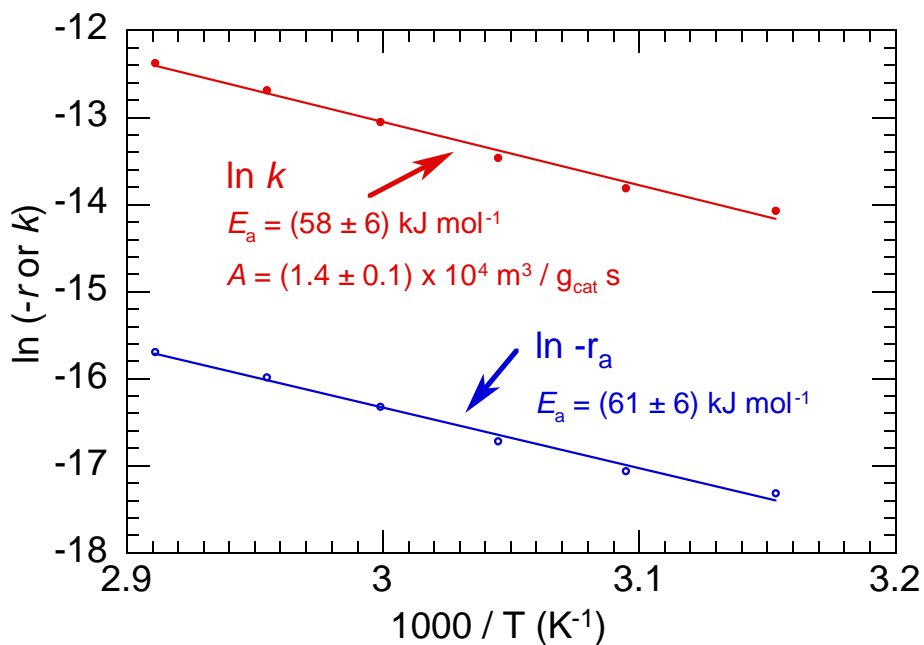


**Fig. A3.5.** Arrhenius plot for  $\text{H}_2$  oxidation over  $\text{Pd}/\text{Al}_2\text{O}_3$  (11.4 mg) diluted in SiC (34.5 mg), constructed using either  $k$  (filled red circles) or  $-r_a$  (open blue circles). To calculate  $k$  values, reaction orders were assumed to be +1 for  $\text{H}_2$  and 0 for  $\text{O}_2$ . The catalyst was pre-conditioned at 200 °C for 3 h, in the presence of the flowing feed ( $C_{\text{H}_2,0} = 500$  ppm;  $C_{\text{O}_2,0} = 100,000$  ppm, balance Ar,  $v_0 = 50 \text{ mL min}^{-1}$ ). Isothermal measurements were made for  $45 < T < 70$  °C and  $0.02 < X < 0.10$ .

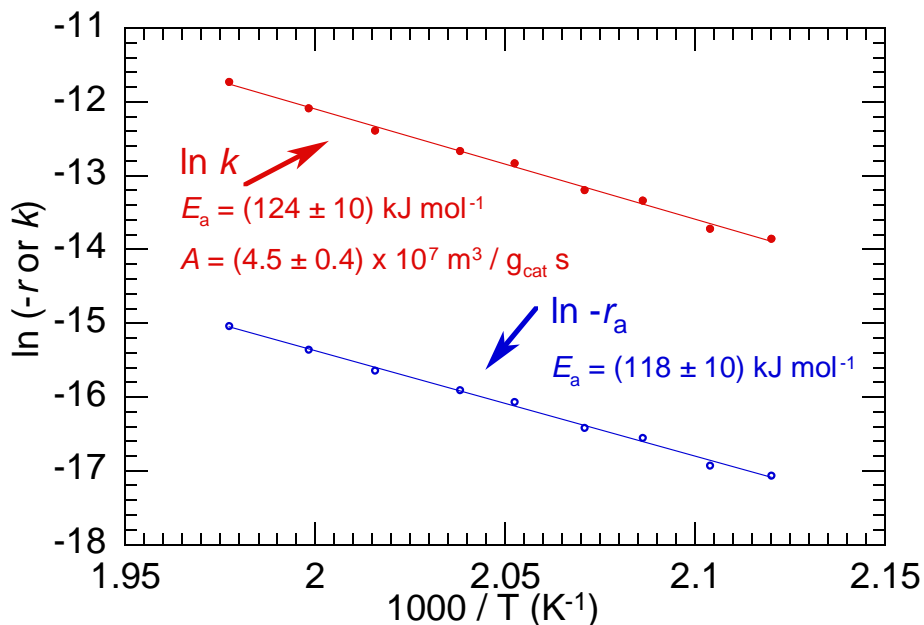


**Fig. A3.6.** Arrhenius plot for  $\text{C}_3\text{H}_8$  oxidation over  $\text{Pd}/\text{Al}_2\text{O}_3$  (11.8 mg) diluted in SiC (30.9 mg), constructed using either  $k$  (filled red circles) or  $-r_a$  (open blue circles). To calculate  $k$  values, reaction orders were assumed to be +1 for  $\text{C}_3\text{H}_8$  and 0 for  $\text{O}_2$ . The catalyst was pre-conditioned at 500 °C for 3 h in the presence of the flowing feed ( $C_{\text{C}_3\text{H}_{8,0}} = 1000$  ppm;  $C_{\text{O}_2,0} = 100,000$  ppm, balance Ar,  $v_0 = 50 \text{ mL min}^{-1}$ ). Isothermal measurements were made for  $208 < T < 233$  °C and  $0.01 < X < 0.09$ .

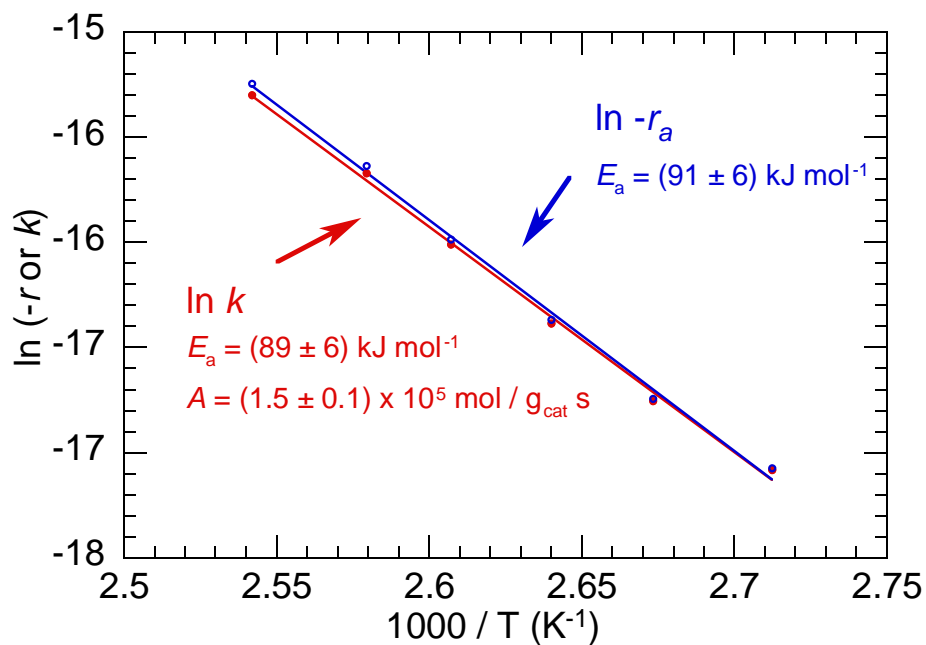


**Fig. A3.7.** Arrhenius plot for CO oxidation over Pd/Al<sub>2</sub>O<sub>3</sub> (11.4 mg) diluted in SiC (35.4 mg), constructed using either  $k$  (filled red circles) or  $-r_a$  (open blue circles). To calculate  $k$  values, reaction orders were assumed to be -1 for CO and +1 for O<sub>2</sub>. The catalyst was pre-conditioned at 180 °C for 3 h, in the presence of the flowing feed ( $C_{\text{CO},0} = 1000$  ppm;  $C_{\text{O}_2,0} = 1000$  ppm, balance Ar,  $v_0 = 50$  mL min<sup>-1</sup>). Isothermal measurements were made for  $95 < T < 120$  °C and  $0.01 < X < 0.10$ .

### A3.6. Experimental reaction profiles

Prior to recording reaction profiles, the catalyst was pre-conditioned under reaction conditions for 3 h at a temperature corresponding to  $X = 1$  (200, 500, and 180 °C, for H<sub>2</sub>, C<sub>3</sub>H<sub>8</sub>, and CO oxidation, respectively). Reaction profiles for H<sub>2</sub> oxidation recorded in sequential fashion are superposable after pre-conditioning the catalyst, Fig. A3.8. Thus the kinetic equations developed above in section A3.3 can be curve-fitted to the sets of experimental reaction profiles.

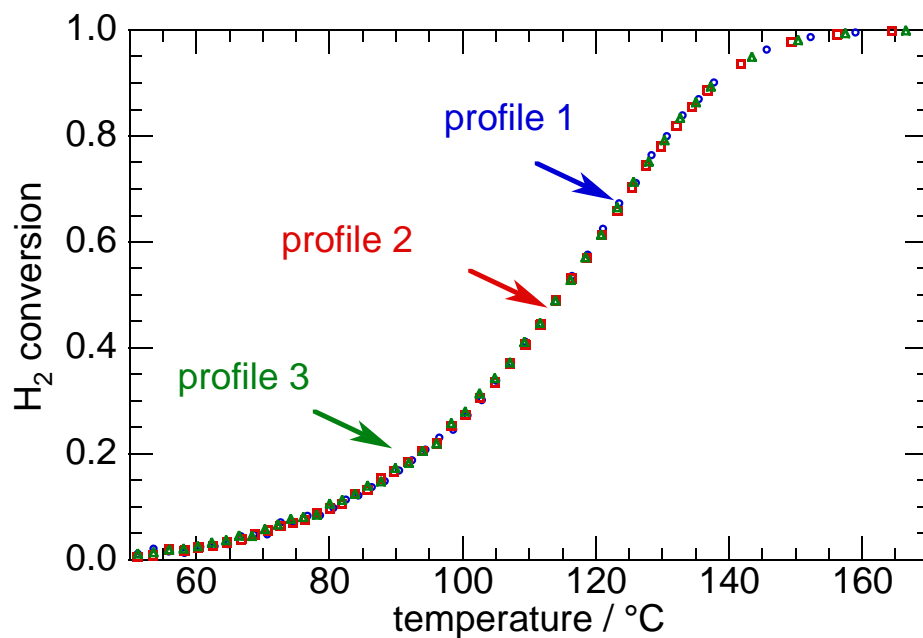


**Fig. A3.8.** Comparison of reaction profiles, recorded sequentially, for  $\text{H}_2$  oxidation ( $C_{\text{H}_{2,0}} = 1000$  ppm,  $C_{\text{O}_{2,0}} = 100,000$  ppm, balance Ar,  $v_0 = 40$  mL  $\text{min}^{-1}$ ) over 2 wt% Pd/ $\text{Al}_2\text{O}_3$  (11.4 mg) diluted in SiC (34.5 mg). The first profile (open blue circles), second profile (open red squares), and third profile recorded (open green triangles) are superposable, indicating a high level of reproducibility. Prior to recording each reaction profile, the catalyst was pre-conditioned at 200 °C ( $X = 1$ ) for 3 h under reaction conditions. Showing every 20<sup>th</sup> data point.

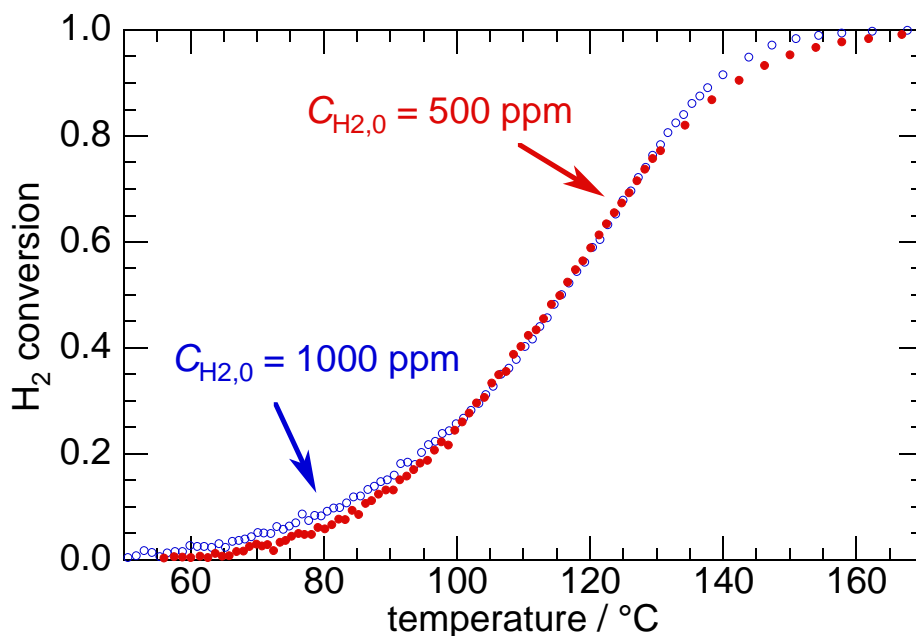


**Fig. A3.9.** Reaction profiles recorded for  $\text{H}_2$  oxidation over 2 wt%  $\text{Pd}/\text{Al}_2\text{O}_3$  (11.4 mg) diluted in SiC (33 mg), recorded at different inlet concentrations of the limiting reactant:  $C_{\text{H}_2,0} = 1000$  ppm (open blue circles) and  $C_{\text{H}_2,0} = 500$  ppm (filled red circles). For both reaction profiles,  $C_{\text{O}_2,0} = 100,000$  ppm and  $v_0 = 50 \text{ mL min}^{-1}$ . The reaction profiles are nearly superposable, even though  $C_{\text{H}_2}$  changes by a factor of two. This result is consistent with a reaction that is first-order in the limiting reagent ( $\text{H}_2$ ). (Note these reaction profiles were recorded on different days with different catalyst samples, which may explain their slight differences.) Prior to recording each reaction profile, the catalyst was pre-conditioned at  $200^\circ\text{C}$  ( $X = 1$ ) for 3 h under reaction conditions. Showing every  $20^{\text{th}}$  data point.

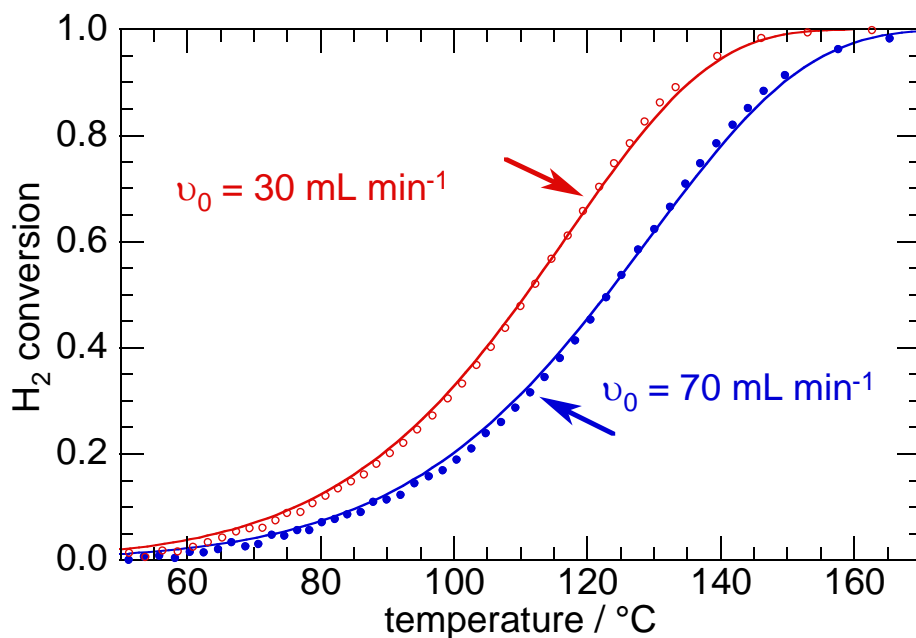


**Fig. A3.10.** Individual curve-fits of Eq. A3.61 (lines) to reaction profiles (symbols) for  $\text{H}_2$  oxidation ( $C_{\text{H}_2,0} = 1000$  ppm,  $C_{\text{O}_2,0} = 100,000$  ppm, balance Ar) over 2 wt%  $\text{Pd}/\text{Al}_2\text{O}_3$  (11.4 mg) diluted in SiC (34.5 mg). Reaction orders for  $\text{H}_2$ ,  $n$ , and  $\text{O}_2$ ,  $m$ , were refined. Recorded at flow rates of 30 (open red circles) and 70  $\text{mL min}^{-1}$  (filled blue circles). Only one reaction profile (of two recorded) is shown for each flow rate. Prior to recording each reaction profile, the catalyst was pre-conditioned at 200 °C ( $X = 1$ ) for 3 h under reaction conditions. Showing every 20<sup>th</sup> data point. Profiles were fit from 46 °C  $\leq T \leq$  195 °C.



## References

- [1] F.V. Hanson, M. Boudart, Reaction between  $H_2$  and  $O_2$  over supported platinum catalysts, *J. Catal.* 53 (1978) 56-67.
- [2] C.F. Cullis, T.G. Nevell, Kinetics of catalytic-oxidation over palladium of some alkanes and cycloalkanes, *Proc. Roy. Soc. Lond. A* 349 (1976) 523-534.
- [3] T. Engel, G. Ertl, Molecular beam investigation of catalytic oxidation of CO on Pd (111), *J. Chem. Phys.* 69 (1978) 1267-1281.
- [4] D.E. Mears, Tests for transport limitations in experimental catalytic reactors, *Ind. Eng. Chem. Proc. Des. Dev.* 10 (1971) 541-547.
- [5] P.B. Weisz, C.D. Prater, Interpretation of measurements in experimental catalysis, *Adv. Catal.* 6 (1954) 143-196.
- [6] D.E. Mears, Diagnostic criteria for heat transport limitations in fixed bed reactors, *J. Catal.* 20 (1971) 127-131.
- [7] A.M. Ganzler, M. Casapu, A. Boubnov, O. Muller, S. Conrad, H. Lichtenberg, R. Frahm, J.D. Grunwaldt, Operando spatially and time-resolved X-ray absorption spectroscopy and infrared thermography during oscillatory CO oxidation, *J. Catal.* 328 (2015) 216-224.
- [8] A. Steigel, J. Sauer, G. Binsch, D.A. Kleier, Nitrogen analogs of cycloheptatrienes and norcaradienes. Nuclear magnetic resonance study of their thermodynamic and kinetic properties, *J. Am. Chem. Soc.* 94 (1972) 2770-2779.
- [9] T. Uda, M. Tanaka, K. Munakata, Scaling up experiments of honeycomb catalysts for oxidation of hydrogen and methane gases, *Fusion Eng. Des.* 87 (2012) 900-904.
- [10] S.P. Asprey, Y. Naka, Mathematical problems in fitting kinetic models - Some new perspectives, *J Chem. Eng. Jpn.* 32 (1999) 328-337.
- [11] D.J. Pritchard, D.W. Bacon, Statistical assessment of chemical kinetic models, *Chem. Eng. Sci.* 30 (1975) 567-574.
- [12] G.E.P. Box, Fitting empirical data, *Ann. N.Y. Acad. Sci.* 86 (1960) 792-816.
- [13] M. Aryafar, F. Zaera, Kinetic study of the catalytic oxidation of alkanes over nickel, palladium, and platinum foils, *Catal. Lett.* 48 (1997) 173-183.
- [14] Y.F.Y. Yao, Oxidation of alkanes over noble metal catalysts, *Ind. Eng. Chem. Prod. Res. Dev.* 19 (1980) 293-298.
- [15] L.L. Hegedus, S.H. Oh, K. Baron, Multiple steady states in an isothermal, integral reactor - The catalytic oxidation of carbon monoxide over platinum-alumina, *AIChE J.* 23 (1977) 632-642.
- [16] P.J. Berlowitz, C.H.F. Peden, D.W. Goodman, Kinetics of CO oxidation on single-crystal Pd, Pt, and Ir, *J. Phys. Chem.* 92 (1988) 5213-5221.
- [17] N.W. Cant, P.C. Hicks, B.S. Lennon, Steady-state oxidation of carbon monoxide over supported noble metals with particular reference to platinum, *J. Catal.* 54 (1978) 372-383.
- [18] S.M. Landry, R.A.D. Betta, J.P. Lu, M. Boudart, Catalytic oxidation of carbon monoxide on palladium. 1. Effect of pressure, *J. Phys. Chem.* 94 (1990) 1203-1206.
- [19] Y.F.Y. Yao, The oxidation of CO and hydrocarbons over noble-metal catalysts, *J. Catal.* 87 (1984) 152-162.
- [20] S.M. McClure, D.W. Goodman, New insights into catalytic CO oxidation on Pt-group metals at elevated pressures, *Chem. Phys. Lett.* 469 (2009) 1-13.

- [21] H. Conrad, G. Ertl, J. Koch, E.E. Latta, Adsorption of CO on Pd Single-Crystal Surfaces, *Surf. Sci.* 43 (1974) 462-480.
- [22] W.K. Kuhn, J. Szanyi, D.W. Goodman, CO Adsorption on Pd(111) - the Effects of Temperature and Pressure, *Surf. Sci.* 274 (1992) L611-L618.
- [23] J.H. Fischer-Wolfarth, J.A. Farmer, J.M. Flores-Camacho, A. Genest, I.V. Yudanov, N. Rosch, C.T. Campbell, S. Schauermaun, H.J. Freund, Particle-size dependent heats of adsorption of CO on supported Pd nanoparticles as measured with a single-crystal microcalorimeter, *Phys. Rev. B* 81 (2010) 241416.
- [24] J.M. Flores-Camacho, J.H. Fischer-Wolfarth, M. Peter, C.T. Campbell, S. Schauermaun, H.J. Freund, Adsorption energetics of CO on supported Pd nanoparticles as a function of particle size by single crystal microcalorimetry, *Phys. Chem. Chem. Phys.* 13 (2011) 16800-16810.
- [25] M. Peter, S. Adamovsky, J.M.F. Camacho, S. Schauermaun, Energetics of elementary reaction steps relevant for CO oxidation: CO and O<sub>2</sub> adsorption on model Pd nanoparticles and Pd(111), *Faraday Discuss.* 162 (2013) 341-354.
- [26] O. Dulaurent, K. Chandes, C. Bouly, D. Bianchi, Heat of adsorption of carbon monoxide on various Pd-containing solids using in situ infrared spectroscopy at high temperatures, *J. Catal.* 192 (2000) 273-285.
- [27] A.K. Santra, D.W. Goodman, Catalytic oxidation of CO by platinum group metals: from ultrahigh vacuum to elevated pressures, *Electrochim. Acta* 47 (2002) 3595-3609.
- [28] B.M. Kunkel, B.C. Peoples, C.M. Yung, S.L. Scott, Clay-catalyzed cracking leads to suppressed flammability in clay-polyolefin nanocomposites, *Macromol. Mater. Eng.* 296 (2011) 1075-1080.
- [29] M.M. Papari, D. Mohammad-Aghaiee, B. Haghighi, A. Boushehri, Transport properties of argon-hydrogen gaseous mixture from an effective unlike interaction, *Fluid Phase Equilib.* 232 (2005) 122-135.
- [30] W.E. Ranz, W.R. Marshall, Evaporation from drops part 2, *Chem. Eng. Prog.* 48 (1952) 173-180.
- [31] J. Kestin, W.A. Wakeham, S.T. Ro, Viscosity of noble gases in temperature range 25-700 degrees, *J. Chem. Phys.* 56 (1972) 4119-4124.
- [32] B.A. Younglove, H.J.M. Hanley, The viscosity and thermal conductivity coefficients of gaseous and liquid argon, *J. Phys. Chem. Ref. Data* 15 (1986) 1323-1337.
- [33] M.W. Chase, Jr., NIST-JANAF Thermochemical tables, fourth ed., American Institute of Physics, Woodbury, NY, 1998.
- [34] D.A. Pittam, G. Pilcher, Measurements of heats of combustion by flame calorimetry methane, ethane, propane, n-butane and 2-methylpropane, *J. Chem. Soc. Faraday Trans. 1* 68 (1972) 2224-2229.
- [35] CODATA recommended key values for thermodynamics, 1975 Report of CODATA Task Group on key values for thermodynamics, 1975, *J. Chem. Thermodyn.* 8 (1976) 603-605.

## **Chapter 4: Coupled Variable-Temperature Kinetic Analysis and *Operando* Spectroscopy Investigation of CO Oxidation Catalyzed by Pd/Al<sub>2</sub>O<sub>3</sub>**

### **4.1. Introduction**

#### **4.1.1. Light-off for CO oxidation catalyzed by Pd**

The oxidation of CO over platinum-group metals continues to be of interest as researchers propose new reaction mechanisms [1] and employ novel *in situ* and *operando* experimental techniques to investigate the dynamic surface chemistry [2-12]. Since the early work of Ertl [13] and Turner et al. [14, 15], CO oxidation on Pt/Al<sub>2</sub>O<sub>3</sub> has been the focus of many *in situ* and *operando* investigations which attempt to explain the abrupt and sudden increase in conversion (light-off), hysteresis, and oscillations in activity at constant temperature. Possible explanations include the facile restructuring of the catalytic surface [12], formation of a highly active surface oxide [4, 7, 10, 11], and light-off caused by hot spots that occur when the concentration of CO is low enough not to poison the catalyst [3, 16]. *In situ* and *operando* infrared spectroscopy (IR) and X-ray absorption spectroscopy (XAS) correlate the reaction progress to the local environment of CO and the chemical state of the catalyst. During CO oxidation catalyzed by Pd/Al<sub>2</sub>O<sub>3</sub> under excess O<sub>2</sub>, *operando* IR and XAS suggested that light-off and the abrupt decrease in conversion during cooling (extinction) are caused by the rapid formation and destruction of a meta-stable surface oxide [2]. In one study, monitoring of CO conversion via mass spectrometry captures rapid oscillations; however the slower nature and lower temperature resolution of IR and XAS

measurements made observation of abrupt changes in surface chemistry difficult. Instead, spectra were recorded at temperatures above and below light-off/extinction. In another study, *ex situ* transmission electron microscopy (TEM) and X-ray photoelectron spectroscopy (XPS) studies of CO oxidation catalyzed by large PdO particles suggested that light-off, extinction, and oscillations in activity were due to the growth of Pd(0) nanoparticles on a solid PdO core [17, 18].

#### 4.1.2. Variable-temperature analysis of reaction profiles

In a previous study [19], analytical expressions for reaction profiles, in which the conversion,  $X$ , is plotted vs. the reactor temperature,  $T$ , were developed using the packed bed reactor (PBR) design equation, Arrhenius equation, and a simple power rate law for  $j + 1$  reactants [19], Eq. 4.1.

$$-r_a = k[C_a]^n \prod_i^j [C_i]^{m_i} = k[C_{a,0}(1 - X)]^n \prod_i^j \left[ C_{a,0} \left( \Theta_i - \frac{b_i}{a} X \right) \right]^{m_i} \quad (4.1)$$

Here, the ratio of the inlet concentrations for species **b** and **a** is  $\Theta_b$ . The stoichiometric coefficients for the excess reactant, **b**, and the limiting reactant, **a**, are  $b$  and  $a$ , respectively. The residence time of the reactor ( $\tau = W_{\text{cat}}/v_0$ ) is the ratio of the mass of catalyst used,  $W_{\text{cat}}$ , to the volumetric flow rate,  $v_0$ . The reaction orders are  $n$  and  $m$  with respect to reactants **a** and **b**. Variable-temperature reaction profiles were recorded in a PBR with a constant temperature ramp rate, however the catalyst bed has been shown to be isothermal within the measurement time [19].

Eq. 4.1 can be solved analytically if  $\Theta_b = b/a$ , Eq. 4.2. Otherwise ( $\Theta_b - X b/a$ ) can be approximated as  $\Theta_b$ , which is valid for all  $X$  if  $\Theta_b \gg b/a$ , Eq. 4.3. If there is only a slight excess or if  $\Theta_b = b/a$ , Eq. 4.3 is valid for small to moderate values of  $X$  [19].

$$X = 1 - \left[ 1 + (n + m - 1) \left( \frac{T_{\text{ref}}}{T} \right)^{n+m} \left( \frac{b}{a} \right)^m C_{a,0,\text{ref}}^{n+m-1} \tau_{\text{ref}} A e^{-\frac{E_a}{RT}} \right]^{\frac{1}{1-n-m}} \quad (4.2)$$

$$X = 1 - \left[ 1 + (n - 1) \tau_{\text{ref}} C_{a,0,\text{ref}}^{n+m-1} \left( \frac{T_{\text{ref}}}{T} \right)^{n+m} \Theta_b^m A e^{-\frac{E_a}{RT}} \right]^{\frac{1}{1-n}} \quad (4.3)$$

### 4.1.3. Objectives

In this study, we explore the oxidation of CO with stoichiometric  $O_2$  ( $C_{O_2}/C_{CO} = 1/2$ ), catalyzed by Pd/Al<sub>2</sub>O<sub>3</sub>, using variable-temperature kinetic analysis in a packed bed reactor (PBR). The active state of the catalyst will be investigated above and below light-off and extinction using *operando* IR and XAS. Stoichiometric reaction conditions are less oxidizing than previous reaction atmospheres studied, and the jump in conversion at light-off is lower. These conditions allow for unique information about the active site(s) during light-off which is not available under highly oxidizing atmospheres.

## 4.2. Experimental methods

### 4.2.1. Materials

The catalyst is 2.0 wt% PdO supported on  $\gamma$ -Al<sub>2</sub>O<sub>3</sub> (Sasol HTA-102, surface area 76 m<sup>2</sup> g<sup>-1</sup>, pore volume 0.60 cm<sup>3</sup> g<sup>-1</sup>, median pore radius 15 nm, Pd particle size of (2.8 ± 0.6) Å). It was sieved to a mesh size of 80-100 (150-180 µm) and diluted with SiC (Sigma

Aldrich, >97.5 %, 200 mesh size) in a 1:3 ratio (w/w). Ar (99.999 %), O<sub>2</sub> (99.99 %; 20% in He, 99.99%; and 5000 ppm in Ar, 99.99 %), CO<sub>2</sub> (5000 ppm in Ar, 99.99 %), and CO (5005 ppm in Ar, 99.99 %; and 5000 ppm in He, 99.99%) were supplied by Praxair.

#### 4.2.2. Reactivity studies

CO oxidation was performed in a Hiden Catlab microreactor. The catalyst bed ( $5 \times 10^{-8} \text{ m}^3$ ; 0.05 mL), was packed in a quartz tube (inner diameter of 3.88 mm, axial length of 4 mm) between plugs of quartz wool and heated in a furnace at a constant rate of  $5 \text{ K min}^{-1}$ . The pressure drop was measured to be less than 70 mbar. The temperature gradient across the catalyst bed was shown to be negligible [19], meaning the PBR is isothermal during each measurement. The temperature was monitored by a single K-Type thermocouple (Omega KQXL, 0.05 s response time) in contact with the inlet of the catalytic bed. A close-coupled online quadrupole mass spectrometer (HR-20, Hiden Analytical) monitored the effluent gas stream. The signal for CO<sub>2</sub> ( $m/z = 44$ ), whose intensity was recorded every 0.6 s, was monitored with a secondary electron multiplier (SEM) detector.

Each catalyst sample was pre-treated in a flow of the appropriate feed gas for 3 h at a temperature for which full conversion was achieved. Reaction profiles were recorded for volumetric flow rates between 30 and  $50 \text{ mL min}^{-1}$  (corresponding to gas-hourly space velocities, GHSV, of  $3 - 9 \times 10^4 \text{ h}^{-1}$ ), varying in random order. Three reaction profiles were recorded sequentially at each flow rate. For stoichiometric CO oxidation the reactant atmosphere was 1000 ppm CO with 500 ppm O<sub>2</sub> diluted in Ar. Reaction profiles were also recorded with 2000 ppm CO + 1000 ppm O<sub>2</sub> diluted in Ar.

#### 4.2.3. *Operando* IR spectroscopy

A full description of the experiment was detailed previously [2]. Transmission *operando* IR spectra was performed in a quartz tube (200 mm x 30 mm) sealed with CaF<sub>2</sub> windows. 25 mg of Pd/Al<sub>2</sub>O<sub>3</sub> was pressed into a pellet (16 mm diameter x 0.1 mm). All gasses were dried with an in-line dry ice/methanol bath maintained at -65 °C. The IR cell was purged with CO<sub>2</sub>-free air, calcined in dry O<sub>2</sub> for 3 h at 250 °C at a flow rate of 50 mL min<sup>-1</sup>. The reactor was cooled to room temperature before the reaction atmosphere began to flow (2000 ppm CO, 1000 ppm O<sub>2</sub>, balance Ar,  $v_0 = 50 \text{ mL min}^{-1}$ ). Spectra were recorded every 10 °C (after the temperature was stabilized for 0.5 h) up to 250 °C, with a resolution of 0.5 cm<sup>-1</sup>.

CO<sub>2</sub> conversion was calculated from the area of the IR signal at 2347 cm<sup>-1</sup> for gas phase CO<sub>2</sub>. Signals for CO in the gas phase were subtracted with spectra of feed gas at the same temperature using IRSolution software (Shimadzu). Deconvolution of the spectra was performed with OriginLab.

#### 4.2.4. *In situ* XAS

A full description of *in situ* XAS and the reactor were detailed previously [2]. Pd K-edge XAS was collected in a custom aluminum flow cell with Kapton windows. Extended X-ray absorption fine structure (EXAFS) measurements were made on Beamline 4-1 at the Stanford Synchrotron Radiation Lightsource (SSRL). A Si(220) double crystal monochromator was used. The beam was detuned 30% to remove higher harmonics. 15 mg Pd/Al<sub>2</sub>O<sub>3</sub> was pressed into a pellet (10 mm x 3 mm) and loaded perpendicular to the X-ray beam. The pellet was calcined (20% O<sub>2</sub>, balance He) for 2 h at 250 °C before catalysis. The cell was returned to room temperature before spectra were collected. The reactant gas (2000

ppm CO, 1000 ppm O<sub>2</sub>, balance He) was flown across the catalyst pellet. The reactor was stabilized at each temperature for 0.5 h before spectra were recorded. A close-coupled online quadrupole mass spectrometer (Pfeiffer vacuum Omnistar) monitored the effluent gas stream. The signal for CO<sub>2</sub> ( $m/z = 44$ ), whose intensity was recorded every 0.6 s, was monitored with a secondary electron multiplier (SEM) detector. The XAS data were normalized and calibrated using Athena and Artemis software packages [20].

### 4.3. Results

#### 4.3.1. Variable-temperature kinetic analysis

CO oxidation was investigated using a stoichiometric CO/O<sub>2</sub> ratio ( $C_{\text{CO},0}/C_{\text{O}_2,0} = b/a = 2$ ) and volumetric flow rates between 30 and 50 mL min<sup>-1</sup>. The experimental profiles are shown in Figure 4.1(A). They are qualitatively similar to profiles simulated (Fig. A4.1) for an overall pseudo-zero-order reaction, caused by opposing reaction orders for CO (-1) and O<sub>2</sub> (+1) in the power rate law, in combination with the stoichiometric ratio of their inlet concentrations [21]. The rate of change of the conversion begins to decrease near  $X \approx 0.8$ , unlike a typical zeroth-order reaction profile (which contains a discontinuity at  $X = 1$ , Fig. A4.1). Above  $X \approx 0.90$ , the conversion increases abruptly by ca. 0.05, observable as a discontinuity in the reaction profile. The conversion then decreases steadily, to a final maximum conversion of 0.95 that does not change with increasing temperature.



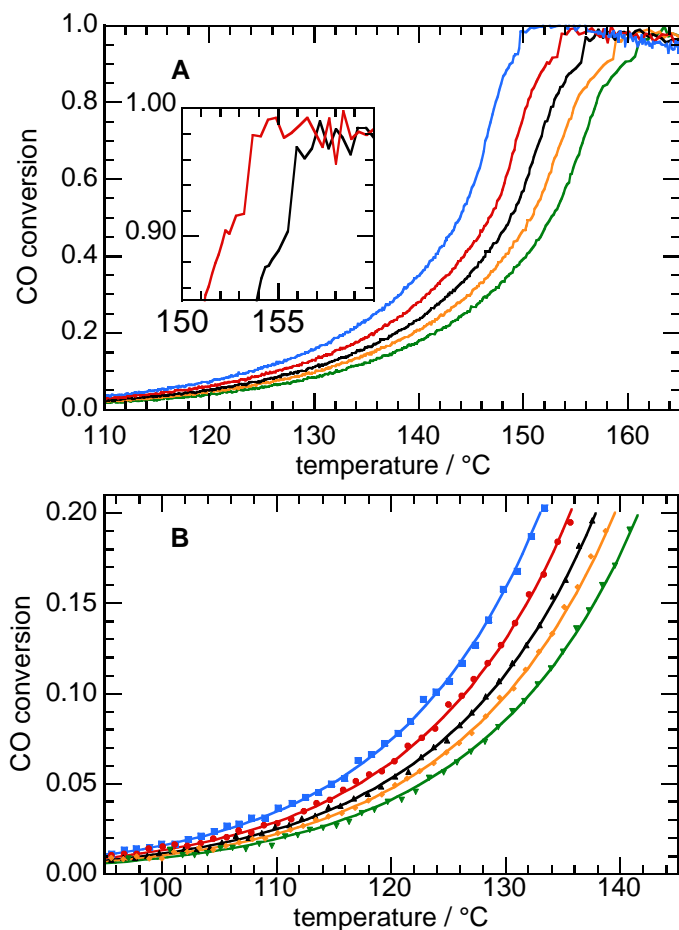


**Fig. 4.1.** Stoichiometric CO oxidation catalyzed by Pd/Al<sub>2</sub>O<sub>3</sub>.

(A) Reaction profiles (lines) for CO oxidation (1000 ppm CO, 500 ppm O<sub>2</sub>, balance Ar) over Pd/Al<sub>2</sub>O<sub>3</sub> (11.8 mg) diluted in SiC (30.9 mg). Only one reaction profile (of three recorded) is shown for each flow rate (GHSV = 3.8 – 8.9 × 10<sup>4</sup> h<sup>-1</sup>). The volumetric flow rates are: 30 (blue), 35 (red), 40 (black), 45 (orange) and 50 (green) mL min<sup>-1</sup>. The inset shows the abrupt increase in conversion for the profiles with  $v_0 = 35$  and 40 mL min<sup>-1</sup>. (B) Global curve-fits (lines) of Eq. 4.3 to all reaction profiles truncated at  $X = 0.20$  (90 °C ≤  $T$  ≤ 142 °C). Every 10<sup>th</sup> datapoint is displayed (symbols).  $E_a$ ,  $n$ , and  $m$  were refined as global parameters; the pre-exponential factor  $A$  was refined separately for each profile.

At each volumetric flow rate, the three profiles are superposable (Fig. A4.2). Eq. 4.3 was fit globally to the data, which was truncated at  $X = 0.20$  because  $\Theta_{O_2} = b/a$ . The data were truncated at low  $X$  because the assumption that  $\Theta_b - b/a X \approx \Theta_b$  is valid at low  $X$  [19]. The activation energy is  $(91.1 \pm 2.2)$  kJ mol<sup>-1</sup>, which agrees with the value obtained from a conventional, linear Arrhenius plot analysis CO oxidation catalyzed by Pd(0)/Al<sub>2</sub>O<sub>3</sub> [19, 22, 23]. The refined reaction orders refined to  $(-1.3 \pm 0.3)$  and  $(1.0 \pm 0.2)$  for CO and O<sub>2</sub>, respectively. These values are expected for CO oxidation catalyzed by Pd(0) [21]. Thus global refinement of Eq. 4.3 yields physically meaningful reaction orders from stoichiometric profiles truncated at low  $X$ , in addition to accurately determining the activation energy.

Eq. 4.2 was used to curve-fit all the experimental profiles, after each dataset was truncated at  $X = 0.6$ . The activation energy is unchanged from the fit using Eq. 4.3,  $(92.1 \pm 2.2)$  kJ mol<sup>-1</sup>. Nearly identical curve-fit parameters were obtained when this procedure was performed with data truncated at  $X = 0.8$ . Thus, the agreement between the fit and the experimental data is very good, Fig A4.4. The value of  $E_a$  can be extracted from profiles using either Eq. 4.2 or 4.3, using variable amounts of data. If a profile is truncated at low conversion, Eq. 4.3 can always be used to extract a full set of kinetic information.

To explore the origin of the abrupt increase in activity at  $X \approx 0.9$  in more detail, the temperature ramp-down was controlled at a rate of 5 K min<sup>-1</sup>, while the conversion was monitored using double the inlet concentrations of Fig. 4.1. Fig. 4.2 shows that the change in conversion,  $\Delta X$ , is higher,  $X = 0.18$ , and occurs at a lower conversion ( $X \approx 0.72$ ) and a higher temperature (181 °C). Above this temperature, the light-off and extinction profiles are superposable. However, on the ramp-down, there is an extinction event at 173 °C, creating a

hysteresis between the light-off and the extinction profiles. Below this temperature, the light-off and extinction profiles are superposable.

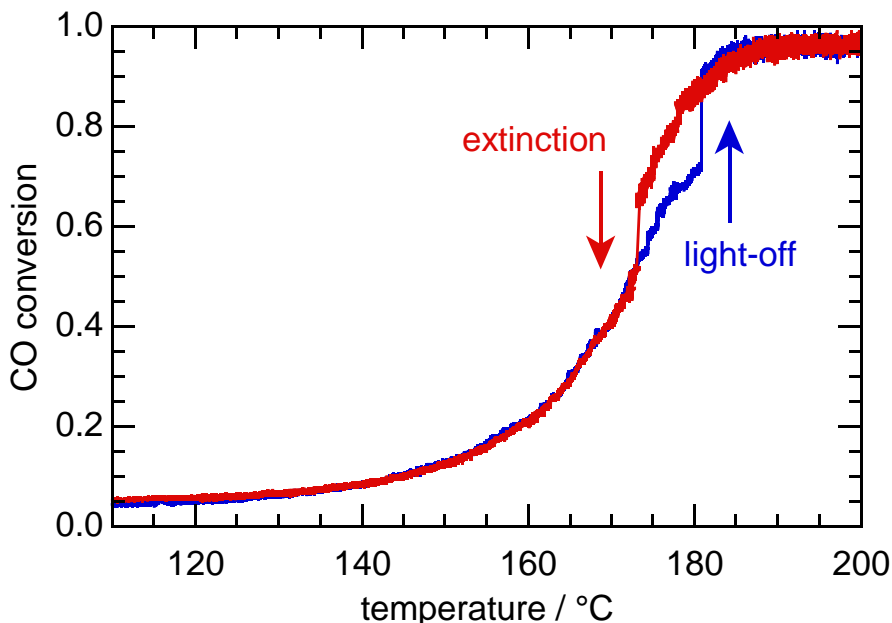


**Fig. 4.2.** Light-off and extinction observed for CO oxidation catalyzed Pd/Al<sub>2</sub>O<sub>3</sub>. Reaction profiles CO oxidation (2000 ppm CO, 1000 ppm O<sub>2</sub>, balance Ar) catalyzed by Pd/Al<sub>2</sub>O<sub>3</sub> (12 mg). Only one reaction profile is shown for light-off (blue) and extinction (red). The flow rate is  $v_0 = 50 \text{ mL min}^{-1}$  (GHSV =  $8.9 \times 10^4 \text{ h}^{-1}$ ).

The superposability of the low conversion portions of the light-off and extinction profiles suggests that, after extinction, the catalyst returns to its original state before light-off. Light-off may occur because the surface chemistry is altered, possibly by the formation of a more active surface oxide [2]. However, the shape of the profile above the jump is similar to that prior to light-off (i.e., the profile is simply displaced vertically relative to the predicted values at a given  $T$ ). Dynamic changes in the catalyst are most often only observable by variable-temperature kinetics, although no information can be obtained about

the chemistry of the catalyst. *Operando* IR and *in situ* XAS were used to investigate the chemical state of the catalyst above and below light-off to probe the changes responsible for kinetic phase transitions.

#### **4.3.2. *Operando* IR**

The causes of the abrupt changes in conversion were explored by monitoring the reaction profile using *operando* IR spectroscopy. At each temperature, the conversion was calculated from the area of the vibrational signal at  $2347\text{ cm}^{-1}$  for gas phase  $\text{CO}_2$ . The global reaction profile, Fig. 4.3, is consistent with the analogous study performed in the PBR (Fig. 4.2), full conversion is achieved in both at ca.  $190\text{ }^\circ\text{C}$ . It is important to note that the maximum conversion reached during the *operando* IR experiment is  $X = 0.75$ , due to catalyst bypass of the feed gas. Abrupt light-off was not observed due to the lower temperature resolution of IR; spectra were collected only every  $10\text{ }^\circ\text{C}$ . During extinction, the conversion decreases with  $T$  except at  $170\text{ }^\circ\text{C}$ , where the conversion rises by ca.  $X = 0.05$ . Further reduction of temperature results in decreasing conversion, and the extinction profile is superposable with the light-off profile. The increase in conversion with decreasing temperature is similar to oscillations in conversion which have been observed during kinetic extinction experiments over this catalyst [9, 17, 18] they can be hard to detect spectroscopically due to the time required to acquire spectra. IR spectra in the region of the adsorbed CO vibrations were extracted and deconvoluted to investigate the nature of the CO-Pd interactions during light-off and extinction.

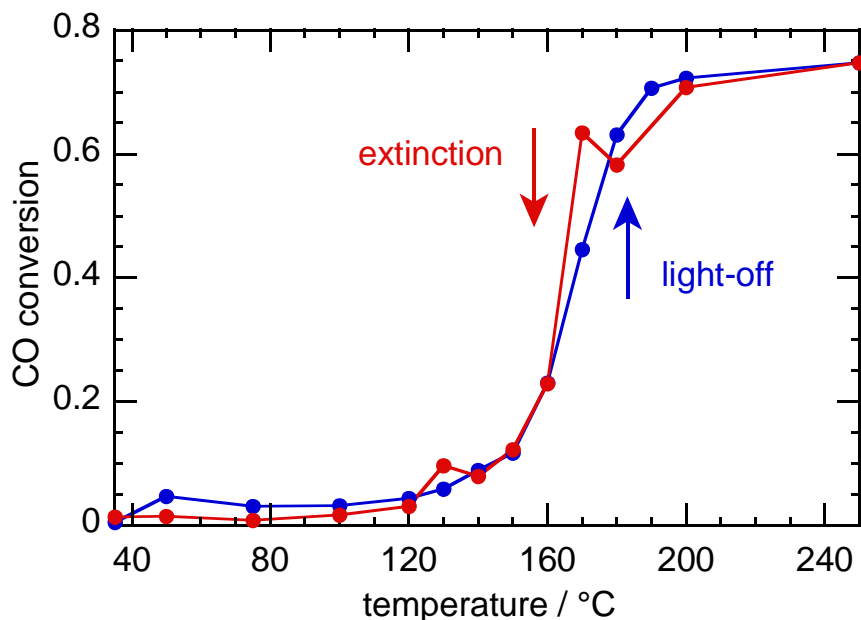


**Fig. 4.3.** CO conversion determined from *operando* IR spectroscopy. Reaction profiles for CO oxidation (2000 ppm CO, 1000 ppm O<sub>2</sub>, balance Ar,  $v_0 = 50 \text{ mL min}^{-1}$ ) catalyzed by Pd/Al<sub>2</sub>O<sub>3</sub> (25 mg). Light-off (blue) and extinction (red) profiles were recorded in a quartz IR flow cell. Prior to catalysis the catalyst was oxidized at 250 °C for 3 h under 50 mL min<sup>-1</sup> of flowing O<sub>2</sub>.

Since the catalyst was pre-oxidized completely to PdO, CO is weakly bound to atop Pd(II) sites below 75 °C, resulting in a signal at 2150 cm<sup>-1</sup>, Fig. 4.4A. At these temperatures, the conversion is negligible. The surface of the PdO nanoparticles is therefore completely reduced to Pd(0) before the onset of activity is detected in variable-temperature kinetic analysis. After the temperature is ramped to 50 °C, the IR spectrum shows adsorbed CO atop Pd(0) sites on terraces at 2066 cm<sup>-1</sup> and coordinatively-unsaturated (*cus*) edge sites at 2088 cm<sup>-1</sup> [24]. By 100 °C, CO adsorption occurs exclusively atop Pd(0) at 2066-2088 cm<sup>-1</sup>, and bridging on Pd (100) at 1976 cm<sup>-1</sup>, Pd(111) terraces at 1956 cm<sup>-1</sup>, as well as in 3-fold hollow sites at 1911 cm<sup>-1</sup> [24, 25]. A typical deconvoluted spectrum, acquired at 100 °C, is shown

in Fig. 4.5A. At high conversion,  $X > 0.7$ , the remaining adsorbed CO interacts solely with Pd at 3-fold hollow sites, which is consistent with large Pd(0) ensembles [26]. This explains why the extracted value of  $E_a$  is consistent with Pd(0), even though the catalyst state is initially PdO. Kinetic studies performed independently of *operando* characterization investigations may mistakenly attribute catalytic activity to the wrong form of the catalyst.

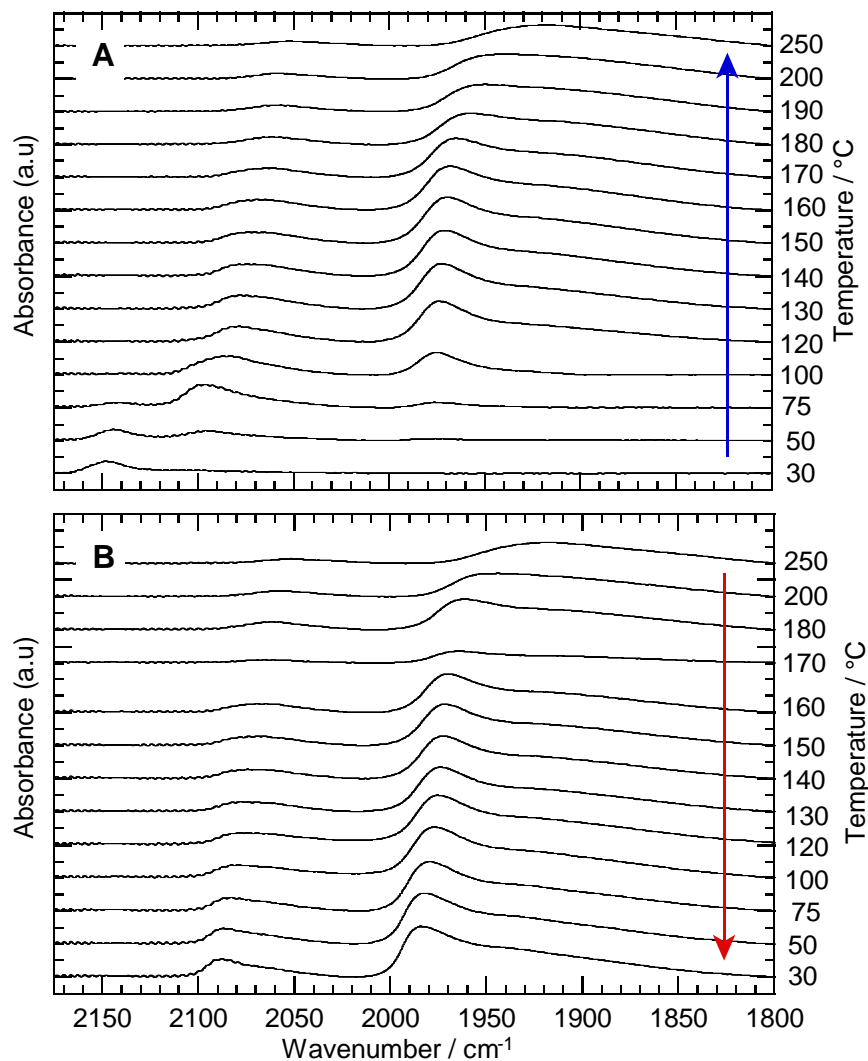


**Fig. 4.4.** *Operando* IR during light-off and extinction for CO oxidation catalyzed by Pd/Al<sub>2</sub>O<sub>3</sub>.

*Operando* IR spectra recorded during (A) light-off and (B) extinction experiments for CO oxidation (2000 ppm CO, 1000 ppm O<sub>2</sub>, balance Ar,  $v_0 = 50 \text{ mL min}^{-1}$ ) catalyzed by Pd/Al<sub>2</sub>O<sub>3</sub> (25 mg). Spectra were recorded in a quartz IR flow cell. Prior to the experiment, the catalyst was oxidized at 250 °C for 3 h under 50 mL min<sup>-1</sup> of flowing O<sub>2</sub>.

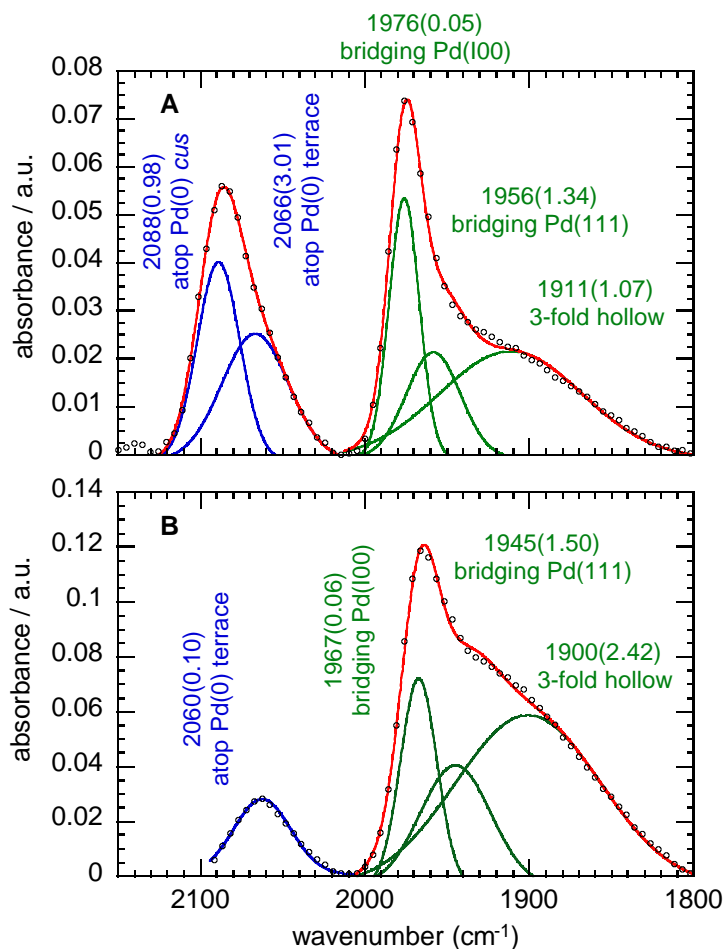


**Fig. 4.5.** Deconvoluted IR spectra in the region of CO adsorption. Deconvoluted *operando* IR spectra for CO oxidation (2000 ppm CO, 1000 ppm O<sub>2</sub>, balance Ar,  $v_0 = 50 \text{ mL min}^{-1}$ ) catalyzed by Pd/Al<sub>2</sub>O<sub>3</sub> (25 mg). Spectra (circles) were recorded in a quartz IR flow cell. Prior to catalysis the catalyst was oxidized at 250 °C for 3 h under 50 mL min<sup>-1</sup> of flowing O<sub>2</sub>. (A) Signals for spectra recorded at 100 °C during the light-off profile. (B) Signals for spectra recorded at 170 °C during the extinction profile. The overall fit (red line) was deconvoluted into atop sites (blue lines), bridging and 3-fold hollow adsorption sites (green lines). The relative intensity of each component is shown in parentheses.



During extinction, CO adsorbed atop on Pd reappears by 180 °C, Fig. 4.4B. The rise in conversion recorded at 170 °C, Fig. 4.3, correlates with a change in the IR spectra recorded at 170 °C and 160 °C. At 170 °C, there is little CO adsorbed atop on Pd(0) terraces and bridged Pd(100) sites, but these sites are populated at 160 °C. The spectrum recorded at 170 °C is deconvoluted in Fig. 4.5B. The relative amount of CO adsorbed atop Pd is diminished indicating the population of Pd(0) sites has decreased, presumably due to the formation of a surface oxide which binds CO weakly. The reduced CO poisoning causes the increase in  $X$  observed in Fig. 4.3. Despite its lower time resolution, spectroscopic evidence for a transient surface oxide was acquired for CO oxidation catalyzed by Pd/Al<sub>2</sub>O<sub>3</sub>.

#### **4.3.3. *In situ* XAS**

IR spectroscopy only probes the Pd surface, while XAS gives information about all of the Pd. Therefore understanding the results of IR and XAS reveals the subsurface chemistry of the Pd nanoparticles. *In situ* X-ray absorption spectroscopy was used to examine the Pd nanoparticles during the oxidation of CO. At 35 °C, before the onset of reaction, the X-ray absorption near edge spectroscopy (XANES) region shows the edge at 24.345 keV with a prominent white-line above the absorption edge, Fig. 4.6. These features are characteristic of Pd<sup>2+</sup>, which is consistent with the oxidative pretreatment and with the IR spectra recorded at 30 °C, Fig 4.4A. The magnitude of the  $k^2$ -weighted Fourier-transform of the X-ray absorption fine structure at 35 °C contains two major components: (1) a Pd-O single-scattering path at 1.5 Å and (2) a Pd-Pd single scattering path at 2.5 Å, Fig 4.7, typical of PdO.

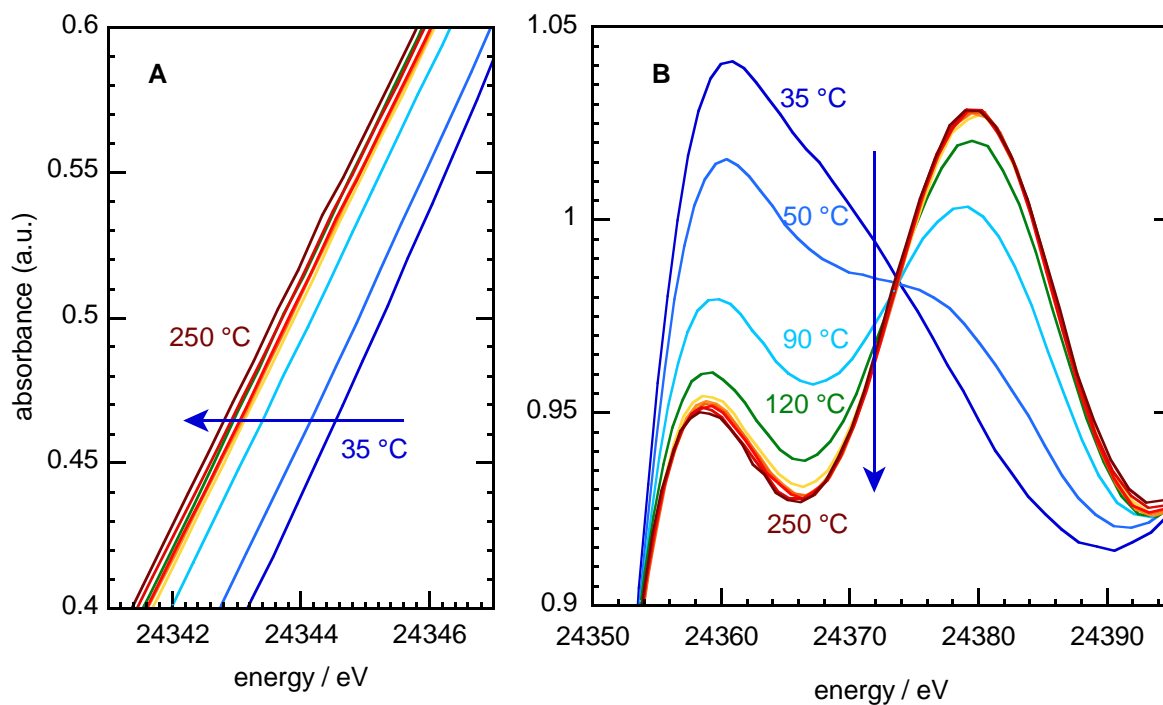


**Fig. 4.6.** *In situ* Pd K-edge XANES for CO oxidation catalyzed by Pd/Al<sub>2</sub>O<sub>3</sub>. X-ray absorption near edge spectroscopy (XANES) at the Pd-K edge for CO oxidation (2000 ppm CO, 1000 ppm O<sub>2</sub>, balance He,  $v_0 = 50 \text{ mL min}^{-1}$ ) catalyzed by Pd/Al<sub>2</sub>O<sub>3</sub> (15 mg), for the increase in temperature. (A) Edge position of XANES spectra recorded at each temperature. (B) White line and isosbestic point. Temperatures recorded: 35 (dark blue), 50 (blue), 90 (light blue), 120 (green), 140 (yellow), 150 (orange), 160 (dark orange), 170 (red), 200 (dark red), and 250 °C (brown).

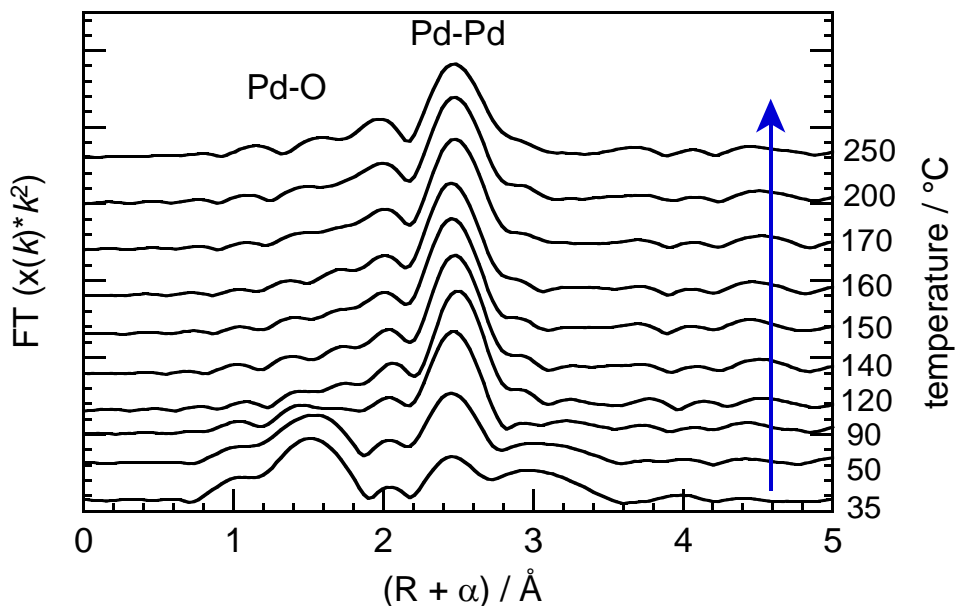


**Fig. 4.7.**  $k^2$ -weighted Fourier-transformed *in situ* XAS. *In situ* X-ray absorption spectra recorded during CO oxidation (2000 ppm CO, 1000 ppm O<sub>2</sub>, balance He,  $v_0 = 50 \text{ mL min}^{-1}$ ) catalyzed by Pd/Al<sub>2</sub>O<sub>3</sub> (15 mg). Profiles recorded isothermally after allowing the reactor to equilibrate for 0.5 h.

Fig 4.6A shows that the edge energy decreases with each temperature increment, which indicates reduction of PdO to Pd(0). From 90 - 120 °C, PdO is significantly reduced, as evidenced by the lower white line intensity. An isosbestic point is observed at 24.374 keV, signifying the clean conversion of Pd<sup>2+</sup> to Pd(0). By 140 °C, the XANES represents almost entirely Pd(0). The Pd-O path at 1.5 Å in Fig. 4.7 is entirely absent by 120 °C. Therefore PBR experiments are only collecting kinetic data for the oxidation of CO catalyzed by Pd/Al<sub>2</sub>O<sub>3</sub>, not the starting material, PdO<sub>x</sub>/Al<sub>2</sub>O<sub>3</sub>. No further changes in EXAFS were observed once the catalyst was reduced to Pd(0).

The kinetic profiles recorded with high resolution in the PBR, Fig. 4.1 – 4.2, clearly show light-off which we attribute to the formation of an active surface oxide. The *in situ*

XAS spectra recorded above 120 °C only shows Pd(0) because (1) the temperature resolution of the experiments were unable to capture the catalyst during light-off and (2) XAS is a bulk technique and is insensitive to the surface. The lack of change in the XAS above and below the light-off temperature indicates that the bulk of the catalyst is largely unchanged. *Operando* IR spectroscopy shows that CO is largely adsorbed atop on Pd(0) and not PdO above light-off suggesting that the surface of the catalyst is reduced after light-off. The increase in conversion during extinction correlates with a decrease in the signal for CO atop on Pd(0) suggesting the formation of an oxidized surface that is not poisoned by CO. The increase in activity may remain after light-off because a layer of sub-surface oxide remains which is undetectable by XAS because the nanoparticles are predominately Pd(0).

#### 4.4. Conclusions

At temperatures below 100 °C, PdO nanoparticles are reduced in flowing CO and O<sub>2</sub> to Pd(0). However the change in the state of the catalyst is not detectable via kinetic analysis, due to very low catalytic activity under these conditions ( $X < 0.01$ ). Variable-temperature kinetic analysis of the reaction profile up to  $X = 0.80$  yields an activation energy of  $(92 \pm 2) \text{ kJ mol}^{-1}$ , consistent with Pd(0) metal nanoparticles and single crystals [21-23]. Reaction profiles recorded in a PBR show a region of hysteresis between the ramp-up and ramp-down and two points of discontinuity (indicating a change in the surface chemistry). Other regions of the ramp-up and -down profiles are superposable. XAS showed that the bulk of the PdO is partially reduced upon exposure to the CO-O<sub>2</sub> atmosphere at low temperature, and completely reduced by 120 °C. The majority of the Pd remains fully reduced before and after light-off, although XAS may not detect a thin surface oxide. *In situ*

IR corroborates the change in the surface of the catalyst from PdO to Pd(0) before the onset of activity. During extinction at 170 °C, there is a sudden disappearance of signals associated with CO-Pd(0), suggesting a transient chemical state responsible for the hysteresis observed during the ramp-down in temperature. Abrupt increases in conversion are consistent with the formation of an active surface oxide that is not poisoned by CO, as evidenced by the IR spectra recorded at 170 °C during extinction. It is possible that the active surface oxide is rapidly partially reduced again to Pd(0), similar to the state of the catalyst before light-off. This explains why no CO-PdO signal is observed above light-off by IR, and why PdO is not detectable by XAS above light-off.

This study demonstrates the need to conduct thorough kinetic and spectroscopic investigations together to confidently link catalyst activity to the chemical state of the catalyst. Future, *operando* and *in situ* experiments with much higher time/temperature resolution will shed more light on dynamic changes in the catalyst.

## **Chapter 4 Acknowledgments**

D. H. C. thanks Zachary Jones for his contribution. Zachary Jones performed the IR and XAS experiments and their corresponding analysis.

## Appendix 4

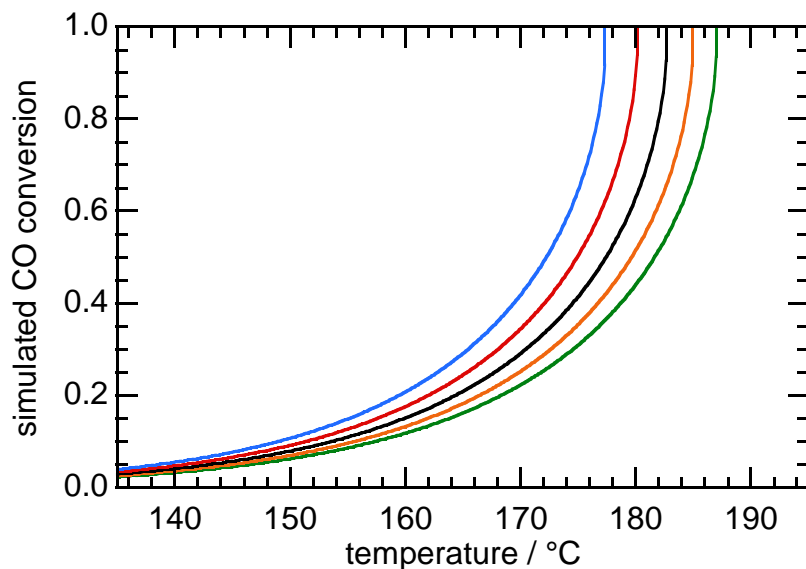


**Fig. A4.1.** Simulated reaction profiles for CO oxidation catalyzed by Pd/Al<sub>2</sub>O<sub>3</sub>. Profiles were simulated with Eq. 4.2. Parameters were fixed at:  $E_a = 92 \text{ kJ mol}^{-1}$ ,  $A = 10^5 \text{ mol CO g}_{\text{cat}}^{-1} \text{ s}^{-1}$ ,  $C_{\text{CO},0} = 0.0409 \text{ mol m}^{-3}$ ,  $\Theta_{\text{O}_2} = 1/2$ ,  $W_{\text{cat}} = 0.01 \text{ g}$ ,  $n = -1$ , and  $m = 1$ . The volumetric flow rate,  $v_0$ , was simulated for 30 (blue), 35 (red), 40 (black), 45 (orange), and 50 mL min<sup>-1</sup> (green).

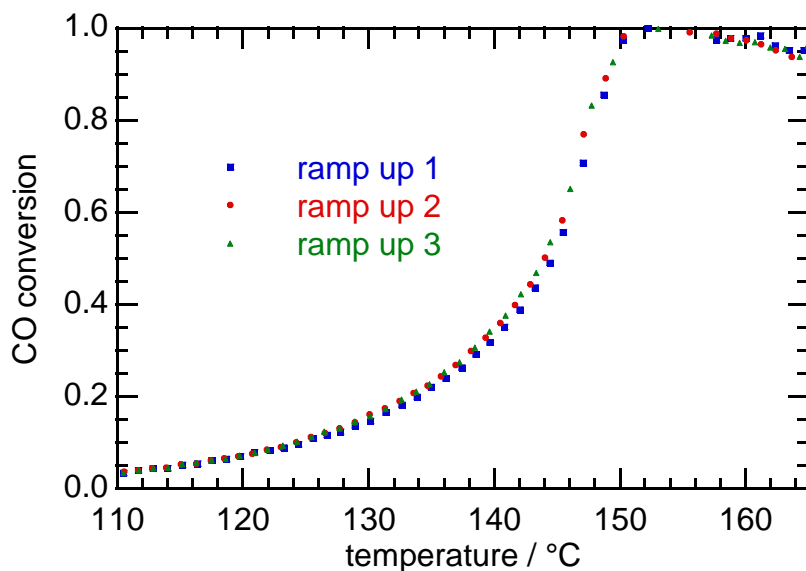


**Fig. A4.2.** Reaction profiles for CO oxidation (1000 ppm CO, 500 ppm O<sub>2</sub>, balance Ar,  $v_0 = 30 \text{ mL min}^{-1}$ ) catalyzed by Pd/Al<sub>2</sub>O<sub>3</sub> (11.8 mg) diluted in SiC (30.9 mg). Three consecutive profiles were recorded from room temperature to 200 °C. The first profile (blue squares), second profile (red circles), and the third profile (green triangles) recorded are superposable.

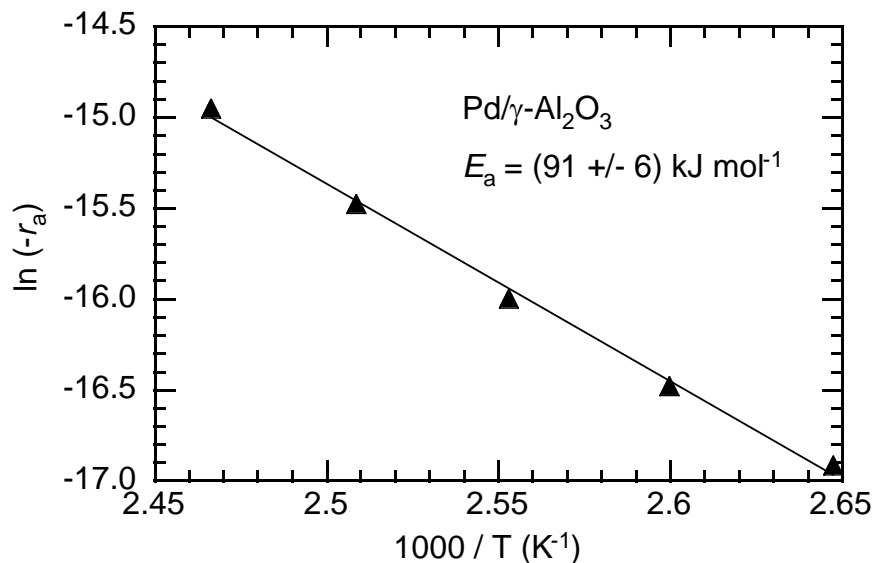


**Fig. A4.3.** Arrhenius plot for CO oxidation (1000 ppm CO, 500 ppm O<sub>2</sub>, balance Ar,  $v_0 = 50 \text{ mL min}^{-1}$ ) catalyzed by Pd/Al<sub>2</sub>O<sub>3</sub> (11.8 mg) diluted in SiC (30.9 mg). The natural log of the rate of reaction is plotted against the reactor temperature. Isothermal measurements were made for  $105^\circ\text{C} < T < 132^\circ\text{C}$  and  $0.01 < X < 0.10$ .

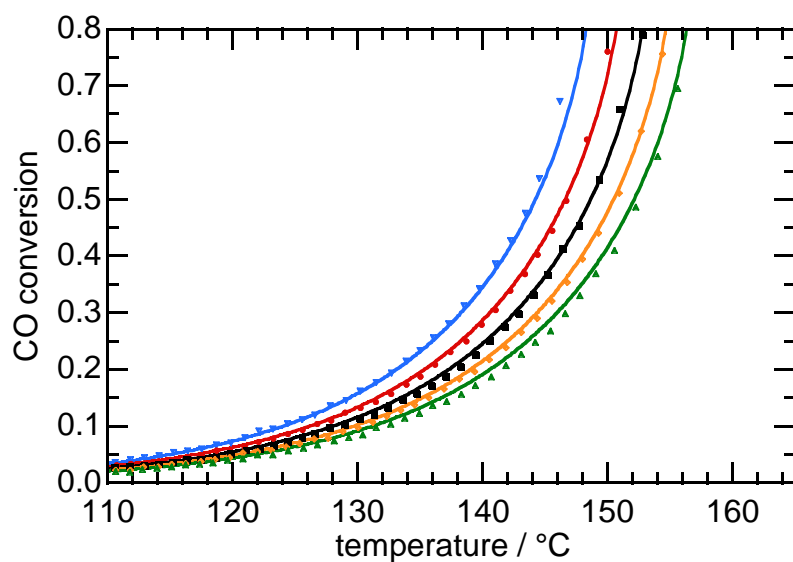


**Fig. A4.4.** Reaction profiles for CO oxidation (1000 ppm CO, 500 ppm O<sub>2</sub>, balance Ar) over Pd/Al<sub>2</sub>O<sub>3</sub> (11.8 mg) diluted in SiC (30.9 mg). Only one reaction profile (of three recorded) is shown for each flow rate (GHSV =  $3.8 - 8.9 \times 10^4 \text{ h}^{-1}$ ). The volumetric flow rates are equal to: 30 (blue), 35 (red), 40 (black), 45 (orange) and 50 (green) mL min<sup>-1</sup>. Global curve-fits (lines) of Eq. 4.2 to all reaction profiles truncated at  $X = 0.80$  ( $90^\circ\text{C} \leq T \leq 157^\circ\text{C}$ ). Every 10<sup>th</sup> datapoint is displayed (symbols).  $E_a$ ,  $n$ , and  $m$  were refined as global parameters; the pre-exponential factor  $A$  was refined separately for each profile.



## References

- [1] A.D. Allian, K. Takanabe, K.L. Fajdala, X. Hao, T.J. Truex, J. Cai, C. Buda, M. Neurock, E. Iglesia, Chemisorption of CO and mechanism of CO oxidation on supported platinum nanoclusters, *J. Am. Chem. Soc.* 133 (2011) 4498-4517.
- [2] R.C. Davis, Operando spectroscopic investigation of supported Pd and low-surface area mixed metal oxide catalysts for automotive emissions after-treatment, (Order No. 3553724) (2012) Available from ProQuest Dissertations & Theses A&I. (1314982911). Retrieved from <http://search.proquest.com/docview/1314982911?accountid=1314914522>.
- [3] A.M. Ganzler, M. Casapu, A. Boubnov, O. Muller, S. Conrad, H. Lichtenberg, R. Frahm, J.D. Grunwaldt, Operando spatially and time-resolved X-ray absorption spectroscopy and infrared thermography during oscillatory CO oxidation, *J. Catal.* 328 (2015) 216-224.
- [4] E.M.C. Alayon, J. Singh, M. Nachtegaal, M. Harfouche, J.A. van Bokhoven, On highly active partially oxidized platinum in carbon monoxide oxidation over supported platinum catalysts, *J. Catal.* 263 (2009) 228-238.
- [5] A. Boubnov, A. Ganzler, S. Conrad, M. Casapu, J.D. Grunwaldt, Oscillatory CO oxidation over Pt/Al<sub>2</sub>O<sub>3</sub> catalysts studied by in situ XAS and DRIFTS, *Top. Catal.* 56 (2013) 333-338.
- [6] A. Bourane, Oxidation of CO on a Pt/Al<sub>2</sub>O<sub>3</sub> catalyst: from the surface elementary steps to light-off tests V. Experimental and kinetic model for light-off tests in excess of O<sub>2</sub>, *J. Catal.* 222 (2004) 499-510.
- [7] P.A. Carlsson, L. Osterlund, P. Thormahlen, A. Palmqvist, E. Fridell, J. Jansson, M. Skoglundh, A transient in situ FTIR and XANES study of CO oxidation over Pt/Al<sub>2</sub>O<sub>3</sub> catalysts, *J. Catal.* 226 (2004) 422-434.
- [8] B.L.M. Hendriksen, S.C. Bobaru, J.W.M. Frenken, Bistability and oscillations in CO oxidation studied with scanning tunnelling microscopy inside a reactor, *Catal. Today* 105 (2005) 234-243.
- [9] R. Imbihl, G. Ertl, Oscillatory kinetics in heterogeneous catalysis, *Chem. Rev.* 95 (1995) 697-733.
- [10] R. Jensen, T. Andersen, A. Nierhoff, T. Pedersen, O. Hansen, S. Dahl, I. Chorkendorff, Self-sustained carbon monoxide oxidation oscillations on size-selected platinum nanoparticles at atmospheric pressure, *Phys. Chem. Chem. Phys.* 15 (2013) 2698-2702.
- [11] J. Singh, E.M.C. Alayon, M. Tromp, O.V. Safonova, P. Glatzel, M. Nachtegaal, R. Frahm, J.A. van Bokhoven, Generating highly active partially oxidized platinum during oxidation of carbon monoxide over Pt/Al<sub>2</sub>O<sub>3</sub>: in situ, time-resolved, and high-energy-resolution X-ray absorption spectroscopy, *Angew. Chem. Int. Ed.* 47 (2008) 9260-9264.
- [12] S.B. Vendelbo, C.F. Elkjaer, H. Falsig, I. Puspitasari, P. Dona, L. Mele, B. Morana, B.J. Nelissen, R. van Rijn, J.F. Creemer, P.J. Kooyman, S. Helveg, Visualization of oscillatory behaviour of Pt nanoparticles catalysing CO oxidation, *Nat Mater* 13 (2014) 884-890.
- [13] G. Ertl, P.R. Norton, J. Rustig, Kinetic oscillations in the platinum-catalyzed oxidation of CO, *Phys Rev Lett* 49 (1982) 177-180.

- [14] B.C. Sales, J.E. Turner, M.B. Maple, Oscillatory oxidation of CO over Pt, Pd and Ir catalysts: Theory, Surf. Sci. 114 (1982) 381-394.
- [15] J.E. Turner, B.C. Sales, M.B. Maple, Oscillatory oxidation of CO over a Pt catalyst, Surf. Sci. 103 (1981) 54-74.
- [16] T.H. Lindstrom, T.T. Tsotsis, Reaction rate oscillations during CO oxidation over Pt/ $\gamma$ - $\text{Al}_2\text{O}_3$  - experimental observations and mechanistic causes, Surf. Sci. 150 (1985) 487-502.
- [17] E.A. Lashina, E.M. Slavinskaya, N.A. Chumakova, O.A. Stonkus, R.V. Gulyaev, A.I. Stadnichenko, G.A. Chumakov, A.I. Boronin, G.V. Demidenko, Self-sustained oscillations in CO oxidation reaction on PdO/ $\text{Al}_2\text{O}_3$  catalyst, Chem. Eng. Sci. 83 (2012) 149-158.
- [18] E.M. Slavinskaya, O.A. Stonkus, R.V. Gulyaev, A.S. Ivanova, V.I. Zaikovskii, P.A. Kuznetsov, A.I. Boronin, Structural and chemical states of palladium in Pd/ $\text{Al}_2\text{O}_3$  catalysts under self-sustained oscillations in reaction of CO oxidation, Appl. Catal. A: Gen. 401 (2011) 83-97.
- [19] D.H. Coller, B.C. Vicente, S.L. Scott, Rapid extraction of quantitative kinetic information from non-isothermal reaction profiles, Chem. Eng. J. (2016).
- [20] B. Ravel, M. Newville, ATHENA, ARTEMIS, HEPHAESTUS: data analysis for X-ray absorption spectroscopy using IFEFFIT, Journal of synchrotron radiation 12 (2005) 537-541.
- [21] T. Engel, G. Ertl, Molecular beam investigation of catalytic oxidation of CO on Pd (111), J. Chem. Phys. 69 (1978) 1267-1281.
- [22] P.J. Berlowitz, C.H.F. Peden, D.W. Goodman, Kinetics of CO oxidation on single-crystal Pd, Pt, and Ir, J. Phys. Chem. 92 (1988) 5213-5221.
- [23] N.W. Cant, P.C. Hicks, B.S. Lennon, Steady-state oxidation of carbon monoxide over supported noble metals with particular reference to platinum, J. Catal. 54 (1978) 372-383.
- [24] H. Tiznado, S. Fuentes, F. Zaera, Infrared study of CO adsorbed on Pd/ $\text{Al}_2\text{O}_3$ - $\text{ZrO}_2$ . Effect of zirconia added by impregnation, Langmuir 20 (2004) 10490-10497.
- [25] K.I. Choi, M.A. Vannice, CO oxidation over Pd and Cu Catalysts III. Reduced  $\text{Al}_2\text{O}_3$  - supported Pd, J. Catal. 131 (1991) 1-21.
- [26] A.K. Santra, D.W. Goodman, Catalytic oxidation of CO by platinum group metals: from ultrahigh vacuum to elevated pressures, Electrochim. Acta 47 (2002) 3595-3609.

## **Chapter 5: Analysis of Variable-Temperature Reaction Profiles Impacted by Mass Transport Limitations**

### **5.1. Introduction**

#### **5.1.1. Background**

Conventional kinetic analysis of heterogeneous catalysts often suffers from long, labor-intensive experimentation and the comparison of non-informative single-point measurements that may be prone to error. Comparison of the turnover frequency (TOF) [1], temperature at which 50% conversion,  $T_{50}$ , occurs, or the rate at a specified temperature can be problematic due to abrupt changes in the activity and the difficulty comparing measurements made in different reactors under different conditions. Therefore there is a need for new methods of kinetic analysis that are amenable to the high throughput studies and provide a wealth of quantitative and qualitative information. Variable-temperature kinetic experiments, where the temperature is increased at a constant rate and the reactor is assumed to be at steady state during each  $X$  measurement, have been used to extract activation parameters from experimental conversion-temperature,  $X$ - $T$ , data with varying success [2-15]. In some cases the rate of external mass transport was included in the derivation of analytical and numerical solutions for the kinetics [4-6, 8-10]. Previously, we reported a rapid method to extract rate law information and activation parameters from variable-temperature reaction profiles ( $X$ - $T$  data) for reactions that are kinetically-limited, free from limitations and gradients in temperature, and the reaction obeys a power rate law [3]. In this paper we explore the effects of internal and external mass transport on simulated

reaction profiles for reactors free from temperature gradients, and study the effect of diffusion for CO oxidation catalyzed by Pt/Al<sub>2</sub>O<sub>3</sub>.

### 5.1.2. Kinetically-limited variable-temperature reaction profiles

Kinetically-limited reaction profiles were explored in a previous study of H<sub>2</sub>, C<sub>3</sub>H<sub>8</sub>, and CO oxidation over Pd/ $\gamma$ -Al<sub>2</sub>O<sub>3</sub> [3]. When the rate of the surface reaction is significantly slower than the rate of diffusion (either external or internal), the observed reaction rate is kinetically-controlled. Even complex Langmuir-Hinshelwood (L-H) rate laws containing many kinetic parameters can often be simplified to mass action (power) rate laws under the restricted range of experimental conditions sampled in a reaction profile. Previously, we showed that the profile can be described completely by combining such a simple power rate law (written in terms of the bulk gas phase concentrations) with the Arrhenius equation and the mass balance, as represented in the reactor design equation.

When heat transport effects are also negligible, the rate of a kinetically-limited reaction with  $j + 1$  concentration dependencies in a packed bed reactor (PBR) is given by Eq. 5.1:

$$C_{a,0}v_0 \frac{dX}{dW} = -r_a = Ae^{-\frac{E_a}{RT}} [C_{a,0}(1-X)]^n \prod_i [C_{a,0}(\Theta_i - X b_i/a)]^{m_i} \quad (5.1)$$

$A$  is the Arrhenius pre-exponential factor,  $E_a$  is the activation energy,  $C_{a,0}$  is the inlet concentration of the limiting reactant **a**,  $v_0$  is the inlet volumetric flow rate,  $\Theta_i$  is the ratio of the inlet concentrations of reactants **i** and **a**,  $a$  and  $b_i$  are the stoichiometric coefficients of **a** and **i**, and  $n$  and  $m_i$  are the reaction orders for species **a** and **i**, respectively. Variable-temperature profiles can be analyzed by non-linear curve-fitting of Eq. 5.1, determining simultaneously the reaction orders and the activation parameters.

Commonly, the rate law depends on the concentrations of just one or two reactants. Analytical solutions are possible for any reaction orders  $n$  and  $m$  provided  $\Theta_b = b/a$ , Eq. 5.2. Here, the inlet concentration  $C_{a,0,\text{ref}}$  and  $\tau_{\text{ref}} = W/v_0$  ( $\text{g}_{\text{cat}} \text{ s m}^{-3}$ , the residence time or space-time) are calculated at an arbitrary reference temperature,  $T_{\text{ref}}$ , and their temperature-dependent values are calculated from the ideal gas law,  $C_a = P/RT$ , where  $P$  is the pressure and  $R$  is the gas constant. If  $\Theta_b \neq b/a$ , the approximate solution in Eq. 5.3 is valid for all conversions provided  $\Theta_b \gg b/a$ . The solution is valid up to moderately high values of conversion even when  $\Theta_b$  is not large.

$$X = 1 - \left[ 1 + (n + m - 1) \left( \frac{T_{\text{ref}}}{T} \right)^{n+m} \left( \frac{b}{a} \right)^m C_{a,0,\text{ref}}^{n+m-1} \tau_{\text{ref}} A e^{-\frac{E_a}{RT}} \right]^{\frac{1}{1-n-m}} \quad (5.2)$$

$$X = 1 - \left[ 1 + (n - 1) \tau_{\text{ref}} C_{a,0,\text{ref}}^{n+m-1} \left( \frac{T_{\text{ref}}}{T} \right)^{n+m} \Theta_b^m A e^{-\frac{E_a}{RT}} \right]^{\frac{1}{1-n}} \quad (5.3)$$

If the reaction orders are known, they can be fixed and analytical solutions for  $X$  can be solved. For example,  $\text{H}_2$  oxidation catalyzed by supported noble metal nanoparticles in an  $\text{O}_2$ -rich environment obeys a simple, first-order rate law [16, 17]. The appropriate simplified form of Eq. 5.1, with  $n = 1$  and  $m = 0$ , is shown in Eq. 5.4.

$$X = 1 - e^{\left[ -\tau_{\text{ref}} \left( \frac{T_{\text{ref}}}{T} \right) A e^{-\frac{E_a}{RT}} \right]} \quad (5.4)$$

$\text{CO}$  oxidation over platinum group metals such as  $\text{Pd}$  and  $\text{Pt}$  on alumina are known to obey a Langmuir-Hinshelwood reaction mechanism, which simplifies to a simple power rate law under most relevant reaction conditions in which the reaction orders are -1 and +1 with

respect to CO and O<sub>2</sub>, respectively [18, 19]. The analytical solution to Eq. 5.3 for CO-lean oxidation (CO is the limiting reactant) can be reduced to two variables:  $E_a$  and  $A$ , Eq. 5.5 [3].

$$X = 1 - \left[ 1 - 2\tau_{\text{ref}} C_{\text{CO},0,\text{ref}}^{-1} \Theta_{\text{O}_2} A e^{-\frac{E_a}{RT}} \right]^{\frac{1}{2}} \quad (5.5)$$

### 5.1.3. Mass Transport Effects on Variable-temperature Reaction Profiles

When the rate of mass transport (either external or internal to the catalyst pellet) is comparable to the rate of reaction, it influences the shape and position of the reaction profile. Effects of external mass transport (also referred to as interparticle diffusion) are most commonly manifested at high conversions, where the gradient between bulk and surface concentration is appreciable. The rate of external mass transport ( $-r_{\text{ext}}$ , in mol g<sub>cat</sub><sup>-1</sup> s<sup>-1</sup>) depends on the concentration gradient that exists between the bulk gas phase and the surface, Eq. 5.6:

$$-r_{\text{ext}} = k_c S (C_a - C_{a,s}) \quad (5.6)$$

where  $C_a$  and  $C_{a,s}$  are the concentrations of the limiting reactant **a** in the bulk gas phase and at the external surface of the catalyst particle, respectively,  $k_c$  is the mass transfer coefficient of **a**, and  $S$  is the catalyst surface area per g catalyst.

The Mears' Criterion, Eq. 5.7, is a theoretical approximation to test if a reaction is kinetically-limited or external mass transport-limited [20].

$$\frac{-r_a R_p n}{k_c C_{a,bulk}} < 0.15 \quad (5.7)$$

For spherical catalyst particles of radius  $R_p$  for a reaction with order  $n$  and a gas phase concentration of  $C_{a,bulk}$ , the reaction is kinetically controlled if the Mears' Criterion is less than 0.15.

Effects of Internal mass transport (or intraparticle, diffusion) may be important in describing the kinetics for highly porous catalysts, for which the active sites are predominantly located on internal surfaces which dominates the total surface area of the catalyst. For non-porous catalysts, intraparticle diffusion does not affect the rate. Resistance to internal diffusion is represented by the internal effectiveness factor,  $\eta$ , Eq. 5.8.

$$-r_{obs} = \eta(-r_{a,s}) = \eta k C_{a,s}^n \quad (5.8)$$

#### 5.1.4. CO oxidation light-off catalyzed by Pt

CO oxidation catalyzed by supported Pt nanoparticles has been studied extensively particularly because of the importance of the reaction to automobile exhaust catalysts [21]. Pt for CO oxidation remains an interesting research area because oscillations in conversion are observable during single-temperature and variable-temperature kinetic experiments as well as the occurrence of a hysteresis observed in reaction profiles during temperature ramp up and ramp down (extinction) experiments. Much of the early work in this field was performed on Pt single crystals and wires under UHV conditions [22-26]. Reaction profiles for CO oxidation on Pt nanoparticles display an abrupt and discontinuous increase in

reactivity over a temperature range of less than 1 K. This behavior will hereafter be referred to as light-off. Reaction oscillations, hysteresis, and light-off for CO oxidation catalyzed by Pt nanoparticles supported on alumina was studied by various *in situ* and *operando* techniques recently, although no clear consensus exists to explain these observations at atmospheric pressure. By *in situ* infrared spectroscopy (IR) it was demonstrated that light-off coincides with a dramatic decrease in observable  $C_{\text{CO},s}$  adsorbed to metallic Pt atop sites [27-29]. Oxidation of Pt(0) to Pt oxide occurs concurrently with light-off and the disappearance of linearly bound CO on Pt(0), as determined by *in situ* X-ray absorption spectroscopy [27, 30-33]. While the phenomenon has garnered wide attention, both recent and old, the origin remains a topic of debate. Proposed explanations include hysteresis between light-off and extinction, and sustained oscillations in conversion, include (1) facile transformation of surface Pt(0) into a super-active oxide layer that is not poisoned by adsorbed CO and can be readily transformed back to Pt(0) [28, 30, 31, 33, 34], (2) ignition caused by hot spots that occur when  $C_{\text{CO},s}$  declines to a value that no longer poisons the catalyst [32, 35], and (3) surface reconstruction of metallic Pt nanoparticles [36].

### 5.1.5. Objectives

Here we explore the analysis of reaction profiles in which mass transport makes a significant contribution to the observed rate of reaction. A method is demonstrated to observe the transition from reaction-limited to mass transport-limited conditions for simulated profiles, and to extract reliable kinetic parameters free from mass transport effects. The catalytic oxidation of CO over Pt/ $\gamma$ -Al<sub>2</sub>O<sub>3</sub> is studied to observe the role particle size and flow rate (which effect internal and external diffusion) have on light-off, which has not been observed before.



## 5.2 Experimental Methods

### 5.2.1. Materials

1.0 wt% Pt supported on  $\gamma$ -Al<sub>2</sub>O<sub>3</sub> (Pt/Al<sub>2</sub>O<sub>3</sub>) was purchased from a commercial supplier (Sigma-Aldrich, product 205966, surface area  $(206 \pm 1) \text{ m}^2 \text{ g}^{-1}$ ; Pt dispersion 0.25 [37]). The Pt nanoparticles have an average size of  $(4.3 \pm 1.7) \text{ nm}$  as determined by TEM [38]. The as-received powder was pressed into pellets and ground with a mortar and pestle so that the catalyst support could be separated into known particle size distributions. The resulting powder was placed in a sieve set with sizes of 20, 40, 60, 80, and 100 mesh sizes. Particles were retrieved such that the largest particle diameters were between 20 and 40 mesh ( $0.43 < 2R_p < 0.85 \text{ mm}$ ) and the smallest particles were between 80 and 100 mesh size ( $0.15 \text{ mm} < 2R_p < 0.18 \text{ mm}$ ).

The high purity reaction gasses were supplied by Praxair: Ar (99.99 %), O<sub>2</sub> (5000 ppm in Ar, 99.99 %, and pure O<sub>2</sub>, 99.99% purity), CO (5005 ppm in Ar, 99.99 %), and CO<sub>2</sub> (5000 ppm in Ar, 99.99 %).

### 5.2.2. Experimental Methods

Oxidation of CO (1000 ppm) was performed with either a 200-fold excess of O<sub>2</sub> ( $\Theta_{\text{O}_2} = C_{\text{O}_2,0}/C_{\text{CO}} = 100$ , balance Ar) or an eight-fold excess of O<sub>2</sub> ( $\Theta_{\text{O}_2} = C_{\text{O}_2,0}/C_{\text{CO}} = 4$ , balance Ar). Variable-temperature reaction profiles were recorded in a CATLAB micro-reactor (Hidden Analytical), containing 12 mg catalyst diluted 3:1 w/w with SiC as previously described [3], to minimize formation of hot spots. The reactor temperature was increased at a constant rate of  $5 \text{ K min}^{-1}$ . Calculation of the Mears' heat criterion and empirical

investigations showed the reactor was isothermal for CO oxidation catalyzed by Pd/Al<sub>2</sub>O<sub>3</sub> [3]. Therefore it was assumed no temperature gradients exist in this study because the only difference is Pt is used instead of Pd. A single temperature measured by a thermocouple (Omega KQXL, 0.05 s response time) in contact with the catalyst at the front end of the catalyst bed was used to describe the reactor temperature. An online secondary electron multiplier (SEM) mass spectrometer was used to monitor the signal for CO<sub>2</sub> ( $m/z = 44$ ) at the reactor outlet. Flow rates were varied from 25 to 100 mL min<sup>-1</sup>. Prior to recording the first of three consecutive reaction profiles, the catalyst was pre-conditioned for 3 h in the desired reaction atmosphere ( $v_0 = 50$  mL min<sup>-1</sup>) at a temperature for which the CO conversion  $X > 0.95$ . Conversion was calculated from the intensity of the  $m/z$  signal for CO<sub>2</sub> divided by the signal intensity for calibration gas (CO<sub>2</sub>) measured at the same flow rate and theoretical maximum yield (1000 ppm CO<sub>2</sub>).

### 5.2.3. Simulation of Variable-Temperature Reaction Profiles

Simulated reaction profiles were calculated both analytically and numerically (described in section 5.3) using Mathematica (Wolfram) and selected values of  $k_c$ ,  $\eta$ , and  $\tau$  that demonstrate kinetic- and transport-limited profiles. Profiles corresponding to a first-order rate law were simulated using arbitrary kinetic parameters. Profiles for CO oxidation were simulated for Pt/Al<sub>2</sub>O<sub>3</sub> using kinetic parameters from this work.

### 5.3. Results

#### 5.3.1. Analytical description for the impact of mass transport on variable-temperature reaction profiles

The mass transfer coefficient for arbitrary reaction conditions,  $k_{c,\text{ref}}$ , was calculated at the reference temperature  $T_{\text{ref}}$ , and used to determine its temperature-dependent value  $k_c(T)$  (see Appendix for sample calculation). Since  $k_c(T)$  is proportional to  $D_{12}^{2/3}$  ( $D_{12}$  is the diffusivity of the reactant),  $U^{1/2}$  ( $U$  is the linear velocity of the feed gas), and  $\nu^{-1/6}$  ( $\nu$  is the kinematic viscosity of the reactant gas), and since  $D_{12}$ ,  $U$  and  $\nu$  vary with temperature as  $T^{7/4}$ ,  $T$  and  $T^{3/2}$ , respectively [39], the overall temperature dependence of  $k_c$  is that given in Eq. 5.9:

$$-r_{\text{ext}} = k_{c,\text{ref}} \left( \frac{T}{T_{\text{ref}}} \right)^{17/12} (C_a - C_{a,s}) \quad (5.9)$$

First, we consider a reaction that obeys a simple first-order rate law whose rate is impacted by external and/or internal mass transport. At steady-state, the mass balance for the limiting reactant **a** requires that the rate of external mass transport be equal to the rate of reaction inside the pores, Eq. 5.10, resulting in the expression for  $C_{a,s}$  shown in Eq. 5.11. After integration, this equation can be solved explicitly for conversion, Eq. 5.12, making use of the temperature-independent reference values for  $k_c$  and  $\tau$  as described above.

$$k_c S_a (C_a - C_{a,s}) = \eta k C_{a,s} \quad (5.10)$$

$$C_{a,0} v_0 \frac{dX}{dW} = \eta k C_{a,s} = \eta k \frac{C_a k_c S_a}{\eta k + k_c S_a} = \eta k \frac{C_{a,0}(1-X)k_c S_a}{\eta k + k_c S_a} \quad (5.11)$$

$$X = 1 - \exp \left( - \frac{\eta k S_a k_{c,\text{ref}} T_{\text{ref}} \left( \frac{T}{T_{\text{ref}}} \right)^{5/12}}{\eta k + S_a k_{c,\text{ref}} \left( \frac{T}{T_{\text{ref}}} \right)^{17/12}} \right) \quad (5.12)$$

For a zeroth-order reaction (or a reaction with opposing reaction orders, such as CO oxidation), the corresponding expression for conversion is equivalent to the kinetically-limited case multiplied by the internal effectiveness factor, Eq. 5.13. In other words, the rates of zeroth-order reactions can never be limited by the rate of external mass transfer, as predicted by Mears' Criterion for mass transport [20].

$$X = \frac{\eta k \tau}{C_{a,0}} \quad (5.13)$$

A full Langmuir-Hinshelwood rate expression may simplify to a pseudo-zeroth-order power law for low to moderate values of  $X$ , but at high conversion the reaction orders will change with coverage and/or absorption coefficients, making mass transfer limitations relevant.

### 5.3.2. Numerical analysis

For rate laws represented by forms other than first- and pseudo-zeroth-order power laws, there is no analytical expression for the variable-temperature reaction profile. However, numerical methods can be used to simulate and fit reaction profiles. The rate of reaction for the simplified L-H mechanism for CO oxidation in excess oxygen contains two surface concentrations, therefore the rate of external mass transport must be considered for CO and O<sub>2</sub>. The couple equations must be solved for both surface concentrations, Eq. 5.14 – 5.15.

$$k_{c,CO} S_a (C_{CO}(1 - X) - C_{CO,s}) = \frac{\eta k C_{O_2,s}}{C_{CO,s}} \quad (5.14)$$

$$k_{c,O_2} S_a (C_{O_2}(1 - X) - C_{O_2,s}) = \frac{2\eta k C_{O_2,s}}{C_{CO,s}} \quad (5.15)$$

Eq. 5.14 is written in terms of the rate with respect to carbon monoxide. Eq. 5.15 is written in terms of oxygen. The factor of 2 in Eq. 5.15 is a consequence of the reaction stoichiometry ( $-r_{\text{CO}} = -r_{\text{O}_2} / 2$ ). The solution for the surface concentrations is cubic, therefore three values of  $C_{\text{CO},s}$  are possible, although they are not all necessarily physically meaningful. Sudden discontinuities during light-off (ramp-up) and extinction (ramp-down) have been attributed to multiple steady-states for CO oxidation over Pt catalysts [5, 22]. Discontinuities (sudden increases or decreases in conversion) and hysteresis between light-off and extinction may also be caused by changes in the chemistry of the catalyst that change the rate law, referred to as the bistability of the L-H mechanism [26, 40].

### **5.3.3. Effect of external mass transport limitations on a simulated first-order reaction**

Variable-temperature reaction profiles were simulated for a first-order reaction with and without external mass transport limitations, using Eq. 5.12 and 5.4, and three different values of  $k_c$ . The activation parameters were chosen to be  $E_a = 100 \text{ kJ mol}^{-1}$  and  $A = 10^8 \text{ m}^3 \text{ s}^{-1} \text{ g}_{\text{cat}}^{-1}$ . The residence time and concentration were chosen to be similar to our typical experimental conditions:  $\tau = 15\,000 \text{ g}_{\text{cat}} \text{ s m}^{-3}$ , and  $C_{a,0} = 0.0409 \text{ mol m}^{-3}$  (1000 ppm). The gas properties were estimated for argon at 298 K (see Appendix). A typical value of  $k_c$  is  $5 \times 10^{-2} \text{ m s}^{-1}$ , corresponding to a Mears' Criterion value of  $1 \times 10^{-3}$  at  $X = 0.1$  ( $T = 128 \text{ }^\circ\text{C}$ ), which indicates that the reaction is kinetically controlled.

A profile simulated without mass transport effects, Eq. 5.4, and profiles for three values of  $k_c$  were simulated, Fig. 5.1. The kinetically-controlled profile and Eq. 5.12 with  $k_c = 0.05 \text{ m s}^{-1}$  are superposable, confirming that this value of  $k_c$  gives a kinetically-limited

profile. Therefore only Eq. 5.12 was plotted for clarity. Fig. 5.1 shows that the reaction profiles are nearly superposable for all values of  $k_c$  at low conversion (below  $X \sim 0.1$ ). For  $k_c = 1 \times 10^{-5} \text{ m s}^{-1}$ , Mears' Criterion at  $X = 0.1$  is 10. This is almost two orders of magnitude greater than the cutoff (0.15), indicating that external mass transport influences the reaction rate. The influence of external mass transport in this case is minimal. However the increase in rate with temperature at high conversion is slower than in the kinetically-limited case, requiring slightly higher temperatures to reach the same non-differential conversions. When  $k_c = 1 \times 10^{-6} \text{ m s}^{-1}$ , Mears' Criterion at  $X = 0.1$  is 100, meaning the reaction rate is strongly influenced by external mass transport. The corresponding profile deviates significantly from the kinetically-limited case when  $X > 0.1$ , and the conversion never reaches 1.0 because the reactants cannot diffuse to the surface before they are carried out of the reactor zone.

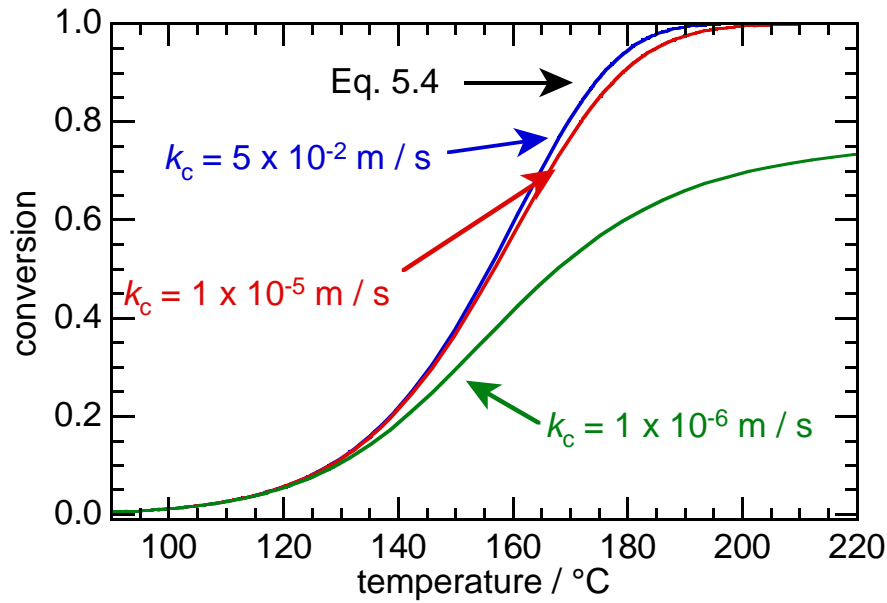


**Fig. 5.1.** Simulated reaction profiles for a first-order rate law in an isothermal packed-bed reactor, influenced by external mass transport.

Simulated reaction profiles, obtained using Eq. 5.12 to include the effect of external mass transport limitations. The reaction parameters were set to values of:  $A = 10^8 \text{ m}^3 \text{ s}^{-1} \text{ g}_{\text{cat}}^{-1}$ ,  $E_a = 100 \text{ kJ mol}^{-1}$ ,  $\tau_{\text{ref}} = 15\,000 \text{ g}_{\text{cat}} \text{ s m}^3$ ,  $C_{a,0} = 0.0409 \text{ mol m}^{-3}$ ,  $S_a = 76 \text{ m}^2 \text{ g}^{-1}$ , and  $T_{\text{ref}} = 298 \text{ K}$ . The value of  $k_{c,\text{ref}}$  was estimated for Ar to be  $0.05 \text{ m s}^{-1}$  at 298 K. The profile with  $k_{c,\text{ref}} = 0.05 \text{ m s}^{-1}$  is superposable with the profile simulated using Eq. 5.4.

#### 5.3.4. Effect of internal mass transport limitations on first-order rate laws

Reaction profiles were also simulated using Eq. 5.12, to investigate the effects of increasing resistance to internal mass transport with (Fig. 5.2B) and without (Fig. 5.2A) external mass transport limitations. In Eq. 5.12, the internal effectiveness factor appears as the product with the pre exponential factor and residence time. Decreasing the value of either  $A$  or  $\tau$  causes the reaction profile to shift to higher temperatures, Fig. 5.2. Unlike the external transport-limited profiles in Fig. 5.1, the internal transport-limited reaction profiles in Fig. 5.2A are not superposable at low conversion. Profiles that are influenced by internal diffusion limitations are also not superposable with the kinetically-limited profile. Physically, the increased barrier to internal diffusion into the pores results in a decrease in the effective number of active sites because the reactants cannot diffuse into the pores. This results in an apparent decrease in the observed rate, compared to a catalyst in which all active sites are accessible to the reactants.



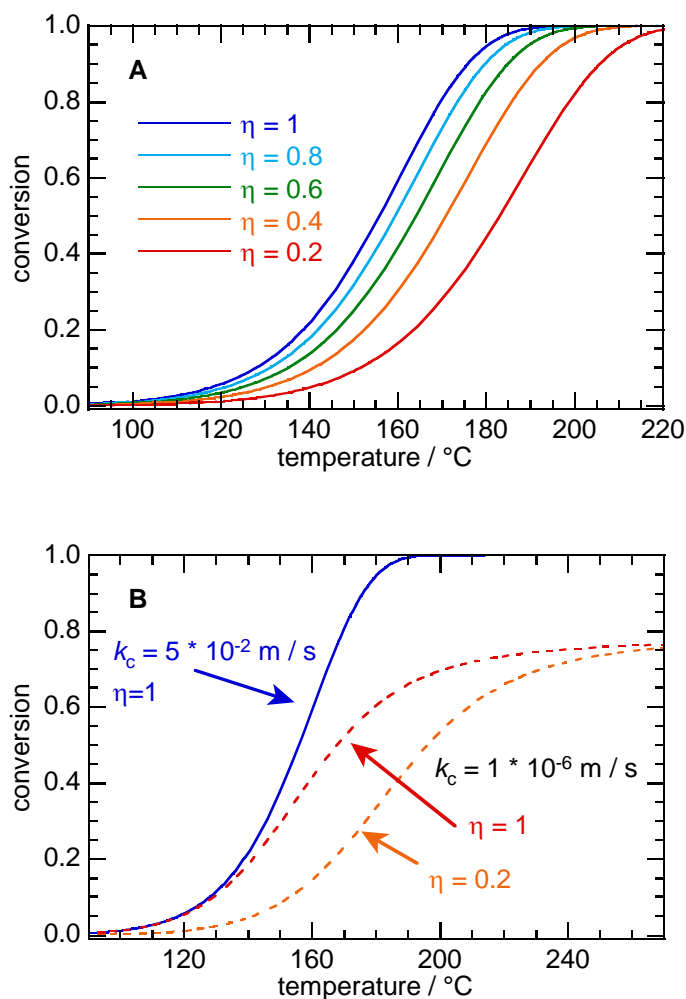


**Fig. 5.2.** Simulated reaction profiles for first-order rate laws under the influence of internal and/or external mass transport limitations.

Simulated reaction profiles, obtained using Eq. 5.12 to include the effect of internal and external mass transport limitations. The reaction parameters were set to values of:  $A = 10^8 \text{ m}^3 \text{ s}^{-1} \text{ g}_{\text{cat}}^{-1}$ ,  $E_a = 100 \text{ kJ mol}^{-1}$ ,  $\tau_{\text{ref}} = 15\,000 \text{ g}_{\text{cat}} \text{ s m}^3$ ,  $C_{a,0} = 0.0409 \text{ mol m}^{-3}$ ,  $S_a = 76 \text{ m}^2 \text{ g}^{-1}$ , and  $T_{\text{ref}} = 298 \text{ K}$ . The value of  $k_{c,\text{ref}}$  was estimated for Ar at 298 K to be  $0.05 \text{ m s}^{-1}$ . The profile with  $k_{c,\text{ref}} = 0.05 \text{ m s}^{-1}$  corresponds to the kinetically-limited case. (A) Reaction profiles with  $k_{c,\text{ref}} = 0.05 \text{ m s}^{-1}$  (at 25 °C), and  $\eta$  varied from 1.0 to 0.2. (B) External mass transfer-limited reaction profiles with  $k_{c,\text{ref}} = 1 \times 10^{-6} \text{ m s}^{-1}$  (at 25 °C), with  $\eta$  equal to 1 and 0.2.

### 5.3.5. Simulated reaction profiles for CO oxidation under the influence of mass transport

Reaction profiles were simulated using the surface concentrations of the reactants calculated using Eq. 5.14 – 5.15 to simulate the behavior of internal and external mass transport-limited reaction profiles, Fig 5.3. Profiles were simulated using estimated kinetic parameters for CO oxidation catalyzed by Pt/Al<sub>2</sub>O<sub>3</sub> (see below). Under the reaction conditions used in this study, the estimated value of  $k_{c,CO}$  is  $7.4 \times 10^{-2} \text{ m s}^{-1}$  for  $v_0 = 25 \text{ mL min}^{-1}$  at  $120 \text{ }^\circ\text{C}$ , and the reaction is kinetically-limited according to Mears' Criterion. In order to simulate external mass transport, values of  $k_c$  for CO and O<sub>2</sub> were both fixed to  $1 \times 10^{-6} \text{ m s}^{-1}$ . At low conversion, the external mass transport-limited profile is superposable with the kinetically-limited profile, similar to Fig. 5.1. Profiles under extreme external mass transport limitations do not reach  $X = 1$ . Instead, the profile approaches a maximum conversion asymptotically. The profile is continuous for all temperatures, and takes on a sigmoidal shape because the external diffusion equation is first-order in concentration. The profile impacted by internal diffusion limitations is translated to higher temperatures, but otherwise is similar in shape to the kinetically-limited profile. The internal effectiveness factor effectively decreases the residence time (by decreasing the number of active sites,  $W$ , Eq. 5.5) causing the profile to reach equivalent conversions at higher temperatures.

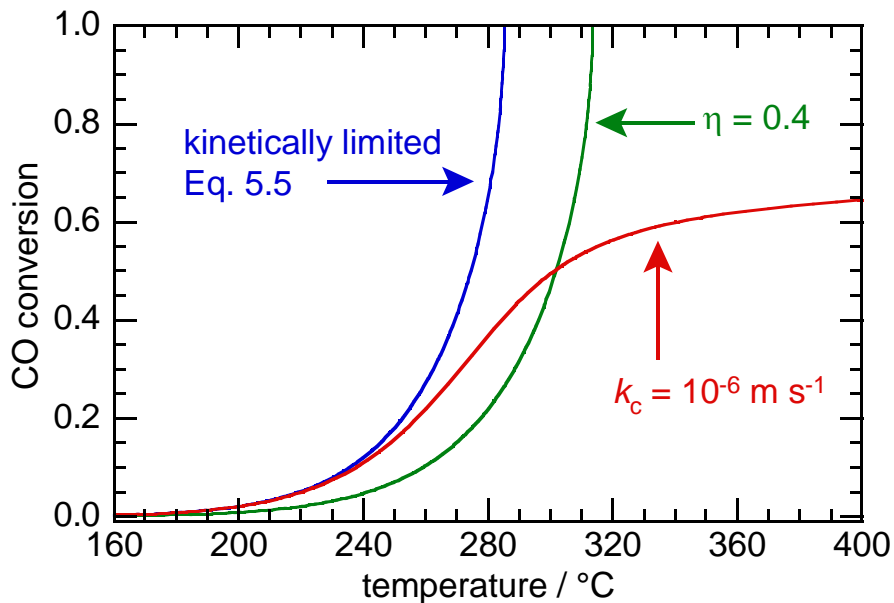


**Fig. 5.3.** Simulated profiles for CO oxidation catalyzed by Pt/Al<sub>2</sub>O<sub>3</sub>, showing the effects of internal and external mass transport limitations.

Simulated reaction profiles, obtained using Eq. 5.5 and 5.14 – 5.15 with Eq. 5.1. The reaction parameters were set to values of:  $A = 1400 \text{ mol CO s}^{-1} \text{ g}_{\text{cat}}^{-1}$ ,  $E_a = 88 \text{ kJ mol}^{-1}$ ,  $\tau_{\text{ref}} = 7200 \text{ g}_{\text{cat}} \text{ s m}^3$ ,  $C_{\text{CO},0} = 0.0409 \text{ mol m}^{-3}$ ,  $C_{\text{O}_2,0} = 0.164 \text{ mol m}^{-3}$ ,  $S_a = 76 \text{ m}^2 \text{ g}^{-1}$ , and  $T_{\text{ref}} = 298 \text{ K}$ . Eq. 5.5 was simulated for the kinetically-controlled case (blue), and for  $\eta = 0.4$  (green). Eq. 5.14 – 5.15 was solved for  $k_{\text{c,CO}} = k_{\text{c,O}_2} = 1 \times 10^{-6} \text{ m s}^{-1}$  (red) and the values for surface concentration were substituted into Eq. 1 to simulate an external mass transport-limited profile.

External mass transport-limited profiles, were simulated with Eq. 5.1 using solutions for the surface concentrations obtained from solving Eq. 5.14 – 5.15. The effect of volumetric flow rate was investigated by varying the values of 100, 50, and 25 mL min<sup>-1</sup>. The corresponding mass transfer coefficients for CO at 120 °C, are 0.17, 0.11, and 0.074 m s<sup>-1</sup>, respectively. The value of  $k_c$  for the profiles with  $v_0 = 50$  and 100 mL min<sup>-1</sup> are 1.5 and 2.2 times greater than  $k_c$  at 25 mL min<sup>-1</sup>, respectively. The large values of  $k_c$  result in kinetically-limited profiles that only show the effects of  $\tau$ . The profiles were therefore simulated with smaller values of  $k_c$  to make external mass transport effects visible:  $k_{\text{c,CO}} =$

$k_{c,O2} = 1 \times 10^{-4} \text{ m s}^{-1}$  for  $v_0 = 25 \text{ mL min}^{-1}$ , with values of  $k_c$  for  $v_0 = 50$  and  $100 \text{ mL min}^{-1}$  were 1.5 and 2.2 x greater, respectively. The resulting profiles in Fig. 5.4 are continuous for all  $T$ . The profiles appear sigmoidal near maximum conversion ( $X_{\max}$ ) because the external mass transport rate equation, Eq. 5.9, is first-order in concentration. The inset to Fig. 5.4 shows that profiles simulated with larger volumetric flow rates and mass transfer coefficients plateau at lower values of  $X_{\max}$ , because reactants are more likely to flow out of the reactor without interacting with the catalyst. In addition, Mears' Criterion for external mass transport increases with flow rate (Mears' Criterion  $\propto -r_a / k_c \propto v_0^{0.5}$ ). The increased impact of external mass transport limitations also explains the decrease in  $X_{\max}$ .

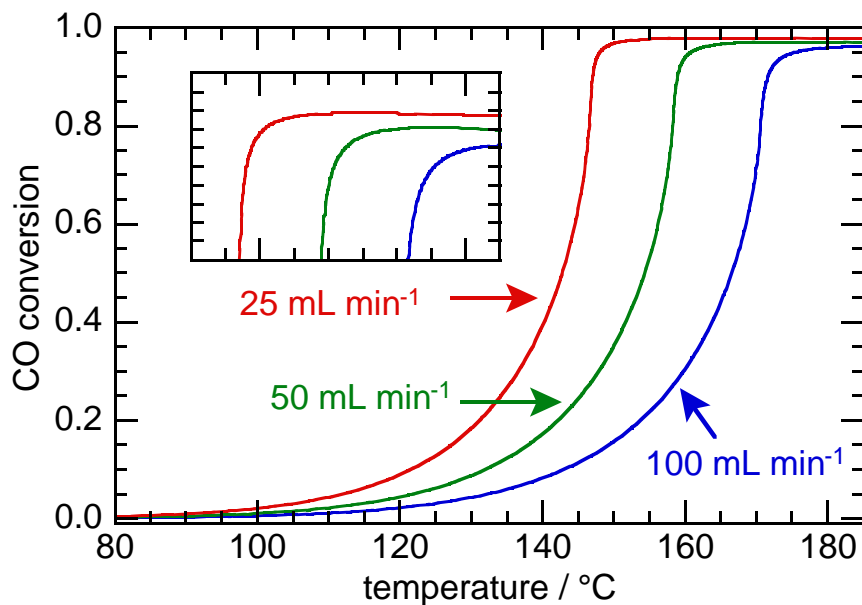


**Fig. 5.4.** Simulated reaction profiles for CO oxidation catalyzed by Pt/Al<sub>2</sub>O<sub>3</sub> for 3 volumetric flow rates.

Simulated reaction profiles, obtained using Eq. 5.1 and surface concentrations calculated using Eq. 5.14 – 5.15. The reaction parameters were set to values of:  $A = 1400 \text{ mol CO s}^{-1} \text{ g}_{\text{cat}}^{-1}$ ,  $E_a = 88 \text{ kJ mol}^{-1}$ ,  $C_{a,0} = 0.0409 \text{ mol m}^{-3}$ ,  $C_{O_2,0} = 4.09 \text{ mol m}^{-3}$ ,  $S_a = 76 \text{ m}^2 \text{ g}^{-1}$ , and  $T_{\text{ref}} = 298 \text{ K}$ . The flow rate (and consequently the residence time) was simulated at values of:  $v_0 = 100 \text{ mL min}^{-1}$  ( $7200 \text{ g}_{\text{cat}} \text{ s m}^3$ ) (blue),  $v_0 = 50 \text{ mL min}^{-1}$  ( $14\,400 \text{ g}_{\text{cat}} \text{ s m}^3$ ) (green), and  $v_0 = 25 \text{ mL min}^{-1}$  ( $28\,800 \text{ g}_{\text{cat}} \text{ s m}^3$ ) (red). The inset shows the maximum conversion ( $X_{\text{max}}$ ) reached for each profile.

### 5.3.6. Influence of flow rate and inlet concentration on experimental reaction profiles

Reaction profiles were recorded for CO oxidation catalyzed by Pt/Al<sub>2</sub>O<sub>3</sub> for three different average particle sizes (referring to the support,  $\gamma$ -Al<sub>2</sub>O<sub>3</sub>; the Pt nanoparticle size is constant) and two different values of  $\Theta_{O_2}$  (100, and 4). Typical results are shown in Fig. 5.5, for catalyst sieved to 20-40 mesh size (corresponding to particle diameters  $0.85 > 2R_p > 0.43$  mm). Profiles recorded at each volumetric flow rate are continuous at low conversion until catalyst light-off. At this point, the conversion increases abruptly to nearly its maximum value, over a temperature range that is less than 1 °C, Fig. 5.5A. The precise location ( $T$ ,  $X$ ) of the abrupt discontinuity is quite reproducible in consecutively recorded profiles over the same catalyst bed, Fig. 5.5A. Values of ( $T$ ,  $X$ ) at which light-off occurs, ( $T_{LO}$ ,  $X_{LO}$ ), are listed in Table 5.1 for this particle size as a function of volumetric flow rate and  $\Theta_{O_2}$ . Results for other catalyst particle sizes are collected in Tables A5.1 and A5.2 of the Appendix.

**Table 5.1.** Relationship between light-off temperature and conversion for CO oxidation catalyzed by Pt/Al<sub>2</sub>O<sub>3</sub> <sup>a</sup>

$\Theta_{O_2}$ <sup>b</sup>	$v_0$ / mL min <sup>-1</sup>	$X_{LO}$	$T_{LO}$ / °C
100	100	0.08	128
100	50	0.13	123
100	25	0.23	120
4	100	0.14	178
4	50	0.23	171
4	25	0.31	164

<sup>a</sup> Oxidation of 1000 ppm CO catalyzed by Pt/Al<sub>2</sub>O<sub>3</sub> (12 mg) sieved to a mesh size of 20-40, then diluted 1:3 with SiC (36 mg).

<sup>b</sup>  $\Theta_{O_2}$  = 100 (100 000 ppm O<sub>2</sub>) or 4 (4000 ppm O<sub>2</sub>), balance Ar.

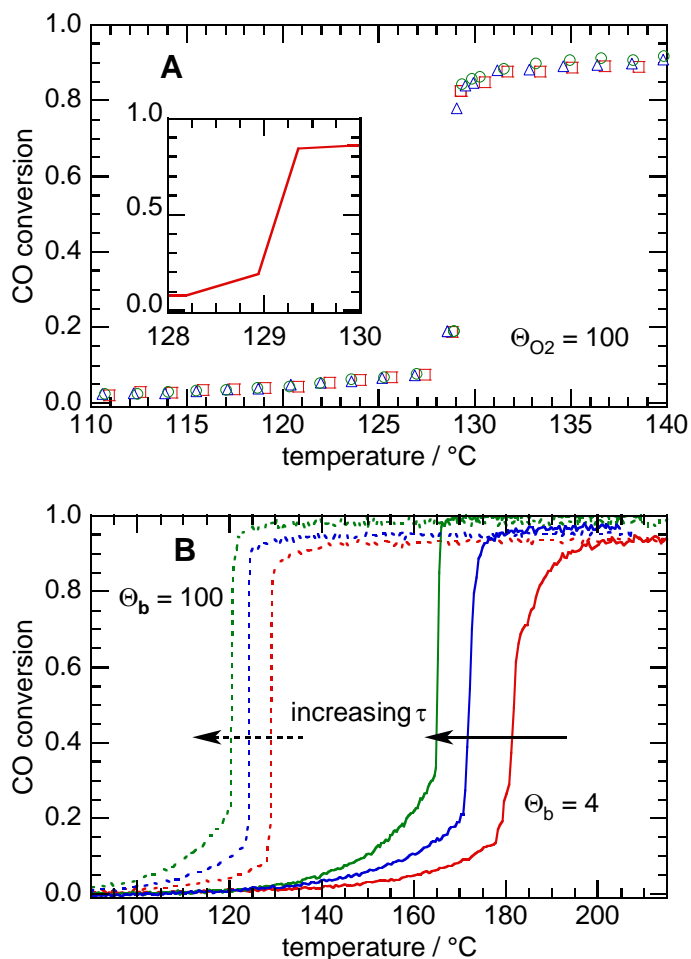


**Fig. 5.5.** Effect of inlet O<sub>2</sub> concentration and flow rate on light-off profiles for CO oxidation catalyzed by Pt/Al<sub>2</sub>O<sub>3</sub> (20-40 mesh particle size).

Reaction profiles for CO oxidation (1000 ppm CO) catalyzed by Pt/Al<sub>2</sub>O<sub>3</sub> (12 mg, sieved mesh size 20-40) diluted in SiC (36 mg). (A) Three consecutive reaction profiles, recorded with  $\Theta_{O_2} = 100$  (100 000 ppm O<sub>2</sub>) and  $v_0 = 25$  mL min<sup>-1</sup>; showing every 3<sup>rd</sup> data point. The first (red squares), second (blue triangles), and third profiles (green circles) are superposable. The inset magnifies light-off for the first reaction profile. (B) Reaction profiles recorded with  $\Theta_{O_2} = 100$  (dashed lines), and  $\Theta_{O_2} = 4$  (4000 ppm O<sub>2</sub>, solid lines). One reaction profile is shown for each flow rate, with  $v_0 = 25$  (green), 50 (blue), and 100 (red) mL min<sup>-1</sup>.



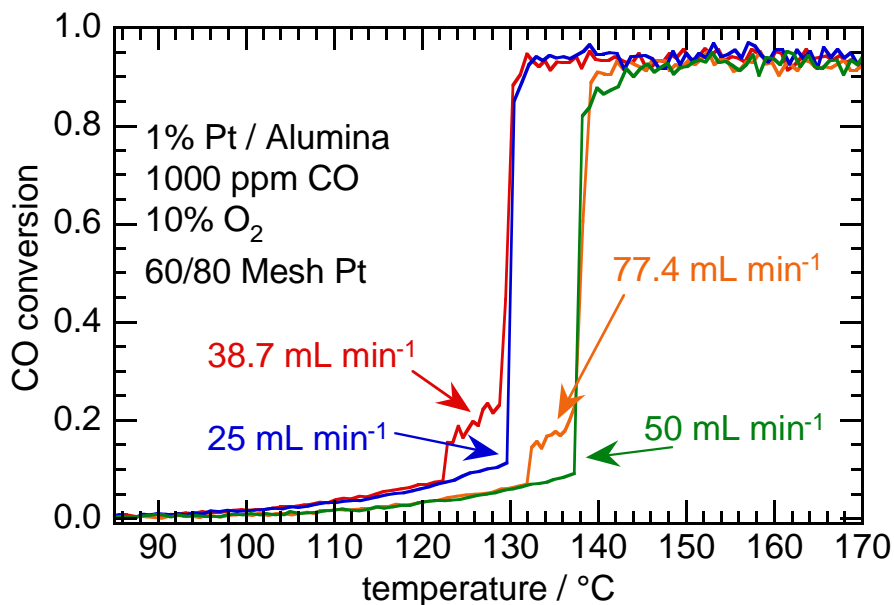


**Fig. 5.6.** Effect of residence time on light-off profiles for CO oxidation. Reaction profiles for CO oxidation (1000 ppm CO, 100 000 ppm O<sub>2</sub>, balance Ar) over Pt/Al<sub>2</sub>O<sub>3</sub> (sieved mesh size of 60-80) diluted 1:3 w/w in SiC. The mass of catalyst is 7.3 mg for profiles recorded at  $v_0 = 25 \text{ mL min}^{-1}$  (blue) and  $50 \text{ mL min}^{-1}$  (green), and 11.3 mg for profiles recorded at  $v_0 = 39 \text{ mL min}^{-1}$  (red) and  $77 \text{ mL min}^{-1}$  (orange). The flow rates were chosen so that the residence time is constant for each pair of profiles, i.e.,  $0.29 \text{ mg min mL}^{-1}$  (red/blue) and  $0.15 \text{ mg min mL}^{-1}$  (green/orange).

Increasing the volumetric flow rate causes the light-off temperature to increase, and the conversion at which light-off occurs to decrease. The increase in  $T_{LO}$  is typically caused by a decrease in the residence time, which shifts the position of the entire reaction profile [3]. To verify that this is the case here, profiles with the same residence time (but different volumetric flow rates and mass of catalyst) were recorded. The profiles are superposable before, during and after light-off, Fig. 5.6, demonstrating that the flow rate itself does not affect the light-off temperature. Increasing the inlet O<sub>2</sub> concentration causes both the light-off temperature and conversion to decrease. In a more oxidizing atmosphere, the surface is more readily oxidized, resulting in higher activity at lower temperatures [30, 31, 33, 34].

As the flow rate increases, the maximum conversion achieved also decreases. Table 5.2 shows  $X_{\max}$  for each value of  $v_0$  and  $\Theta_{O_2}$  at a constant catalyst particle size (20-40 mesh). Results for other particle sizes are shown in Table A5.4. This trend is consistent with the behavior seen in simulated reaction profiles (Fig. 5.4), which shows that observed reaction rates are impacted more by the rate of external mass transport at higher flow rates. For  $\Theta_{O_2} = 4$ , the appearance of the reaction profile above  $X_{LO}$  becomes increasingly sigmoidal at higher flow rates. At the lowest flow rate ( $v_0 = 25 \text{ mL min}^{-1}$ ), the rate accelerates as the reactor approaches maximum conversion, consistent with behavior expected for an inverse-first-order rate law. The temperature range over which the conversion increases from 0.31 to 0.99 is just 3 °C. At the highest flow rate ( $v_0 = 100 \text{ mL min}^{-1}$ ), the rate begins to decelerate above  $X = 0.7$ , causing the profile to become S-shaped as it approaches a maximum conversion of 0.93 slowly over a range of 24 °C. The change is not smooth, leveling off briefly at 185 °C ( $X = 0.7$ ) then accelerating again.

**Table 5.2.** Maximum observed conversion in CO oxidation catalyzed by Pt/Al<sub>2</sub>O<sub>3</sub> <sup>a</sup>

$\Theta_{O_2}$ <sup>b</sup>	$v_0 / \text{mL min}^{-1}$	$X_{\max}$
100	100	0.93
100	50	0.95
100	25	0.98
4	100	0.93
4	50	0.97
4	25	0.99

<sup>a</sup> Oxidation of 1000 ppm CO catalyzed by Pt/Al<sub>2</sub>O<sub>3</sub> (12 mg) sieved to a mesh size of 20-40, then diluted 1:3 with SiC (36 mg).

<sup>b</sup>  $\Theta_{O_2} = 100$  (100 000 ppm O<sub>2</sub>) or 4 (4000 ppm O<sub>2</sub>), balance Ar.

Light-off is known to occur in parallel with changes in the state of the catalyst surface, which alter the reaction kinetics. These changes, which involve surface oxidation, have been observed by *in situ* XAS, IR, and TEM [27-36, 40]. Their relationship to external mass transport limitations is highly non-linear: above  $T_{LO}$ , the rate becomes more external mass transport-limited (evidenced by the decrease in  $X_{max}$  and the sigmoidal shape of the profile as it approaches  $X_{max}$ ), and this further stabilizes the oxidized state of the surface because CO is less available at the surface to reduce Pt(II) to Pt(0).

Increasing the volumetric flow rate causes the boundary layer for diffusion and heat transfer to and from the catalyst surface to become thinner, and increases the heat transfer coefficient ( $h$ ) for the fluid. This results in more dissipation of the heat of reaction by convection and advection because  $h$  is proportional to  $v_0^{0.5}$  according to the relationship  $h = (2 + 0.6Re^{0.5}Pr^{1/3})\lambda/R_p$  and the Reynold's number (Re) is proportional to  $v_0$  [39]. Consequently, the observed decrease in  $X_{LO}$  and  $T_{LO}$  with increasing  $v_0$  cannot be attributed to formation of hot spots or large temperature gradients in the catalyst bed, because higher flow rates result in light-off at lower conversion. The opposite trend would be observed if enhanced heat transfer due to the higher flow rate were responsible for light-off.

### 5.3.7. Influence of particle size on experimental reaction profiles

The effect of catalyst particle size was explored by recording reaction profiles for three different particle size ranges. A typical result is shown in Fig. 5.7 for  $v_0 = 50 \text{ mL min}^{-1}$  and  $\Theta_{O_2} = 100$ . Results for other flow rates and oxygen concentrations can be seen in Fig. 5.8. For a particular particle size, the three reaction profiles recorded consecutively are superposable over the entire range of conversion, including the abrupt discontinuity at light-off. The reaction profiles recorded for different particle sizes are all superposable up to 123

°C and  $X = 0.13$ . At this point, the profile corresponding to the largest particle size (20-40 mesh) exhibits light-off: the rate accelerates rapidly and the conversion jumps to  $X = 0.91$ , eventually leveling off at  $X_{\max} = 0.95$ . The profiles for the smaller and size distributions continue to increase smoothly up to 126 °C ( $X_{LO} = 0.17$ ), when the profile recorded for the intermediate particle size exhibits light-off. The profile for the smallest particle size eventually lights off at 131 °C ( $X_{LO} = 0.25$ ).

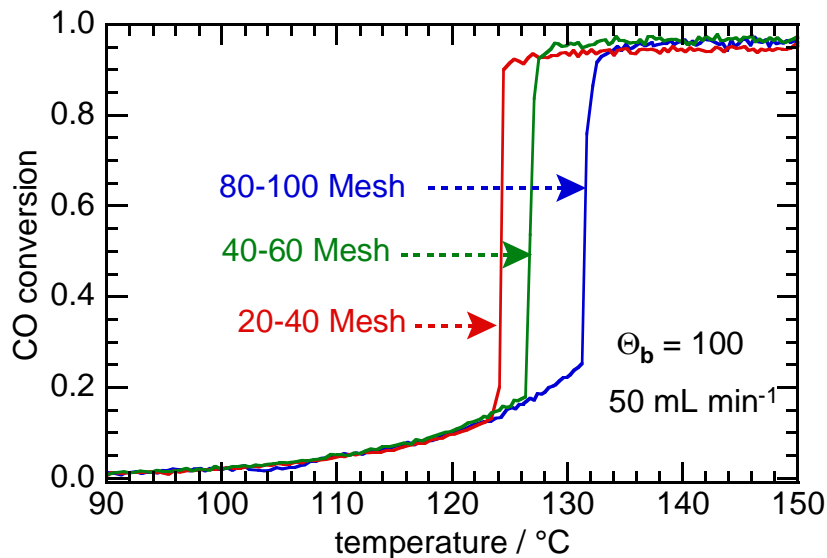


**Fig. 5.7.** Effect of particle size on the light-off profile for CO oxidation ( $\Theta_{O_2} = 100$ ,  $v_0 = 50$  mL min<sup>-1</sup>) catalyzed by Pt/Al<sub>2</sub>O<sub>3</sub>  
 Reaction profiles for CO oxidation (1000 ppm CO, 100 000 ppm O<sub>2</sub>, balance Ar,  $v_0 = 50$  mL min<sup>-1</sup>) catalyzed by Pt/Al<sub>2</sub>O<sub>3</sub> (ca. 12 mg) diluted in SiC (36 mg). One reaction profile is shown for each particle size distribution. The particle sizes are: 80-100 mesh ( $0.18 > 2R_p > 0.15$  mm, blue), 40-60 mesh ( $0.42 > 2R_p > 0.25$  mm, green), and 20-40 mesh ( $0.84 > 2R_p > 0.42$  mm, red).

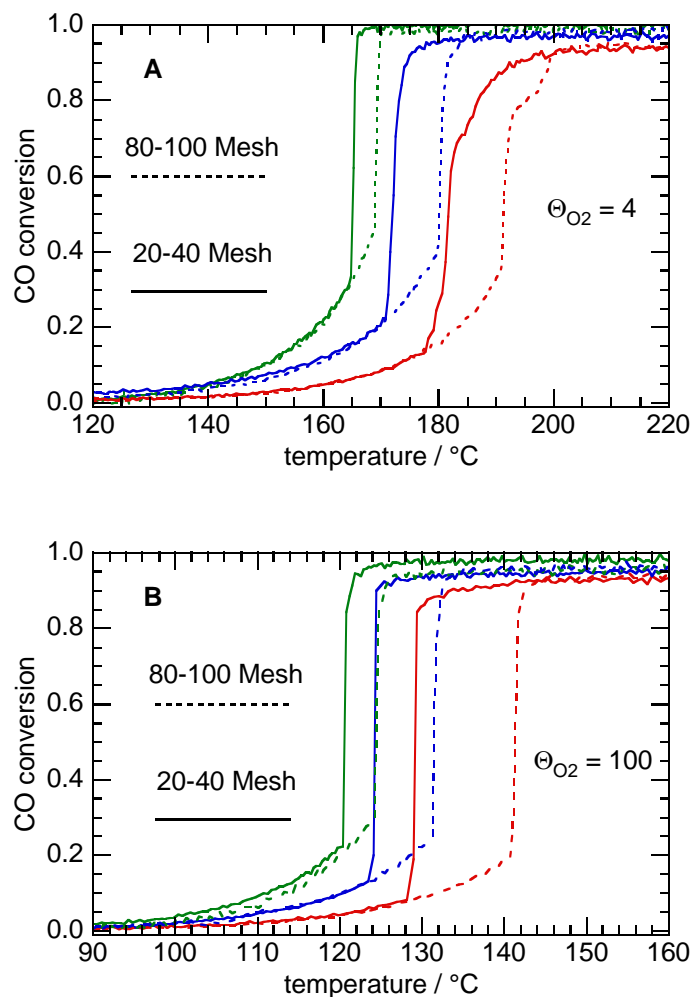


**Fig. 5.8.** Particle size effect on light-off profiles for CO oxidation catalyzed by Pt/Al<sub>2</sub>O<sub>3</sub>. Reaction profiles for CO oxidation with (A) (1000 ppm CO, 4000 ppm O<sub>2</sub>, balance Ar) or (B) (1000 ppm CO, 100 000 ppm O<sub>2</sub>, balance Ar) catalyzed by Pt/Al<sub>2</sub>O<sub>3</sub> (ca. 12 mg) diluted in SiC (36 mg), for different particle sizes: 80-100 mesh ( $0.18 > 2R_p > 0.15$  mm, dashed lines), and 20-40 mesh ( $0.84 > 2R_p > 0.42$  mm, solid lines). Additional reaction profiles recorded for 40-60 mesh size particles ( $0.42 > 2R_p > 0.25$  mm) are shown in the Appendix. One reaction profile is shown for each volumetric flow rate,  $v_0 = 25$  (green), 50 (blue), and 100 (red) mL min<sup>-1</sup>.

As the particle size increases, the barrier to internal diffusion also increases. Eq. 5.16 shows the Weisz-Prater Criterion ( $C_{wp}$ ) [41], for which  $C_{a,s}$  is the surface concentration of the limiting reactant and  $D_{TA}^e$  is the effective diffusivity of the gas mixture which is an average of the molecular diffusivity and the Knudsen diffusivity.

$$C_{wp} = \frac{-r_a R_p^2}{D_{TA}^e C_{a,s}} \quad (5.16)$$

Reaction conditions for which  $C_{wp} < 1$  are deemed kinetically-controlled. As  $R_p$  increases, so does the resistance to internal mass transport, while the CO concentration inside the catalyst pores decreases. These factors cause  $C_{wp}$  to increase and signal the onset of internal mass transport limitations at lower values of temperature and conversion.

When the CO concentration inside the catalyst pores decreases, this suppresses the CO poisoning effect. *In situ* IR spectroscopy showed that light-off is accompanied by a sudden decrease in the amount of CO linearly-bound to metallic Pt [28]. *In situ* and *operando* XAS measurements demonstrated that the metal is converted to an oxide at light-off [27, 30-33]. Since the ratio of gas phase concentrations  $C_{O_2}/C_{CO}$  in the pores is much higher than in the bulk gas phase, the catalyst particles are more readily oxidized. The two effects (catalyst light-off, which causes  $C_{CO}$  to decrease, and Pt oxidation, which causes rate acceleration due to suppression of CO poisoning) constitute a positive feedback loop in which cause and effect are inextricably confounded. The decrease in both  $X_{LO}$  and  $T_{LO}$  for larger values of  $R_p$  and  $\Theta_{O_2}$  suggest that increasing the ratio  $C_{O_2}/C_{CO}$  inside the catalyst pores causes light-off to occur at lower temperatures. Oxide formation begins deep in the pores and propagates outward, resulting in rapid rate acceleration.

We also considered the possibility that larger catalyst particles exhibit temperature gradients (i.e., the internal temperature of the particle exceeds the surface temperature). An increase in internal temperature would result in an increase in the effectiveness factor, causing light-off to occur at lower values of the external temperature ( $T_{LO}$ ). The Biot number ( $Bi = h R_p / \lambda$ ), where  $\lambda$  is the thermal conductivity of the catalyst (see Appendix 5), is used to assess the existence of thermal gradients. For  $Bi \ll 1$ , thermal gradient inside catalyst particles are negligible. For all values of  $v_0$  and  $R_p$  used in this work, the value of  $Bi$  is of order  $10^{-3}$ , therefore no thermal gradients are present. Empirical tests of a similar Pd/Al<sub>2</sub>O<sub>3</sub> catalyst for CO oxidation using the same reactor design showed that external heat transfer is does not affect the rate of reaction [3]. Therefore we can assume that our catalyst is thermally equilibrated under all reaction conditions, and thermal gradients in catalyst particles do not affect light-off.

The same trends were observed for each combination of  $v_0$  and  $\Theta_{O_2}$ , Figs. 5.8 (for clarity, only profiles for the smallest and largest particle sizes are shown). At all flow rates, the reaction profiles are superposable below light-off. The transition always occurs at lower values of conversion and temperature for larger particles, due to their greater internal diffusion limitations. The maximum conversion does not change noticeably for catalyst sieved to different particle sizes; our simulations showed that  $X_{max}$  is unaffected by internal transport limitations (see section Fig. 5.3).

For particles sieved to 80-100 mesh at  $\Theta_{O_2} = 4$  and  $v_0 = 100 \text{ mL min}^{-1}$ ), a second light-off event is visible, Fig. 5.8. A possible explanation is that the surface again becomes poisoned by CO or partially reduced to Pt(0). This reduces the rate and the conversion briefly plateaus. However, autocatalytic oxidation of the surface occurs again and a second

light-off event is observed. *In situ* and *operando* XAS and IR should be performed under these reaction conditions to better understand the state of the catalyst between the initial light-off and before the profile reach  $X_{\max}$ .

### 5.3.8. Curve-fitting experimental profiles

Eq. 5.5, which was derived assuming that the entire reaction profile is kinetically-limited, was used to curve-fit data that had been truncated just below the abrupt increase in rate. Reaction orders were fixed at -1 with respect to CO and +1 and with respect to O<sub>2</sub>, based on the Langmuir Hinshelwood reaction mechanism for CO oxidation over Pt nanoparticles on alumina [42]. The results are presented in Table 5.3. Fig. 5.9 shows a representative curve-fit to a single profile below  $X_{LO}$ . In addition, the fit parameters were used to simulate results up to  $X = 1$ . Above  $X_{LO}$ , the predicted kinetically-limited conversion deviates significantly from the experimental reaction profile. However, simulated reaction profiles that include mass transport effects (Fig. 5.1 – 5.4) deviate from kinetically-limited behavior gradually, not abruptly. The sudden increase in rate associated with light-off is therefore not a direct result of the onset of mass transport limitations. Instead, it is likely caused by an abrupt change in mechanism, associated with a change in surface chemistry which is observable by *in situ* IR [28], TEM [36], and XAS [27, 31, 32].



**Table 5.3.** Activation parameters for CO oxidation<sup>1</sup> over Pt/Al<sub>2</sub>O<sub>3</sub>

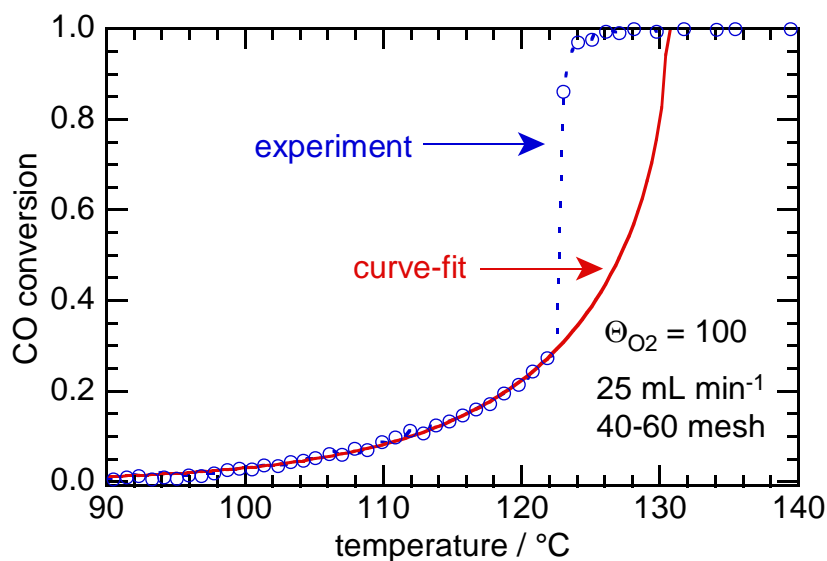
Data acquisition method	$E_a$ / kJ mol <sup>-1</sup>	$A$ / mol CO g <sub>cat</sub> <sup>-1</sup> s <sup>-1</sup>
Variable-temperature kinetic profile <sup>2</sup>	99 ± 4	(4.8 ± 1.0) × 10 <sup>4</sup>
steady-state differential conversion <sup>3</sup>	100 ± 10	N/A <sup>4</sup>

<sup>1</sup> Ca. 12 mg Pt/Al<sub>2</sub>O<sub>3</sub> diluted 1:3 with SiC,  $v_0 = 25, 50$ , or 100 mL min<sup>-1</sup>,  $\Theta_{O_2} = 100$  (1000 ppm CO, 100 000 ppm O<sub>2</sub>, balance Ar), or  $\Theta_{O_2} = 4$  (1000 ppm CO, 4000 ppm O<sub>2</sub>, balance Ar). Catalyst was sieved with mesh size distributions of 80-100, 40-60, and 20-40 mesh.

<sup>2</sup> Values for a global fit to 35 profiles recorded for three particle sizes and two values of  $\Theta_{O_2}$ .

<sup>3</sup> Averaged values for individual Arrhenius plots for three particle sizes and two  $\Theta_{O_2}$  values, recorded at steady-state or  $0.02 < X < 0.10$ . Uncertainty is the standard deviation for all profiles.

<sup>4</sup>  $A$  cannot be extracted from the  $y$ -intercept of an Arrhenius plot of  $\ln[X]$ .

**Fig. 5.9.** Individual curve-fit of Eq. 5.5 to a single reaction profile for CO oxidation catalyzed by Pt/Al<sub>2</sub>O<sub>3</sub>.

Reaction profile for CO oxidation (1000 ppm CO, 100 000 ppm O<sub>2</sub>, balance Ar, 25 mL min<sup>-1</sup>) over Pt/Al<sub>2</sub>O<sub>3</sub> (12 mg, sieved to 40-60 mesh) diluted in SiC (36 mg). Every third data point is displayed (blue circles and dashed line). Red line is the individual curve-fit of Eq. 5.5 to data up to  $X = 0.28$ , then extrapolated to  $X = 1$ .

The same value for the activation energy,  $100 \text{ kJ mol}^{-1}$ , was obtained by curve-fitting each subset of profiles corresponding to a specific value of catalyst particle size and  $\Theta_{\text{O}_2}$ , Table. A5.4. It is consistent with other reported values for supported Pt(0) nanoparticles [19], Table 5.1. Since the value of  $E_a$  obtained from global non-linear curve-fitting of reaction profiles is identical for all particle sizes, the results are deemed free of internal diffusion limitations. The pre-exponential factors obtained in this way vary from  $(0.24 \times 10^5)$  to  $(2.6 \times 10^5) \text{ mol CO g}_{\text{cat}}^{-1} \text{ s}^{-1}$ .

Data between  $0.02 < X < 0.10$  were used to create an Arrhenius plot and the activation energies were extracted. Representative Arrhenius plots that gave values for  $E_a$  of 80, 90, and  $110 \text{ kJ mol}^{-1}$  are shown in Fig. 5.10 and all the results are shown in Table A5.6. There is no trend with particle size or flow rate. Although individual Arrhenius plots give  $E_a$  values ranging from 80 to  $130 \text{ kJ mol}^{-1}$ , the average from all profiles is  $(100 \pm 10) \text{ kJ mol}^{-1}$  (Table 5.3). This average value of  $E_a$  is identical to that obtained from non-linear curve-fitting, albeit with a much larger uncertainty. As previously reported [3], values of  $E_a$  obtained from non-linear curve-fitting of reaction profiles are more precise compared to those obtained from conventional analysis of differential kinetic data. Because curve-fitting with Eq. 5.5 returns a value consistent with the conventional Arrhenius analysis, the superposable low conversion regions of the reaction profiles are deemed kinetically-limited.

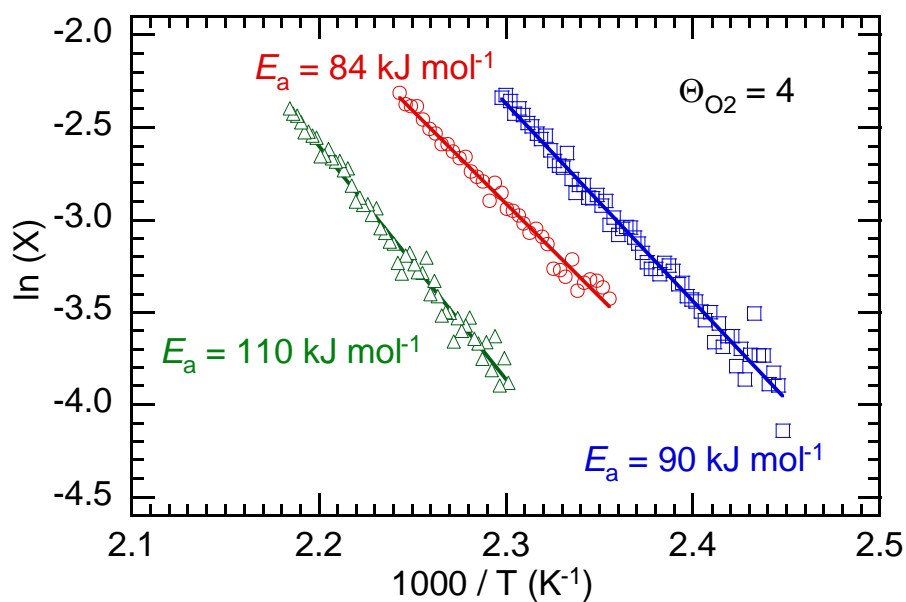


**Fig. 5.10.** Representative Arrhenius plots for CO oxidation catalyzed by Pt/Al<sub>2</sub>O<sub>3</sub>. Arrhenius plots for CO oxidation (1000 ppm CO, 4000 ppm O<sub>2</sub>, balance Ar) over Pt/Al<sub>2</sub>O<sub>3</sub> (12 mg, diluted in 36 mg SiC. Data used are taken from the range  $0.02 < X < 0.1$ . For catalyst sieved to 20-40 mesh size,  $v_0 = 100 \text{ mL min}^{-1}$  (red circles); 80-100 mesh size,  $v_0 = 25 \text{ mL min}^{-1}$  (blue squares) and  $v_0 = 100 \text{ mL min}^{-1}$  (green triangles).

## 5.4. Conclusion

Simulated reaction profiles under the influence of internal and external mass transport limitations were simulated. The profiles are continuous for all values of  $X$  and  $T$  and no abrupt changes in activity are observed. Severe external mass transport limitations decrease the maximum conversion reached in the reactor and the profile becomes *S*-shaped, particularly at high conversion. Internal mass transport limitations shift profiles to higher temperatures to achieve the same conversion as kinetically-limited profiles.

At low conversion, the rate of CO oxidation over Pt/Al<sub>2</sub>O<sub>3</sub> is kinetically-limited and obeys a simple power rate law which allows for the extraction of reliable activation parameters by variable-temperature kinetic analysis. Light-off occurs at low-to-medium conversion, with the precise temperature depending on the concentration of O<sub>2</sub>, flow rate, and catalyst particle size. Trends in light-off temperatures are correlated with transport limitations, particularly internal diffusion limitations.

Transport limitations for CO (particularly internal diffusion) cause light-off to occur at lower values of  $T_{LO}$  and  $X_{LO}$ . Above light-off, the faster rate causes the value of  $C_{CO,surface}$  to decrease further, which accentuates external mass transport limitations, particularly at larger flow rates ( $v_0 = 100 \text{ mL min}^{-1}$ ). When the concentration of CO is low enough inside the pores, Pt is converted to a super-active surface oxide, further decreasing  $C_{CO,surface}$  and enhancing external transport limitations.

## Appendix 5

### A5.1. Calculation of mass transfer coefficient and Mears' Criterion

The mass transfer coefficient  $k_c$  is estimated from empirical correlations for a packed bed reactor according to [43]:

$$k_c = 1.17 Re^{-.42} Sc^{2/3} u \quad (\text{A5.1})$$

where  $Re$  and  $Sc$  are the dimensionless Reynolds and Schmidt numbers, respectively:

$$Sc = \frac{\mu}{\rho D_{12}} \quad (\text{A5.2})$$

$$Re = \frac{u \rho (2R_p)}{\mu} \quad (\text{A5.3})$$

and the diffusivity,  $D_{12}$ , was set to be  $2 \times 10^{-5} \text{ m}^2 \text{ s}^{-1}$  at 298 K, the viscosity was set to  $3 \times 10^{-5} \text{ Pa} \cdot \text{s}$  at 298 K, and the density was set to  $1.6 \text{ kg m}^{-3}$  (typical values for Ar at 298 K [44-46]).

The linear fluid velocity,  $u$ , depends on the volumetric flow rate  $v_0$  and the reactor cross-sectional area  $A_c$  which were estimated using our reactor dimensions and a flow rate of  $25 \text{ mL min}^{-1}$ :

$$A_c = \pi \left( \frac{d}{2} \right)^2 = \pi \left( \frac{0.0039 \text{ m}}{2} \right)^2 = 1.2 \times 10^{-5} \text{ m}^2 \quad (\text{A5.4})$$

$$v_0 = v_{0,\text{ref}} \frac{T}{T_{\text{ref}}} = \left( 0.025 \frac{\text{L}}{\text{min}} \right) \left( \frac{\text{m}^3}{10^3 \text{ L}} \right) \left( \frac{\text{min}}{60 \text{ s}} \right) = 4.2 \times 10^{-7} \frac{\text{m}^3}{\text{s}} \quad (\text{A5.5})$$

$$u = \frac{v_0}{A_c} = \frac{4.2 \times 10^{-7} \frac{m^3}{s}}{1.2 \times 10^{-5} m^3} = 0.04 \frac{m}{s} \quad (A5.6)$$

Thus, the estimated values of the dimensionless numbers are:

$$Sc = \frac{\mu}{\rho D_{12}} = \frac{2.5 \times 10^{-5} Pa \cdot s}{\left(1.6 \frac{kg}{m^3}\right) \left(2 \times 10^{-4} \frac{m^2}{s}\right)} = 0.79 \quad (A5.7)$$

$$Re = \frac{u \rho (2R_p)}{\mu} = \frac{\left(0.04 \frac{m}{s}\right) \left(1.6 \frac{kg}{m^3}\right) (1.65 \times 10^{-4} m)}{2.5 \times 10^{-5} Pa \cdot s} = 0.38 \quad (A5.8)$$

Together, they lead to the following estimate for the mass transfer coefficient:

$$k_c = 1.17(0.38)^{-0.42}(0.79)^{2/3} 0.04 \frac{m}{s} = 0.05 \frac{m}{s} \quad (A5.9)$$

From experimental results we could estimate a  $(T, X)$  pair of 128 C and  $X = 0.1$ . The rate of reaction would be  $0.04 \text{ mol CO m}^{-3} \text{ s}^{-1}$  for particles with radius,  $R_p = 8.3 \times 10^{-5} \text{ m}$ .

$$\frac{-r_a R_p n}{k_c C_{a, bulk}} = \frac{\left(0.04 \frac{\text{mol CO}}{\text{m}^3 \cdot \text{s}}\right) (8.3 \times 10^{-5} \text{ m})}{\left(0.08 \frac{m}{s}\right) \left(3.0 \times 10^{-2} \frac{\text{mol CO}}{\text{m}^3}\right) (1-0.1)} = 0.0014 \quad (A5.10)$$

Mears' criterion is much less than 0.15, thus the reaction is kinetically-limited.

## A5.2. Calculation of Biot number

The Biot number gives the ratio of heat transfer by a fluid to the heat transfer inside a solid object, Eq. A5.11.

$$Bi = \frac{hL}{\lambda_{\text{solid}}} \quad (\text{A5.11})$$

Where  $h$  is the heat transfer coefficient of the fluid (argon),  $L$  is the characteristic length (radius of the catalyst support,  $R_p$ ), and  $\lambda_{\text{solid}}$  is the thermal conductivity of the solid (alumina). The value of  $\lambda$  for alumina is  $18 \text{ W m}^{-1} \text{ K}^{-1}$  [43]. For catalyst sieved to 80-100 mesh size the mean  $R_p$  is  $8.3 \times 10^{-5} \text{ m}$ . The heat transfer coefficient,  $h$ , can be estimated from the Nusselt number,  $Nu$  [47]:

$$Nu = \frac{h(2R_p)}{\lambda_{\text{fluid}}} = 2 + 0.6Re^{0.5}Pr^{1/3} \quad (\text{A5.12})$$

The thermal diffusivity,  $\alpha$ , for Ar is used to calculate the Prandtl number,  $Pr$ . The thermal conductivity for Ar,  $\lambda_{\text{fluid}}$ , is  $0.027 \text{ W m}^{-1} \text{ K}^{-1}$  at 298 K [48]; its density,  $\rho$ , is  $1.6 \text{ kg/m}^3$  (at 573 K); and its heat capacity,  $C_p$ , is  $570 \text{ J kg}^{-1} \text{ K}^{-1}$  [49].

$$\alpha = \frac{\lambda_{\text{fluid}}}{\rho C_p} = \frac{0.027 \frac{\text{W}}{\text{m} \cdot \text{K}}}{\left(1.6 \frac{\text{kg}}{\text{m}^3}\right) \left(570 \frac{\text{J}}{\text{kg} \cdot \text{K}}\right)} = 2.9 \times 10^{-5} \frac{\text{m}^2}{\text{s}} \quad (\text{A5.13})$$

$$Pr = \frac{\mu}{\rho \alpha} = \frac{(3.0 \times 10^{-5} \text{ Pa} \cdot \text{s})}{\left(1.6 \frac{\text{kg}}{\text{m}^3}\right) \left(2.9 \times 10^{-5} \frac{\text{m}^2}{\text{s}}\right)} = 0.63 \quad (\text{A5.14})$$

The heat transfer coefficient,  $h$ , is obtained by rearranging Eq. A5.11:

$$h = \left(2 + 0.6Re^{0.5}Pr^{\frac{1}{3}}\right) \frac{\lambda_{\text{fluid}}}{2R_p} = \left(2 + 0.6(0.38)^{0.5}(0.63)^{\frac{1}{3}}\right) \frac{0.027 \frac{\text{W}}{\text{m} \cdot \text{K}}}{8.3 \times 10^{-5} \text{ m}} = 377 \frac{\text{W}}{\text{m}^2 \cdot \text{K}} \quad (\text{A5.15})$$

so the Biot number is

$$Bi = \frac{hL}{\lambda_{\text{solid}}} = \frac{\left(377 \frac{\text{W}}{\text{m}^2 \cdot \text{K}}\right) (8.3 \times 10^{-5} \text{m})}{18 \frac{\text{W}}{\text{m} \cdot \text{K}}} = 1.73 \times 10^{-3} \ll 1 \quad (\text{A5.16})$$

The value of Bi is much less than one, indicating that the solid catalyst particles are homogeneous in temperature, i.e. the catalyst particles has no internal temperature gradients.

The value of Bi for every flow rate and catalyst support size is given in Table A5.1.

**Table A5.1.** Biot number for Pt/AL<sub>2</sub>O<sub>3</sub>

$R_p / \mu\text{m}$	$v_0 / \text{mL min}^{-1}$	Bi x 10 <sup>3</sup>
320	25	1.9
320	50	2.1
320	100	2.3
168	25	1.8
168	50	1.9
168	100	2.1
82.5	25	1.7
82.5	50	1.8
82.5	100	1.9



### A5.3. CO oxidation catalyzed by Pt/Al<sub>2</sub>O<sub>3</sub>: Figures and Tables

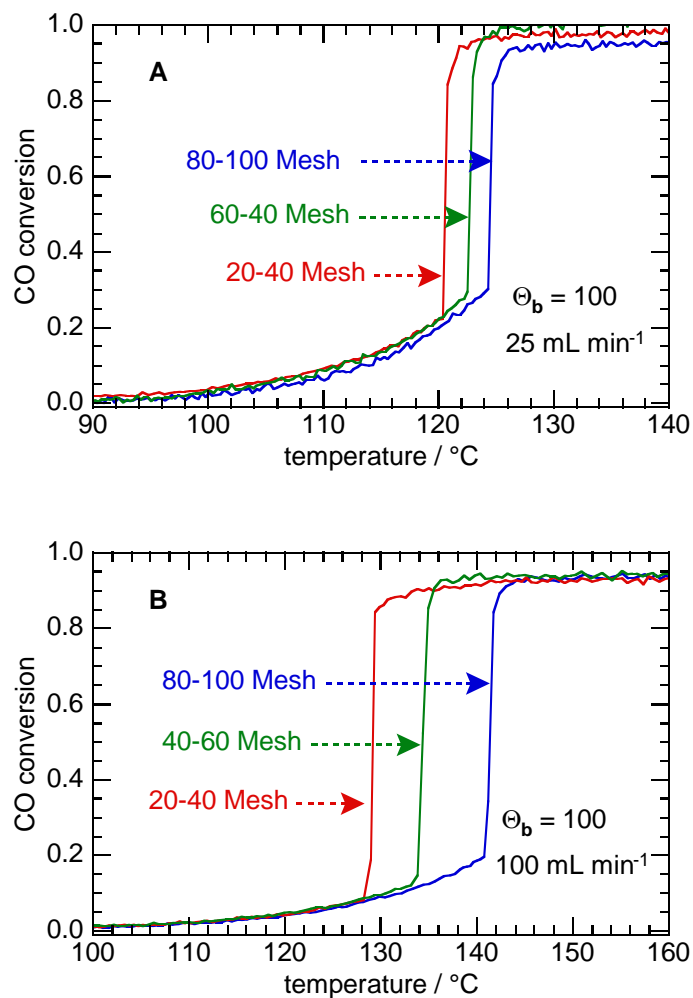


**Fig. A5.1.** Effect of particle size on the light-off profile for CO oxidation ( $\Theta_{O_2} = 100$ ) catalyzed by Pt/Al<sub>2</sub>O<sub>3</sub>. Reaction profiles for CO oxidation (1000 ppm CO, 100 000 ppm O<sub>2</sub>, balance Ar) catalyzed by Pt/Al<sub>2</sub>O<sub>3</sub> (ca. 12 mg) diluted in SiC (36 mg). (A)  $v_0 = 25 \text{ mL min}^{-1}$  and (B)  $v_0 = 100 \text{ mL min}^{-1}$ . One reaction profile is shown for each particle size distribution. The particle sizes are: 80-100 mesh ( $0.18 > 2R_p > 0.15 \text{ mm}$ , blue), 40-60 mesh ( $0.42 > 2R_p > 0.25 \text{ mm}$ , green), and 20-40 mesh ( $0.84 > 2R_p > 0.42 \text{ mm}$ , red).

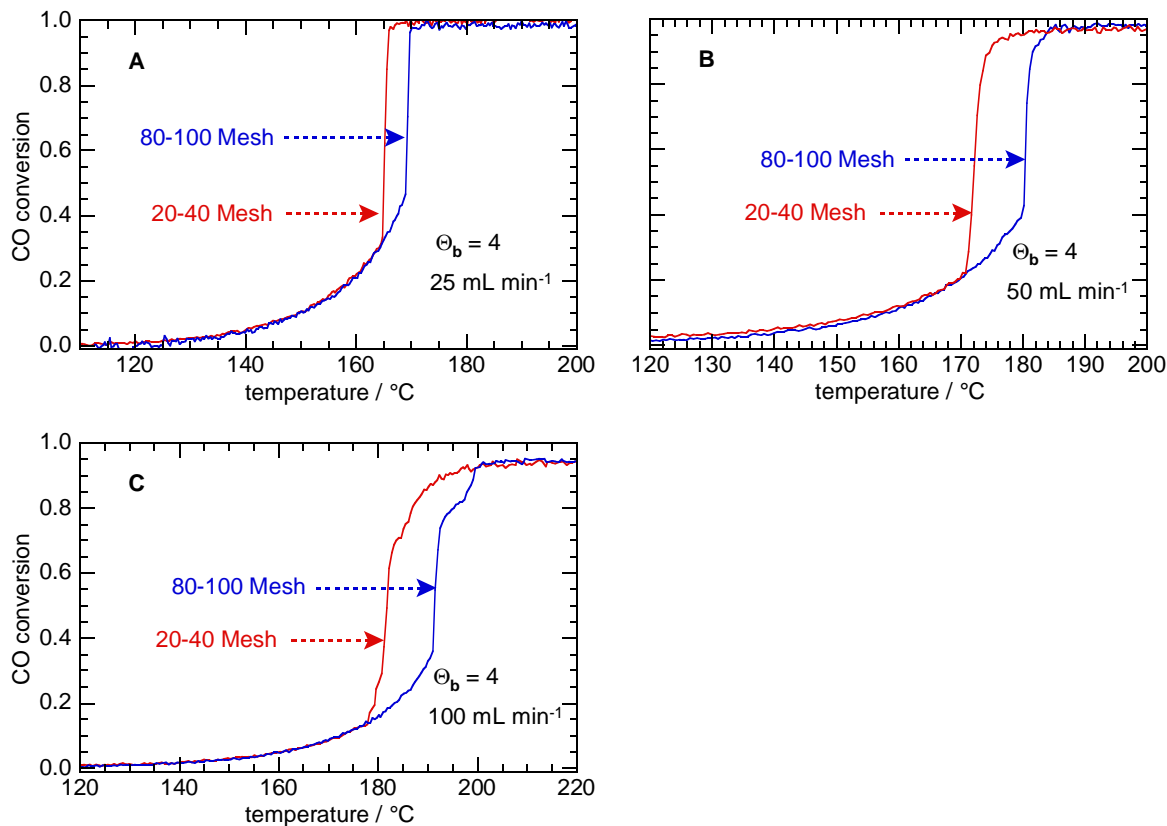


**Fig. A5.2.** Effect of particle size on the light-off profile for CO oxidation ( $\Theta_{O_2} = 4$ ) catalyzed by Pt/Al<sub>2</sub>O<sub>3</sub>. Reaction profiles for CO oxidation (1000 ppm CO, 100 000 ppm O<sub>2</sub>, balance Ar) catalyzed by Pt/Al<sub>2</sub>O<sub>3</sub> (ca. 12 mg) diluted in SiC (36 mg). (A)  $v_0 = 25 \text{ mL min}^{-1}$ , (B)  $v_0 = 50 \text{ mL min}^{-1}$ , and (C)  $v_0 = 100 \text{ mL min}^{-1}$ . One reaction profile is shown for each particle size distribution. The particle sizes are: 80-100 mesh ( $0.18 > 2R_p > 0.15 \text{ mm}$ , blue) and 20-40 mesh ( $0.84 > 2R_p > 0.42 \text{ mm}$ , red).

**Table A5.2.** Light-off temperature and conversion for CO oxidation over Pt/Al<sub>2</sub>O<sub>3</sub> (40-60 mesh size)

$\Theta_{O_2}$	$v_0 / \text{mL min}^{-1}$	$X_{LO}$	$T_{LO} / ^\circ\text{C}$
100	100	0.08	134
100	50	0.13	124
100	25	0.23	122

CO oxidation for  $\Theta_{O_2} = 100$  (1000 ppm CO, 100 000 ppm O<sub>2</sub>, balance Ar) and  $\Theta_{O_2} = 4$  (1000 ppm CO, 4000 ppm O<sub>2</sub>, balance Ar) over Pt/Al<sub>2</sub>O<sub>3</sub> (12 mg) sieved to a mesh size of 40-60, diluted 3:1 in SiC (36 mg).

**Table A5.3.** Light-off temperature and conversion for CO oxidation over Pt/Al<sub>2</sub>O<sub>3</sub> (80-100 mesh size)

$\Theta_{O_2}$	$v_0 / \text{mL min}^{-1}$	$X_{LO}$	$T_{LO} / ^\circ\text{C}$
100	100	0.20	140
100	50	0.25	131
100	25	0.29	124
4	100	0.36	191
4	50	0.40	180
4	25	0.46	169

CO oxidation for  $\Theta_{O_2} = 100$  (1000 ppm CO, 100 000 ppm O<sub>2</sub>, balance Ar) and  $\Theta_{O_2} = 4$  (1000 ppm CO, 4000 ppm O<sub>2</sub>, balance Ar) over Pt/Al<sub>2</sub>O<sub>3</sub> (12 mg) sieved to a mesh size of 80-100, diluted 3:1 in SiC (36 mg).

**Table A5.4.** Maximum observed conversion for CO oxidation over Pt/Al<sub>2</sub>O<sub>3</sub>

Mesh size	$\Theta_{\text{O}_2}$	$v_0$ / mL min <sup>-1</sup>	$X_{\text{max}}$
80-100	100	100	0.94
80-100	100	50	0.96
80-100	100	25	0.94
80-100	4	100	0.94
80-100	4	50	0.98
80-100	4	25	0.99
40-60	100	100	0.94
40-60	100	50	0.96
40-60	100	25	1.0

CO oxidation for  $\Theta_{\text{O}_2} = 100$  (1000 ppm CO, 100 000 ppm O<sub>2</sub>, balance Ar) and  $\Theta_{\text{O}_2} = 4$  (1000 ppm CO, 4000 ppm O<sub>2</sub>, balance Ar) over Pt/Al<sub>2</sub>O<sub>3</sub> (12 mg), diluted 3:1 in SiC (36 mg).

**Table A5.5.** Global curve-fit parameters from non-linear kinetic analysis of variable-temperature profiles for CO oxidation catalyzed by Pt/Al<sub>2</sub>O<sub>3</sub>

Mesh size	$\Theta_{\text{O}_2}$	$E_a$ / kJ mol <sup>-1</sup>	$A$ / mol CO g <sub>cat</sub> <sup>-1</sup> s <sup>-1</sup> x 10 <sup>-5</sup>
80-100	100	106 ± 3	2.8 ± 0.3
80-100	4	100 ± 2	0.84 ± 0.05
40-60	100	99 ± 4	0.37 ± 0.05
20-40	100	98 ± 4	0.24 ± 0.03
20-40	4	102 ± 2	1.3 ± 0.1

CO oxidation for  $\Theta_{\text{O}_2} = 100$  (1000 ppm CO, 100 000 ppm O<sub>2</sub>, balance Ar) and  $\Theta_{\text{O}_2} = 4$  (1000 ppm CO, 4000 ppm O<sub>2</sub>, balance Ar) over Pt/Al<sub>2</sub>O<sub>3</sub> (12 mg), diluted 3:1 in SiC (36 mg). Data up light-off. Values are for global curve-fits to profiles at  $v_0 = 25, 50$ , and 100 mL min<sup>-1</sup>.

**Table A5.6.** Arrhenius plot activation energy for CO oxidation catalyzed by Pt/Al<sub>2</sub>O<sub>3</sub>

Mesh size	$\Theta_{\text{O}_2}$	$v_0 / \text{mL min}^{-1}$	$E_a / \text{kJ mol}^{-1}$
80-100	100	100	110
80-100	100	50	93
80-100	100	25	89
80-100	4	100	100
80-100	4	50	93
80-100	4	25	82
40-60	100	100	83
40-60	100	50	90
40-60	100	25	120
20-40	100	100	87
20-40	100	50	96
20-40	100	25	110
20-40	4	100	84
20-40	4	50	58
20-40	4	25	110

CO oxidation for  $\Theta_{\text{O}_2} = 100$  (1000 ppm CO, 100 000 ppm O<sub>2</sub>, balance Ar) and  $\Theta_{\text{O}_2} = 4$  (1000 ppm CO, 4000 ppm O<sub>2</sub>, balance Ar) over Pt/Al<sub>2</sub>O<sub>3</sub> (12 mg), diluted 3:1 in SiC (36 mg). Data for  $0.02 < X < 0.1$  only.

## References

- [1] S. Kozuch, J.M.L. Martin, "Turning over" definitions in catalytic cycles, *ACS Catal.* 2 (2012) 2787-2794.
- [2] S.P. Asprey, B. W. Wojciechowski, B.A. Peppley, Kinetic studies using temperature-scanning: the steam-reforming of methanol, *Appl. Catal. A: Gen.* 179 (1999) 51-70.
- [3] D.H. Collier, B.C. Vicente, S.L. Scott, Rapid extraction of quantitative kinetic information from non-isothermal reaction profiles, *Chem. Eng. J.* (2016).
- [4] F. Duprat, Light-off curve of catalytic reaction and kinetics, *Chem. Eng. Sci.* 57 (2002) 901-911.
- [5] J.E. Etheridge, T.C. Watling, Is reactor light-off data sufficiently discriminating between kinetic parameters to be used for developing kinetic models of automotive exhaust aftertreatment catalysts? The effect of hysteresis induced by strong self inhibition, *Chem. Eng. J.* 264 (2015) 376-388.
- [6] N. Matthess, D. Schweich, B. Martin, F. Castagna, From light-off curves to kinetic rate expressions for three-way catalysts, *Top. Catal.* 16 (2001) 119-124.
- [7] B.W. Wojciechowski, S.P. Asprey, Kinetic studies using temperature-scanning: the oxidation of carbon monoxide, *Appl. Catal. A: Gen.* 190 (2000) 1-24.
- [8] D. Bhatia, M.P. Harold, V. Balakotaiah, Kinetic and bifurcation analysis of the cooxidation of CO and H<sub>2</sub> in catalytic monolith reactors, *Chem. Eng. Sci.* 64 (2009) 1544-1558.
- [9] C. Depcik, S. Loya, A. Srinivasan, T. Wentworth, S. Stagg-Williams, Adaptive global carbon monoxide kinetic mechanism over platinum/alumina catalysts, *Catalysts* 3 (2013) 517-542.
- [10] R.E. Hayes, F.H. Bertrand, C. Audet, S.T. Kolaczowski, Catalytic combustion kinetics: Using a direct search algorithm to evaluate kinetic parameters from light-off curves, *Can. J. Chem. Eng.* 81 (2003) 1192-1199.
- [11] A. Pandya, J. Mmbaga, R.E. Hayes, W. Hauptmann, M. Votsmeier, Global kinetic model and parameter optimization for a diesel oxidation catalyst, *Top. Catal.* 52 (2009) 1929-1933.
- [12] N. Rankovic, A. Nicolle, D. Berthout, P. Da Costa, Kinetic modeling study of the oxidation of carbon monoxide-hydrogen mixtures over Pt/Al<sub>2</sub>O<sub>3</sub> and Rh/Al<sub>2</sub>O<sub>3</sub> catalysts, *J. Phys. Chem. C* 115 (2011) 20225-20236.
- [13] S. Sa, J.M. Sousa, A. Mendes, Steam reforming of methanol over a CuO/ZnO/Al<sub>2</sub>O<sub>3</sub> catalyst, part I: Kinetic modelling, *Chem. Eng. Sci.* 66 (2011) 4913-4921.
- [14] P. Stefanov, S. Todorova, A. Naydenov, B. Tzaneva, H. Kolev, G. Atanasova, D. Stoyanova, Y. Karakirova, K. Aleksieva, On the development of active and stable Pd-Co/gamma-Al<sub>2</sub>O<sub>3</sub> catalyst for complete oxidation of methane, *Chem. Eng. J.* 266 (2015) 329-338.
- [15] B.W. Wojciechowski, N.M. Rice, *Experimental methods in kinetic studies*, Elsevier, Boston, 2003.
- [16] F.V. Hanson, M. Boudart, Reaction between H<sub>2</sub> and O<sub>2</sub> over supported platinum catalysts, *J. Catal.* 53 (1978) 56-67.
- [17] M.G. Jones, T.G. Nevell, Oxidation of Hydrogen over Supported Palladium, *J. Catal.* 122 (1990) 219-229.

- [18] T. Engel, G. Ertl, Molecular beam investigation of catalytic oxidation of CO on Pd (111), *J. Chem. Phys.* 69 (1978) 1267-1281.
- [19] Y.F.Y. Yao, The oxidation of CO and hydrocarbons over noble-metal catalysts, *J. Catal.* 87 (1984) 152-162.
- [20] D.E. Mears, Tests for transport limitations in experimental catalytic reactors, *Ind. Eng. Chem. Proc. Des. Dev.* 10 (1971) 541-547.
- [21] S.E. Voltz, C.R. Morgan, Liederma.D, S.M. Jacob, Kinetic study of carbon-monoxide and propylene oxidation on platinum catalysts, *Ind. Eng. Chem. Prod. Res. Dev.* 12 (1973) 294-301.
- [22] L.L. Hegedus, S.H. Oh, K. Baron, Multiple steady states in an isothermal, integral reactor - The catalytic oxidation of carbon monoxide over platinum-alumina, *AIChE J.* 23 (1977) 632-642.
- [23] G. Ertl, P.R. Norton, J. Rustig, Kinetic oscillations in the platinum-catalyzed oxidation of CO, *Phys Rev Lett* 49 (1982) 177-180.
- [24] R. Imbihl, G. Ertl, Oscillatory kinetics in heterogeneous catalysis, *Chem. Rev.* 95 (1995) 697-733.
- [25] B.C. Sales, J.E. Turner, M.B. Maple, Oscillatory oxidation of CO over Pt, Pd and Ir catalysts: Theory, *Surf. Sci.* 114 (1982) 381-394.
- [26] J.E. Turner, B.C. Sales, M.B. Maple, Oscillatory oxidation of CO over a Pt catalyst, *Surf. Sci.* 103 (1981) 54-74.
- [27] A. Boubnov, A. Ganzler, S. Conrad, M. Casapu, J.D. Grunwaldt, Oscillatory CO oxidation over Pt/Al<sub>2</sub>O<sub>3</sub> catalysts studied by in situ XAS and DRIFTS, *Top. Catal.* 56 (2013) 333-338.
- [28] A. Bourane, Oxidation of CO on a Pt/Al<sub>2</sub>O<sub>3</sub> catalyst: from the surface elementary steps to light-off tests V. Experimental and kinetic model for light-off tests in excess of O<sub>2</sub>, *J. Catal.* 222 (2004) 499-510.
- [29] D.J. Kaul, E.E. Wolf, Ftir studies of surface-reaction dynamics. 1. Temperature and concentration programming during CO oxidation on Pt/SiO<sub>2</sub>, *J. Catal.* 89 (1984) 348-361.
- [30] E.M.C. Alayon, J. Singh, M. Nachtegaal, M. Harfouche, J.A. van Bokhoven, On highly active partially oxidized platinum in carbon monoxide oxidation over supported platinum catalysts, *J. Catal.* 263 (2009) 228-238.
- [31] P.A. Carlsson, L. Osterlund, P. Thormahlen, A. Palmqvist, E. Fridell, J. Jansson, M. Skoglundh, A transient in situ FTIR and XANES study of CO oxidation over Pt/Al<sub>2</sub>O<sub>3</sub> catalysts, *J. Catal.* 226 (2004) 422-434.
- [32] A.M. Ganzler, M. Casapu, A. Boubnov, O. Muller, S. Conrad, H. Lichtenberg, R. Frahm, J.D. Grunwaldt, Operando spatially and time-resolved X-ray absorption spectroscopy and infrared thermography during oscillatory CO oxidation, *J. Catal.* 328 (2015) 216-224.
- [33] J. Singh, E.M.C. Alayon, M. Tromp, O.V. Safonova, P. Glatzel, M. Nachtegaal, R. Frahm, J.A. van Bokhoven, Generating highly active partially oxidized platinum during oxidation of carbon monoxide over Pt/Al<sub>2</sub>O<sub>3</sub>: in situ, time-resolved, and high-energy-resolution X-ray absorption spectroscopy, *Angew. Chem. Int. Ed.* 47 (2008) 9260-9264.
- [34] R. Jensen, T. Andersen, A. Nierhoff, T. Pedersen, O. Hansen, S. Dahl, I. Chorkendorff, Self-sustained carbon monoxide oxidation oscillations on size-selected platinum

- nanoparticles at atmospheric pressure, *Phys. Chem. Chem. Phys.* 15 (2013) 2698-2702.
- [35] T.H. Lindstrom, T.T. Tsotsis, Reaction rate oscillations during CO oxidation over Pt/ $\gamma$ - $\text{Al}_2\text{O}_3$  - experimental observations and mechanistic causes, *Surf. Sci.* 150 (1985) 487-502.
- [36] S.B. Vendelbo, C.F. Elkjaer, H. Falsig, I. Puspitasari, P. Dona, L. Mele, B. Morana, B.J. Nelissen, R. van Rijn, J.F. Creemer, P.J. Kooyman, S. Helveg, Visualization of oscillatory behaviour of Pt nanoparticles catalysing CO oxidation, *Nat Mater* 13 (2014) 884-890.
- [37] R.C. Runnebaum, T. Nimmanwudipong, R.R. Limbo, D.E. Block, B.C. Gates, Conversion of 4-methylanisole catalyzed by Pt/ $\gamma$ - $\text{Al}_2\text{O}_3$  and by Pt/ $\text{SiO}_2$ - $\text{Al}_2\text{O}_3$ : Reaction networks and evidence of oxygen removal, *Catal. Lett.* 142 (2012) 7-15.
- [38] F. Morfin, T. Nguyen, J. Rousset, L. Piccolo, Synergy between hydrogen and ceria in Pt-catalyzed CO oxidation: An investigation on Pt-CeO<sub>2</sub> catalysts synthesized by solution combustion, *Applied Catalysis B: Environmental* Just Accepted (2016) DOI: 10.1016/j.apcatb.2016.1001.1056.
- [39] H.S. Fogler, *Elements of chemical reaction engineering*, 4th ed., Prentice Hall PTR, Upper Saddle River, NJ, 2006.
- [40] B.L.M. Hendriksen, S.C. Bobaru, J.W.M. Frenken, Bistability and oscillations in CO oxidation studied with scanning tunnelling microscopy inside a reactor, *Catal. Today* 105 (2005) 234-243.
- [41] P.B. Weisz, C.D. Prater, Interpretation of measurements in experimental catalysis, *Adv. Catal.* 6 (1954) 143-196.
- [42] R.K. Herz, S.P. Marin, Surface chemistry models of carbon monoxide oxidation on supported platinum catalysts, *J. Catal.* 65 (1980) 281-296.
- [43] E.L. Cussler, *Diffusion: Mass transfer in fluid systems*, Cambridge University Press, New York, NY, 2009.
- [44] J. Kestin, H.E. Khalifa, W.A. Wakeham, Viscosity and Diffusion-Coefficients of Binary-Mixtures of Xenon with Other Noble-Gases, *Physica A* 90 (1978) 215-228.
- [45] J. Kestin, W.A. Wakeham, S.T. Ro, Viscosity of noble gases in temperature range 25-700 degrees, *J. Chem. Phys.* 56 (1972) 4119-4124.
- [46] M.M. Papari, D. Mohammad-Aghaiee, B. Haghighi, A. Boushehri, Transport properties of argon-hydrogen gaseous mixture from an effective unlike interaction, *Fluid Phase Equilib.* 232 (2005) 122-135.
- [47] W.E. Ranz, W.R. Marshall, Evaporation from drops part 2, *Chem. Eng. Prog.* 48 (1952) 173-180.
- [48] B.A. Younglove, H.J.M. Hanley, The viscosity and thermal conductivity coefficients of gaseous and liquid argon, *J. Phys. Chem. Ref. Data* 15 (1986) 1323-1337.
- [49] M.W. Chase, Jr., *NIST-JANAF Thermochemical tables*, fourth ed., American Institute of Physics, Woodbury, NY, 1998.



## Chapter 6: Conclusions and Future Direction

### 6.1. Conclusions

High throughput screening of catalytic materials for both quantitative and qualitative kinetic assessment is both highly desirable and required in order to match the rate at which catalysts are synthesized across composition and property space. This thesis has demonstrated a novel, rapid, and accurate method of variable-temperature reaction profile analysis that allows for the modeling of activity and the extraction of kinetic parameters from experimental data. The method is easily accessible, and it is applicable to many reactions of importance today, such as three-way catalysis.

Surface reactions over heterogeneous catalysts typically obey complex reaction mechanisms. The full mechanisms contain large numbers of kinetic parameters, making parameter discrimination difficult. These mechanisms can often be reduced to simple power rate laws over a large range of relevant reaction conditions. Combination and integration of the design equation for a packed bed reactor (PBR) and the Arrhenius equation for the rate constant, with an appropriate power rate law allow us to model the entire kinetically-limited reaction profile. For rate laws with a single concentration dependence, and for select cases when the rate law has two concentration dependences, unique analytical solutions exist. Simulation of variable-temperature reaction profiles show that the shape and position of a profile is unique for each rate law and set of kinetic parameters ( $A$ ,  $E_a$ , and the reaction orders). Qualitative changes in reaction profiles are correlated with known changes in these parameters, and can be used to rapidly discriminate between rate laws. When all kinetic

parameters are known, simulated reaction profiles can be used to predict reactor performance faster than experiments.

The analytical solutions for conversion as a function of temperature were curve-fitted to individual experimental reaction profiles to extract accurate information about the activation parameters and the reaction orders. The oxidation of hydrogen, propane, and carbon monoxide were chosen as representative reactions. An individual curve-fit yields the same activation energy as a conventional Arrhenius plot made using kinetic data collected under differential conditions. Estimation of the reaction orders is less accurate, especially for reaction orders with respect to an excess reactant. Global curve-fitting of analytical variable-temperature kinetic equations to sets of ten reaction profiles recorded with varying residence times yielded activation parameters and reaction orders, in agreement with previous studies. In the future the method could be used to rapidly assess changes in catalytic performance due to changes in the active metal, loading, particle size, and presence of promoters.

Variable-temperature kinetic analysis was coupled with *operando* infrared spectroscopy (IR) and X-ray absorption spectroscopy (XAS) to probe the dynamic chemistry of the active site(s) during stoichiometric CO oxidation over Pd/Al<sub>2</sub>O<sub>3</sub>. The activation energy obtained from variable-temperature kinetic analysis,  $(92.1 \pm 2.2) \text{ kJ mol}^{-1}$ , is consistent with that of Pd(0) nanoparticles. *In situ* XAS showed that the bulk of PdO is reduced to Pd(0) upon exposure to the reactive atmosphere, below the onset temperature for catalytic activity. The observation of only linearly-bound CO to Pd(0) confirms the change in the state of the catalyst from oxide to metal, which is undetectable through kinetic measurements at low temperature. During recording of the extinction profile, a single *operando* IR spectra showed a decrease in CO bound atop on Pd(0) consistent with Pd

oxidation, with an increase in conversion. Oscillations in the activity have been observed by kinetic measurements but rarely correlated with changes in the active sites through *in situ* or *operando* spectroscopy. This study suggests the formation of a more active oxide phase, as evidenced by IR. This highlights the need for coupled kinetic and *in situ* experiments to fully understand the catalyst.

Variable-temperature kinetic analysis was expanded to include external and internal mass transport effects, by incorporating the rate of external mass transport and the internal effectiveness factor. Reaction profiles were simulated numerically, and the resulting profiles showed continuous transitions from predicted kinetically-limited behavior to mass transport-limited regimes. Experimental reaction profiles for CO oxidation catalyzed by Pt/Al<sub>2</sub>O<sub>3</sub> were recorded for varying catalyst support particle sizes to observe the effects of diffusion on the reaction profile. Curve-fitting to the profiles prior to light-off returned activation energies consistent with that of Pt(0). In each reaction profile, abrupt light-off caused rapid acceleration to maximum conversion. Larger particles light-off earlier, while smaller particles light-off at higher temperatures and conversions. We propose that the increase in particle size promotes the oxidation of Pt deep inside the pores where the CO concentration is low. Therefore larger catalysts with a higher barrier to internal diffusion light-off before smaller particles.

## **6.2. Future directions**

The variable-temperature kinetic analysis developed in this thesis greatly reduces the time required to assess the kinetics and rate law of a reaction, opening the door to many potential fruitful applications. For instance, this method can be applied to catalysts which

deactivate rapidly, as long as the time scale is longer than the time it takes to record a reaction profile, ca. 30 minutes. In conventional kinetic analysis, catalyst deactivation would complicate kinetic data. This is of particular importance for single site catalysts, metal clusters, and other supported materials that are prone to deactivation by pathways such as sintering.

To further increase the speed at which kinetic information is gathered, multiple reactions can be tested simultaneously. These results may differ from with those obtained from experiments in which a single reaction is studied because the reactant atmosphere may promote changes in the active state of the catalyst due to poisoning or redox. Variable-temperature kinetic analysis is an appropriate method to extract kinetic parameters for three-way catalysts and to simulate automobile exhaust emission profiles.

Limitations in the maximum volumetric flow rate and catalyst particle size in our experimental design make studying severe external and internal mass transport limitations difficult. For CO oxidation catalyzed by Pt/Al<sub>2</sub>O<sub>3</sub>, we were unable to detect external mass transfer limitations before light-off, although they were evident after light-off, and at high conversion, the profiles were mass transfer-limited. It would be interesting to design a reactor configuration that allows for mass transfer-limitations at all conversions, but the reactor does not experience significant temperature gradients.

Dynamic changes in platinum group metals used to catalyze CO oxidation have been studied for decades, yet there is still no clear consensus about the causes of catalyst light-off or the oscillations sometimes observed. Variable-temperature kinetic analysis should be coupled with *operando* XAS on a rapid scanning synchrotron beamline to capture the local structure and oxidation state of the catalyst during light-off and extinction. Direct

observation of the conversion with high temperature resolution will make it possible to capture the structure of the high and low activity states of the catalyst during extinction, similar to our observation during *operando* IR. Reaction profiles for CO oxidation catalyzed by Pt/Al<sub>2</sub>O<sub>3</sub> (1000 ppm CO, 4000 ppm O<sub>2</sub>) with a flow rate of 100 mL min<sup>-1</sup> showed interesting behavior that would be ideal for *operando* investigations. After the initial light-off, the conversion plateaued briefly before a secondary light-off event, and the conversion increased slowly to maximum conversion over 20 °C. Using an online-mass spectrometer coupled with XAS, the local structure of Pt before, during, and after both light-off events could be examined. These reaction conditions appear to stabilize the active form of the catalyst over larger temperature ranges than previously explored conditions.